TWO-SCALE METHOD FOR WALL-BOUNDED FLOWS



Chen Chen

Somerville College

Department of Engineering Science

University of Oxford

This thesis is submitted for the degree of Doctor of Philosophy

February 2023

DECLARATION

This dissertation is the result of my own work and includes nothing, which is the outcome of work done in collaboration except where specifically indicated in the text. It has not been previously submitted, in part or whole, to any university of the institution for any degree, diploma, or other qualification.

In accordance with the Department of Engineering Science guidelines, this thesis does not exceed 250 pages, and it contains less than 150 figures.

Signed:_____

Date:_____

Chen Chen

Oxford, Oxfordshire

ABSTRACT

Recent findings on wall-bounded turbulence prompt a new impetus for modelling development to capture and resolve the Reynolds-number-dependent influence of outer flow on near-wall turbulence in terms of the 'foot-printing' of the large-scale coherent structures and the scale-interaction associated 'modulation'. A two-scale method is developed to couple a locally embedded near-wall fine-mesh DNS block with a global coarser mesh domain. The influence of the large-scale structures on the local fine-mesh block is captured by a scale-dependent coarse-fine domain interface treatment. The global near-wall coarse-mesh region outside the local fine-mesh block is governed by the augmented flow governing equations with forcing source terms generated by upscaling the space-time averaged fine-mesh solution. The validity and effectiveness of the method are examined for canonical incompressible channel flows at several Reynolds numbers. It is shown that the mesh-count scaling with Reynolds number is potentially reduced from $O(Re^2)$ for the conventional fully wall-resolved LES to $O(Re)$ for the present locally embedded two-scale LES. The method is also extended to the implementation in boundary layer flows. A 2-dimensional roughness element is used to trip a turbulent boundary layer. It is observed that large-scale disturbances originating from the trip have a much shorter lifetime and weaker foot-printing signatures on near-wall flow compared to those long streaky coherent structures in well-developed wall-bounded turbulent flows. For the tripped turbulent boundary layer, a Chebyshev block spectral mapping is adopted to propagate source terms, driving the upscaled equations to a target solution. The overall mesh count - Re scaling is estimated to reduce from $O(Re^{1.8})$ for the full wall-resolved LES to $O(Re^{0.9})$ for the present two-scale solution.

ACKNOWLEDGEMENTS

I am grateful to my supervisor, Professor Li He, for his patience and continuous efforts in leading me to become a better ‘thinker’ on not only this DPhil project but also on all interesting things around along the journey.

Special thanks should go to everyone I met in the Osney Lab, especially during the difficult pandemic time. Much appreciation should be expressed to Mr Craig Parsons for the IT support and the warm smiles.

I am grateful to my dear parents for their continuous support from the other side of the planet. Also, I would like to take this opportunity to express my thanks to Yin, for these years’ companion.

Much gratitude also goes to the China Scholarship Council for providing financial support for my study.

Finally, thanks also go to me myself for these years of endeavour and hard work to learn from the fluid mechanics: Life is multi-scaled. Focus on the essence. World is diversified. Embrace the interaction.

CONTENTS

1 INTRODUCTION 22

1.1 GENERAL BACKGROUNDS 22

1.2 OBJECTIVES AND SCOPE OF THESIS 24

1.3 THESIS OUTLINE 26

2 LITERATURE REVIEW 28

2.1 BASICS OF TURBULENT FLOWS 28

2.1.1 Wall-bounded Turbulence 28

2.1.2 Turbulence Length Scales 32

2.1.3 Near-wall Universal Behaviour 33

2.1.4 Boundary Layer Transition 35

2.2 NUMERICAL SIMULATIONS AND TURBULENCE MODELLING 37

2.2.1 Computational Cost of Numerical Simulations 37

2.2.2 Resolving and Modelling Turbulence 39

2.2.3 Near-wall Modelling 41

2.2.4 Numerical Inflow Conditioning for Turbulent Boundary Layer 44

2.3 RECENT PROGRESS IN UNDERSTANDING WALL TURBULENCE 46

2.3.1 Outer Plateau in Energy Spectrum 47

2.3.2 Foot-printing and Modulation 49

2.3.3 Minimum Flow Unit Approach *51*

2.4 SUMMARY 52

3 METHODOLOGY 55

3.1 OVERALL FRAMEWORK 56

3.2 DUAL MESHING AND INTERFACE TREATMENT 58

3.3 TWO-SCALE FORMULATION 60

3.3.1 Upscaling for Time-averaging/Reynolds-averaging *61*

3.3.2 Upscaling for the Present Space-time Averaging *63*

3.4 TWO-SCALE BLOCK-SPECTRAL METHOD FOR TURBULENT BOUNDARY LAYER 68

4 INITIAL IMPLEMENTATIONS AND ASSESSMENTS FOR RANS 74

4.1 CHANNEL FLOW 75

4.1.1 Temporal Non-linearity *75*

4.1.2 Spatial Non-linearity *82*

4.1.3 RANS Solution *85*

4.2 TURBULENT BOUNDARY LAYER 90

4.3 SUMMARY 96

5 TWO-SCALE SOLUTIONS FOR TURBULENT CHANNEL FLOWS 98

5.1 MESH-COUNT SCALING WITH REYNOLDS NUMBER 99

5.1.1 Sizing of Fine-mesh Block *99*

5.1.2 Scaling mesh count with Reynolds number *102*

5.2 IMPLEMENTATION FOR CHANNEL FLOW CASE STUDY 108

5.2.1 Baseline flow solution method 108

5.2.2 Parameters for DNS and LES case studies 108

5.3 WALL-EMBEDDED DNS 112

5.3.1 Mean Statistics 113

5.3.2 Spectral Analysis 117

5.3.3 'Foot-printing' and 'Modulation' in Near-wall Region 127

5.4 WALL-EMBEDDED LES 132

5.5 SUMMARY 137

6 TRIPPING OF TURBULENT BOUNDARY LAYERS 142

6.1 BASELINE METHOD AND CASE SET-UPS 143

6.2 LES VALIDATION AND RESOLUTION REQUIREMENT FOR TRIPPING 148

6.3 EVOLUTION TOWARDS EQUILIBRIUM STATE 155

6.4 EVOLUTION AND IMPACT OF LARGE-SCALE DISTURBANCES 163

6.5 SUMMARY 172

7 TWO-SCALE SOLUTIONS FOR TURBULENT BOUNDARY LAYERS 174

7.1 SIZING LOCALLY EMBEDDED FINE-MESH BLOCK FOR TRIPPING 175

7.2 TWO-SCALE SOLUTION FOR TRIPPED TBL 180

7.2.1 Validation against Baseline Full LES 180

7.2.2 Cases with Higher Reynolds Numbers 187

7.3 MESH COUNT – REYNOLDS NUMBER SCALING 190

7.4 SUMMARY 195

8 CONCLUSIONS AND RECOMMENDATIONS FOR FUTURE WORK..... 197

9 REFERENCES..... 202

10 APPENDICES..... 220

LIST OF TABLES

TABLE 4.1 RANS SIMULATION PARAMETERS WITHIN GLOBAL (G) AND LOCAL-EMBEDDED (L) DOMAINS. 87

TABLE 5.1 WEDNS SIMULATION PARAMETERS WITHIN GLOBAL (G) AND LOCAL-EMBEDDED (L) DOMAINS 111

TABLE 5.2 WELES PARAMETERS FOR GLOBAL (G) AND LOCAL-EMBEDDED (L) DOMAINS 112

TABLE 5.3 WALL SHEAR-STRESS PREDICTION OF THE TWO-SCALE WEDNS APPROACH 114

TABLE 5.4 WALL-SHEAR-STRESS PREDICTION OF THE TWO-SCALE WELES APPROACH 135

TABLE 6.1 DETAILS OF MESH RESOLUTION OF THE CASES SIMULATED 147

TABLE 6.2 AVERAGED PRESSURE GRADIENT AT APPROXIMATELY $y{\sim}Ly/8$ 148

TABLE 7.1 FRONTAL BLOCK WIDTHS OF THE CASES SIMULATED.....176

TABLE 7.2 SIMULATION PARAMETERS OF CALCULATIONS WITH HIGHER Re 188

LIST OF FIGURES

FIGURE 2.1. SKETCHES OF (A) CHANNEL FLOW AND (B) FLAT-PLATE BOUNDARY LAYER FLOW. 30

FIGURE 2.2. VELOCITY PROFILES FROM PUBLISHED DNS SOLUTIONS. 31

FIGURE 2.3. TURBULENCE ENERGY SPECTRUM. 33

FIGURE 2.4. ONE-DIMENSIONAL PRE-MULTIPLIED ENERGY SPECTRA 48

FIGURE 2.5. THE FOOT-PRINTING EFFECT ILLUSTRATED IN MARUSIC ET AL. (2017) ... 51

FIGURE 3.1. DOMAIN CONFIGURATIONS FOR THE CHANNEL FLOW WITH A LOCALLY EMBEDDED BLOCK. 56

FIGURE 3.2. DOMAIN-DOMAIN INFLUENCE AND INTERACTION IN A TWO-SCALE FRAMEWORK. 58

FIGURE 3.3. FLOWCHART OF THE TWO-SCALE SOLUTION PROCESS AS IMPLEMENTED. 67

FIGURE 3.4. ILLUSTRATION OF COMPUTING DOMAINS WITH NEAR-WALL EMBEDDED DNS BLOCKS. 70

FIGURE 3.5. FLOWCHART OF THE TWO-SCALE BLOCK-SPECTRAL SOLUTION PROCESS AS IMPLEMENTED. 73

FIGURE 4.1. THE PRESENT LES SOLUTIONS COMPARED WITH THE DNS DATABASE.... 78

FIGURE 4.2. CONVERGENCE HISTORY AS THE NORMALISED RESIDUAL VERSUS MARCHING TIME STEPS OF CASES USING DIFFERENT DAMPING PARAMETERS..... 81

FIGURE 4.3. MEAN VELOCITY PROFILES AS SOLUTIONS USING DIFFERENT DAMPING PARAMETERS. 82

FIGURE 4.4. VELOCITY PROFILES IN THE LAMINAR CHANNEL FLOW. 84

FIGURE 4.5. FLOWCHART OF THE TWO-SCALE BLOCK-SPECTRAL SOLUTION PROCESS AS IMPLEMENTED IN RANS CHANNEL FLOWS. 88

FIGURE 4.6. MEAN VELOCITY PROFILES OF RANS COMPARED WITH DNS SOLUTIONS 89

FIGURE 4.7. TURBULENT EDDY VISCOSITY νt MODELLED FROM THE S-A MODEL.....90

FIGURE 4.8. BASELINE VALIDATION AGAINST NASA DATA 93

FIGURE 4.9. FLOWCHART OF THE TWO-SCALE BLOCK-SPECTRAL SOLUTION PROCESS AS IMPLEMENTED IN RANS BOUNDARY LAYER FLOWS. 94

FIGURE 4.10. VELOCITY PROFILES COMPARED WITH THE '*BASELINE-FINE*' 95

FIGURE 4.11. VELOCITY PROFILES COMPARED WITH THE '*BASELINE-FINE*' 96

FIGURE 5.1. ONE-DIMENSIONAL PRE-MULTIPLIED ENERGY SPECTRA 101

FIGURE 5.2. COMPARISON OF MESH COUNT SCALING WITH REYNOLDS NUMBER: 107

FIGURE 5.3. MEAN VELOCITY PROFILES IN (A, C, E) AND TURBULENCE FLUCTUATIONS IN (B, D, F).....116

FIGURE 5.4. SOURCE TERM PROFILES IN RELATION TO WALL DISTANCE $y+$ AT TWO REYNOLDS NUMBERS.....117

FIGURE 5.5. (A) THE $x-z$ PLANE SNAPSHOT OF THE INSTANTANEOUS VELOCITY FIELD AROUND THE EMBEDDED BLOCK AT THE INNER LOCATION $y+=13.5$. (B) ISO-CONTOURS OF THE SECOND INVARIANT OF THE VELOCITY GRADIENT TENSOR (JEONG & HUSSAIN, 1995), COLOURED WITH THE INSTANTANEOUS VELOCITY. THE SOLID BLACK BOXES MARK THE EMBEDDED FINE-MESH BLOCK.....119

FIGURE 5.6. THE x-y SNAPSHOT OF THE SPANWISE VORTICITY ωz FIELD NEAR WALL: 120

FIGURE 5.7. ONE-DIMENSIONAL ENERGY SPECTRA AT $y+= 13.5$ AT $Re\tau \approx 1000$ .. 121

FIGURE 5.8. TURBULENCE POWER SPECTRA DENSITY (PSD) AS FUNCTIONS OF THE NON-DIMENSIONAL FREQUENCY AT $Re\tau \approx 1000$ 122

FIGURE 5.9. ONE-DIMENSIONAL PRE-MULTIPLIED ENEGY SPECTRA $kz\Phi uu +$..... 124

FIGURE 5.10. TWO-DIMENSIONAL PRE-MULTIPLIED ENERGY SPECTRUM $kxkz\Phi uu$.. 125

FIGURE 5.11. ONE-DIMENSIONAL PRE-MULTIPLIED ENERGY SPECTRA $kz\Phi uu$ AT $Re\tau \approx 2000$..... 126

FIGURE 5.12. ILLUSTRATION OF THE 'FOOT-PRINTING' EFFECT. 129

FIGURE 5.13. ILLUSTRATION OF THE 'MODULATION'. 131

FIGURE 5.14. THE INSTANTANEOUS VELOCITY FIELDS AT THE VICINITY OF THE EMBEDDED REGION AS THE GREEN BOX IN FIGURE 5.13(B) ENLARGED. 132

FIGURE 5.15. MEAN VELOCITY PROFILES AT HIGH REYNOLDS NUMBERS: (A) $Re\tau \approx 2000$; (B) $Re\tau \approx 4100$; (C) $Re\tau \approx 5200$..... 134

FIGURE 5.16. INNER ENERGY SPECTRA..... 136

FIGURE 5.17. COMPARISON IN MESH COUNT SCALING WITH REYNOLDS NUMBER:.... 137

FIGURE 6.1. SCHEMATIC OF THE COMPUTATIONAL DOMAIN..... 145

FIGURE 6.2. FRICTION COEFFICIENTS Cf AS FUNCTIONS OF $Re\theta$ ALONG THE STREAMWISE DIRECTION 150

FIGURE 6.3. INDICATORS $\delta/\delta*$ AND δ/θ COMPARED WITH THE CORRELATED CURVES 151

FIGURE 6.4. THE SHAPE FACTOR $H12$ AS FUNCTIONS OF $Re\theta$ 152

FIGURE 6.5. THE DEVELOPMENT OF BOUNDARY LAYER THICKNESS $\delta+$ AS FUNCTIONS OF $Re\theta$.....153

FIGURE 6.6. MEAN STATISTICS WITH RESPECT TO WALL-NORMAL DISTANCES $y+$....154

FIGURE 6.7. ISO-SURFACES OF THE Q-CRITERION IN THE INNER REGION WITH REFINED MESH. 156

FIGURE 6.8. INDICATORS $\delta/\delta*$ AND δ/θ COMPARED WITH THE EXPERIMENTALLY CORRELATED CURVES BY CHAUHAN ET AL. (2009) 158

FIGURE 6.9. THE DISSIPATION COEFFICIENT Cd AS FUNCTIONS OF Rex, CATEGORISED AS FOUR STAGES: LAMINAR, TRANSITIONAL, NON-EQUILIBRIUM AND EQUILIBRIUM. 159

FIGURE 6.10. ONE-DIMENSIONAL PRE-MULTIPLIED ENERGY SPECTRA 160

FIGURE 6.11. THE POWER SPECTRAL DENSITY (PSD) IN RELATION TO THE NON-DIMENSIONAL FREQUENCIES.....162

FIGURE 6.12. THE ORIGINAL AND FILTERED FIELD AROUND THE TRIPPING REGION....164

FIGURE 6.13. THE ORIGINAL AND FILTERED FIELD FROM $Re\theta \approx 800$ TO 950.....165

FIGURE 6.14. PROPER 'FOOT-PRINTING' EVIDENCE AT HIGH Re IN THE FULLY DEVELOPED CHANNEL FLOW.....166

FIGURE 6.15. THE LOSS FUNCTION IN RELATION TO THE NUMBER OF MODES INVOLVED FOR FIELD RECONSTRUCTION N. 168

FIGURE 6.16. THE RECONSTRUCTED FIELD COMPARED WITH THE ORIGINAL. 169

FIGURE 6.17. THE DOMINANT MODES EXTRACTED FROM THE MID $x - y$ PLANE FROM FULL WRLES WITH FREQUENCY AROUND (A) $St \approx 0.3$ (B) $St \approx 0.6$ AND (C) $St \approx 0.9$. 171

FIGURE 7.1. TURBULENCE POWER SPECTRA DENSITY (PSD) WITH RESPECT TO THE NON-DIMENSIONAL FREQUENCY, STROUHAL NUMBER St..... 177

FIGURE 7.2. MEAN VELOCITY PROFILES AS FUNCTIONS OF WALL-NORMAL DISTANCE $y+$ AT (A) $Re\theta \approx 600$ AND (B) $Re\theta \approx 800$. PROFILES OF STREAMWISE VELOCITY FLUCTUATIONS AS FUNCTIONS OF $y+$ AT (C) $Re\theta \approx 600$ AND (D) $Re\theta \approx 800$. 178

FIGURE 7.3. PSD AS FUNCTIONS OF NON-DIMENSIONAL FREQUENCIES BASED ON BOUNDARY LAYER THICKNESS δ AND WALL SHEAR VELOCITY $u\tau$ AT (A) $Re\theta \approx 600$ AND (B) $Re\theta \approx 800$..... 179

FIGURE 7.4. COMPARISON OF LARGE-SCALE DISTURBANCES ($St \approx 0.3$) ON THE MID $x - y$ PLANE FROM (A) FULL LES AND (B) THE LOCAL DNS BLOCK. 180

FIGURE 7.5. THE FRICTION COEFFICIENT Cf AS THE FUNCTION OF REYNOLDS NUMBER Rex..... 181

FIGURE 7.6. THE MEAN VELOCITY PROFILE IN RELATION TO WALL NORMAL DISTANCE $y+$ IN THE GLOBAL COARSE-MESH REGION. 182

FIGURE 7.7. DISTRIBUTION OF SOURCE TERM VECTORS $ST = (STx, STy, STz)$ ALONG THE STREAMWISE DIRECTION AS FUNCTIONS OF REYNOLDS NUMBERS Rex IN THE VISCOUS SUBLAYER ($y+ \approx 6$). 183

FIGURE 7.8. MEAN STATISTICS. 185

FIGURE 7.9. PSD WITH RESPECT TO THE DIMENSIONLESS FREQUENCIES. 187

FIGURE 7.10. THE FRICTION COEFFICIENT Cf AS THE FUNCTION OF REYNOLDS NUMBER $Re\theta$. 189

FIGURE 7.11. MEAN STATISTICS. 190

FIGURE 7.12. SECTIONED TBL DOMAIN: (A) ILLUSTRATION OF THE TBL DOMAIN WITH Ns SUB-DOMAINS. (B) A CLOSE-UP VIEW OF THE SUB-DOMAIN i. 192

FIGURE 7.13. MESH COUNT - Re SCALING. 195

FIGURE 10.1. DOMAIN WITH COARSE-MESH BUFFER REGIONS AS AN EXTENDED VERSION OF FIGURE 3.1. 222

FIGURE 10.2. MEAN VELOCITY PROFILES AT $Re\tau \approx 5200$. 224

LIST OF ABBREVIATIONS AND ACRONYMS

Abbreviations

CFD	Computational Fluid Dynamics
HPC	High Performance Computer
2(3)-D	Two (Three)-dimensional
N-S	Navier-Stokes
DNS	Direct numerical simulation
LES	Large eddy simulation
WMLES	Wall-modelled LES
WRLES	Wall-resolved LES
WeLES	Wall-embedded LES
WeDNS	Wall-embedded DNS
RANS	Reynolds-averaged Navier-Stokes
S-A	Spalart-Allmaras
DES	Detached eddy simulation
TBL	Turbulent boundary layer
TS	Tollmien-Schlichting
BS	Block-spectral
MFU	Minimum flow unit

AMI	Arbitrary mesh interface
PISO	Pressure-Implicit with Splitting of Operators
SIMPLE	Semi-Implicit Method for Pressure Linked Equations
PSD	Power spectra density
EMD	Empirical Mode Decomposition
DMD	Dynamic Mode Decomposition
IMF	Intrinsic Mode Function

Arithmetic Symbols

$\overline{(\cdot)}, <\cdot>$	Time (ensemble) averaged variable
$\widetilde{(\cdot)}$	Spatial averaged variable
$(\cdot)'$	Fluctuation on time-mean variables
$(\cdot)''$	Fine-scale fluctuation on interfaces
$R(\cdot)$	Lumped governing equation
$[\cdot]^{-1}$	Pseudo inverse operator
$\overline{\overline{[\cdot]}}$	DMD reconstructed field

Symbols

$\boldsymbol{A}$	A linear operator
b	DMD mode amplitude
C_i	Multiplier coefficient

C_d Dissipation coefficient

C_f Friction coefficients

$\boldsymbol{C}$ Chebyshev polynomial coefficient set

D Damping term

F Surface patch

$\boldsymbol{f}$ Source-term vector in N-S equations/Chebyshev sampled function vector

f Frequency

f^{approx} Chebyshev interpolated function

G Global domain

H_{12} Shape factor

h Channel height/Mesh spatial increment

k Wavenumber

k_d Dissipation range wavelength lower bound

k_i Inertial subrange wavelength lower bound

L Local embedded domain/Characteristic length

L_d Empirical cut-off mixing length

l Length

m Number of data points in each snapshot

N Number of mesh points/Chebyshev sample points/modes

N_s Number of embedded blocks used

$\boldsymbol{n}$	Vector normal to the face
P	Time-averaged pressure
Pr	Energy production rate
p	Pressure
Re	Reynolds number
r	DMD mode rank number
$\boldsymbol{ST}$	Source term vector
St	Strouhal number
T_n	Chebyshev polynomial
t	Time
U	Time-averaged velocity
U_b	Bulk time-averaged velocity
U_∞	Free-stream velocity
$\boldsymbol{u}$	Flow variable vector
u, v, w	Streamwise, wall-normal, spanwise velocity
u_τ	Shear velocity
$\boldsymbol{X}_1^n$	Instantaneous flow field matrix of snapshot vectors from index 1 to n
$\boldsymbol{x}$	Location vector
x, y, z	Streamwise, wall-normal, spanwise dimension/distance
y_s	Fine-coarse interface location as wall distance

Greek Letters

β	Pressure gradient coefficient
Δ	Small distance
Δt	Time interval
Δv	Small volume
δ	Half channel height/Boundary layer thickness
δ^*	Displacement thickness
ϵ	Energy dissipation rate
η	Kolmogorov scale
θ	Momentum thickness
κ	Von Karmon constant
$\boldsymbol{\Lambda}$	Chebyshev construction matrix
λ	Wavelength
λ_j	Eigenvalues in DMD approach
ν	Kinematic viscosity
ν_d	Artificial viscosity
ρ	Density
τ	Pseudo marching time-step
τ_w	Wall shear stress

$\boldsymbol{\Phi}_j$	Eigenvectors in DMD approach
Φ_{uu}	Energy spectrum of streamwise fluctuations
Ω	Fluid domain
$\boldsymbol{\omega}$	Vorticity

Superscripts

$+$	Variable in wall unit

Subscripts

C	Coarse-mesh solution/configuration
f	Fine-mesh solution/configuration
rms	Root-mean-square value
s	Spatial variable
st	Spatial-temporal variable
t	Temporal variable
$trip$	Trip-associated variable
w	Wall variable

LIST OF APPENDICES

APPENDIX 1 BUFFER REGION AND 'MODULATION' 221

1 INTRODUCTION

1.1 General Backgrounds

Thanks to the rapid development of scientific computing technologies, the power of Computational Fluid Dynamics (CFD) has been recognised for numerically solving complex fluid mechanics problems, ranging from meteorological research to aerospace engineering designs, etc. However, numerical simulations of wall-bounded turbulent flows have long been challenging due to the wide range of length scales involved, from very large eddies away from the wall down to the Kolmogorov scales in the near-wall region (Kolmogorov 1941), where the required resolution is deemed to be the highest attributed to the spatial and temporal micro-scales. The disparity in length scales gives rise to overly expensive simulations given the limited computational resources in many practical cases at present (Slotnick 2014), longing for more efficient methodologies.

The near wall is the focal region regarding computational costs for wall-bounded turbulent flows (Moin & Jimenez 1997; Jimenez & Moser 2000). The higher the Reynolds number is, the more disparate the scale difference becomes. As a result, the mesh count needed to resolve all scales of turbulence as in the direct numerical simulations (DNS) scale with the Reynolds number as $O(Re^3)$ (Jimenez 2003). For large-eddy simulations (LES) which filter out the small scales to be modelled, the required mesh count still scales up and increases with the Reynolds number as $O(Re^2)$ (Mizuno & Jiménez 2013), thus still being too expensive for many practical engineering applications.

One prevalent framework to reduce the overall computational cost for simulations takes advantage of the near-wall 'universal' behaviour where turbulence behaves in a self-sustained 'autonomous' manner. The underlying wisdom promotes a hybrid approach to couple the near-wall modelled Reynold-averaged Navier Stokes (RANS) part with the scale-resolving outer flow (Spalart et al. 1997; Spalart 2009; Cabot & Moin 2000; Piomelli & Balaras 2002; Larsson, et al. 2016; Bose & Park 2018).

However, the significant findings recently progressed in understanding wall-bounded turbulent flows challenge the existing modelling approaches. The near-wall portion is revealed not to be completely 'universal' but instead consists of a clear Reynolds-number-dependent part that is 'foot-printed' and 'modulated' by large-scale coherent structures away from the wall (Hutchins & Marusic 2007; Jimenez 2013; Lee & Moser 2015).

A distinctive alternative path, which the thesis follows, is aimed at resolving, rather than modelling, the near-wall region, with the use of a small number

of local fine-mesh blocks. The primary consideration is that such an approach with locally resolved fine-mesh solutions must be compatible with the requirement of capturing and resolving the key features as identified in the recent research on near-wall turbulence. In particular, the method needs to capture the large-scale 'foot-prints' and resolve the local scale interactions in the near-wall region adequately.

1.2 Objectives and Scope of Thesis

The overall objective is to develop, implement and validate an efficient two-scale method for wall-bounded flows. Given the background, the key intended attributes of the present development are, firstly the local fine-mesh domain should directly interact with the outer-flow large structures locally and instantaneously, in order to capture the 'foot-prints' appropriately. This leads to research Question 1: how can the local embedded region receive the influence of the large-scale coherent structures?

Secondly, the local and the global domains are to be coupled in a way to minimise the discretisation errors of the under-resolved global coarse-mesh near-wall region. This leads to research Question 2: how can the under-resolved region be conditioned with minimised discretisation errors?

A two-scale source-term oriented approach could potentially be adopted to meet these two requirements. The original framework is developed for specific multi-scale problems of surface micro-structures and effusion cooling (He, 2018). The local near-wall fine-mesh block is embedded in a coarse-mesh domain and the embedded block is directly interfaced with its surrounding coarse-mesh. The coupling between the two domains is facilitated by a space-time averaging of the

fine-mesh solution over the overlapping coarse-mesh cells. The corresponding residual imbalance can simply be taken as the source terms and mapped to the global coarse-mesh domain. These source terms will effectively balance out the under-resolution associated errors for the time-averaged solution over the coarse mesh. It is realised that the main attributes of the methodology are closely relevant to general wall-bounded turbulent flows. The framework is thus adapted to examine more general and fundamental cases and implemented in an open-source code.

Two canonical cases are focused on in this thesis for purposes of fundamental studies on the two aforementioned research questions. Firstly, the two-scale approach is implemented and validated in turbulent channel flows. Secondly, given the homogeneity in both streamwise and spanwise directions as the basic limitation of the canonical channel flow, it is useful to examine and demonstrate the feasibility of the two-scale method for spatially developing turbulent boundary layer (TBL) flows.

Therefore, another relevant issue is raised as the research Question 3 as the prerequisite to studying TBL: how to properly initiate a turbulent boundary layer with clearly and consistently applied inflow conditions? Furthermore, can the TBL be properly initiated in a locally embedded region?

Finally, a substantive appeal for developing such a local-embedded fine-mesh method is the possibility for much more efficient scale-resolving simulations whilst avoiding taking the wall-modelled avenue. Therefore, the relevant research Question 4 is raised: how much computational saving could be achieved? The potential computational gain thus needs to be measured in terms of the mesh-count

scaling with the Reynolds number, which in the present context manifests regarding the fine-mesh block size in relation to the overall mesh count.

Relevant publications by the author include:

1) Chen, C. & He, L., 2022. On locally embedded two-scale solution for wall-bounded turbulent flows. *Journal of Fluid Mechanics*, Volume 933, p. A47.
2) Chen, C. & He, L., 2022 (under revision). Two-scale solution for tripped turbulent boundary layer. *Journal of Fluid Mechanics.*

1.3 Thesis Outline

The rest of the thesis is organised as follows.

Chapter 2 provides a literature review on the basics of wall-bounded turbulence, the prevalent wisdom of wall-modelling techniques and the recent findings challenging the traditional pathway of near-wall modelling.

Chapter 3 presents the overall two-scale methodology including the baseline framework, the dual meshing system with the interface treatment, the two-scale formulation, and the source-term propagation method.

Chapter 4 presents the preliminary implementations of the two-scale method in some simple cases for manifestation. The source-term approach is elaborated and articulated with the non-linearity induced when exerting spatial and temporal averaging in two specific cases. Thereafter, implementation of the method in the RANS cases is demonstrated in channel flows and turbulent boundary layers.

Chapter 5 validates the local embedding two-scale method in turbulent channel flows with the homogeneity ensured in the two wall-parallel directions,

under the framework of both DNS and LES. The overall mesh-count is estimated scaling with the Reynolds number to project the potential savings using the present method.

Chapter 6 explores an effective physical tripping method in the numerical simulations for the initiation of TBL. The inclusion of this chapter in the thesis is to provide a method to establish a turbulent boundary layer for studying the implementation of the two-scale method in the non-homogeneous turbulent flow. The associated extra computational cost in resolving the tripping is evaluated. Also, the evolution and impact of the residual large-scale disturbances of tripping are investigated.

Chapter 7 implements the two-scale method in boundary layer flows with the inhomogeneous streamwise direction as an extension of the method. The overall mesh count is again estimated scaling with the Reynolds number.

Finally, chapter 8 presents the concluding remarks for the thesis and provides general suggestions on potential future works.

2 LITERATURE REVIEW

2.1 Basics of Turbulent Flows

2.1.1 Wall-bounded Turbulence

For fluid flows, be they laminar or turbulent, if are considered continuous media, the ratio between the convective and diffusive effects can be arranged in a non-dimensional way as the Reynolds number (Reynolds 1883):

$$Re = UL/\nu \tag{2.1}$$

where ν is the kinematic viscosity, U is the characteristic velocity and L is the characteristic length. At low Reynolds numbers, the flow is diffusion dominated and could be laminar. At high Reynolds numbers, the flow is convection dominated and turbulent. On many occasions, fluids are naturally highly turbulent and chaotic, consisting of a wide range of length scales.

In many cases of engineering or meteorological studies, turbulent flows are bounded at least partially, by one or more solid surfaces. The wall-bounded turbulent flows can be categorised as internal flows (e.g., the flow through channels, pipes, and ducts) and external flows (e.g., the flow around flat plates, airfoils, ship hulls, and atmospheric boundary layers). The simplest forms of these flows as the canonical ones, for instance, the fully developed channel flows and the turbulent boundary layer flows are of practical importance and have been extensively studied throughout the development of understandings of turbulent flows.

Figure 2.1(a) sketches the flow through a pair of paralleled flat plates as a channel with the distance between plates being the channel height $h = 2\delta$. We confine our attention to the fully developed region with sufficient distance downstream away from the entry, in which case the channel flow is considered statistically stationary and one-dimensional, with velocity statistics depending only on the distance to the wall y. Figure 2.1(b) illustrated the boundary layer formed when a non-turbulent flow with uniform velocity passes over a smooth flat plate. Here, the boundary layer thickness $\delta(x)$ develops continuously and increases in the streamwise direction x along the flat plate.

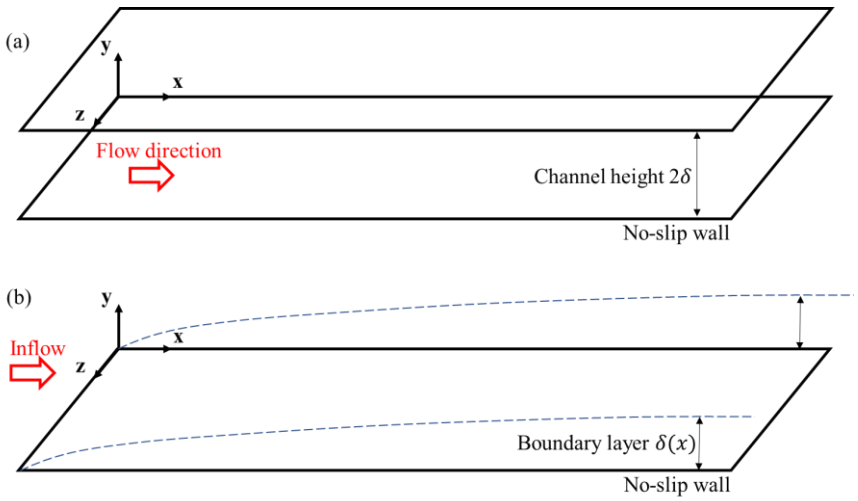


Figure 2.1. **Sketches of (a) channel flow and (b) flat-plate boundary layer flow.**

In both cases, at the solid wall, the time-mean shear stress is completely attributed to the viscous contribution directly correlated with the velocity gradient at the wall as

$$\tau_w = \rho\nu \frac{\partial U}{\partial y}\Big|_{y=0} \tag{2.2}$$

where 'U' denotes the ensemble-averaged time-mean velocity, ρ is the fluid density, and ν is the kinematic viscosity.

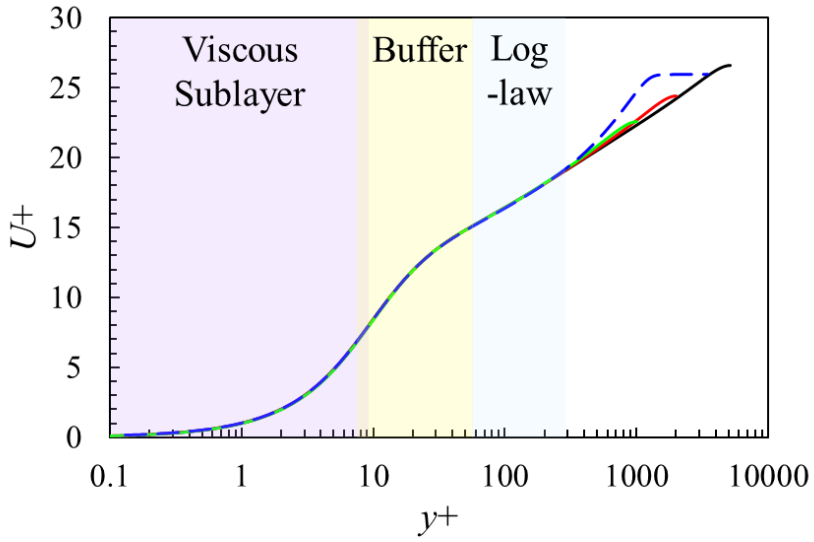


Figure 2.2. **Velocity profiles from published DNS solutions. Channel flow results (Lee & Moser 2015): Green solid line '—': Re_τ ≈1000; Red solid line '—': Re_τ ≈ 2000; Black solid line '—': Re_τ ≈ 5200. Turbulent boundary layer results (Schlatter & Orlu 2012): Blue dashed line '— —': Re_τ ≈ 1300.**

It is widely accepted that the behaviour of the two types of canonical flows in Figure 2.1(a) and (b) is largely identical in the viscous sublayer, buffer region and log-law region, as shown in Figure 2.2. The time-mean velocity profile as the function of wall-distance y with $y < \delta$ can be roughly sectioned as inner and outer regions with the buffer region in between that connects. It is usually regarded that the viscous sublayer covers $0 \leq y^+ \leq 10$. For simplicity, the superscript '+' denotes values in wall units normalised by shear velocity $u_\tau = \sqrt{\tau_w/\rho}$ and viscosity ν. The corresponding Reynolds number is denoted as $Re_\tau = u_\tau \delta/\nu$. The viscous sublayer is dominated by viscous effect. According to Prandtl (1926), this is where the mean velocity profile depends solely on y^+ with the linear relation $U^+ = y^+$ at $y^+ < 5$. Conventionally, the outer log-law region starts beyond $y^+ \approx 50$. The outer log region

convects energy containing large-scale structures. The mean velocity gradient in this region follows $\frac{\partial U^+}{\partial y^+} = \frac{1}{\kappa y^+}$ which integrates to

$$U^+ = \frac{1}{\kappa} ln y^+ + B \tag{2.3}$$

where $\kappa \approx 0.41$ is the von Karmon constant (1930) and $B \approx 5.2$.

2.1.2 Turbulence Length Scales

Kolmogorov (1941) discovered the hierarchy of whirls incorporated in turbulent flows. Turbulent energy is discovered to transform from the largest scale to the smallest one eventually dissipated by molecular viscosity and die out. The turbulence energy spectrum is shown in Figure 2.3. The energy is transferred through turbulent mixing to smaller scales and higher wavenumbers till k_d, where the vortex is small enough to be dissipated into heat. The corresponding micro-scale η related to the wave number k_d is the Kolmogorov scale

$$\eta = \left(\nu^3/\epsilon\right)^{1/4} \tag{2.4}$$

where ν is the kinematic viscosity and ϵ is the energy dissipation rate. As illustrated in Figure 2.3, there are three regions with distinctively different physical behaviours. Firstly, the region where the wave numbers exceed k_d and the wavelengths are smaller than η is the dissipation range. A rapid drop-off at the end of the curve can be observed, which corresponds to the turbulent structures at dissipative scales concentrating at the wall. Secondly, the range over which viscous effects are not so

significant lies between k_i and k_d is the inertial sub-range, containing turbulence structures of integral scales that largely reside in the log region. These scales are dominated by inertial forces transferring energy from the large scales to the small ones. Finally, to the left end of Figure 2.3, the integral scales with the smallest wavenumbers (longest wavelengths) are the largest scales of permanent eddies owning capacity for the majority of the kinetic energy, of which the viscous dissipation is trivial. These are the very large-scale coherent structures in the outer flow far away from the wall.

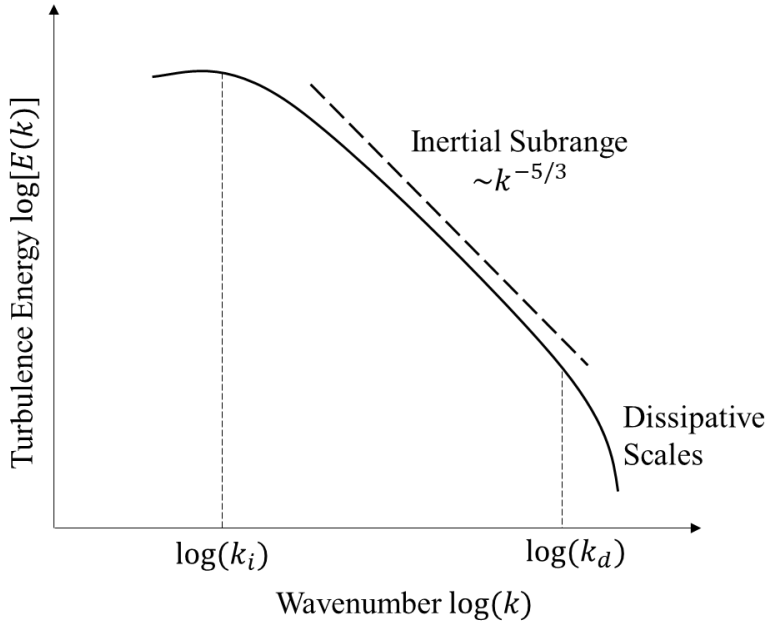


Figure 2.3. **Turbulence energy spectrum.**

2.1.3 Near-wall Universal Behaviour

The near-wall inner layer is essential to the dynamics of wall-attached turbulent shear flows. This is where the turbulent energy production rate is the highest with the maximum turbulent intensities, dominated by intense physics

activities (Schlichting 1968; Robinson 1991). Meanwhile, the flow close to the wall is also found to be highly organised, consisting of regions with alternating high- and low-speed fluid motions (Kline et al. 1967; Smith & Metzler 1983).

A consensus on the small-scale turbulence is its ‘universality’. It has long been taken for granted in theoretical approaches (Kolmogorov 1941) and investigated in detail in both numerical simulations (reviewed in Ishihara et al. 2009) and experimental studies (reviewed in Sreenivasan & Antonia 1997). In wall-bounded turbulent flows, the outer region convects energy containing large scales, while the small scales down to Kolmogorov ones gathering at the inner near-wall region are less energetic and have long been regarded as ‘universal’.

Past observations are that all near-wall turbulence behaves similarly in a self-sustained manner. It is believed that there exists a near-wall self-sustaining mechanism (Jiménez & Moin 1991; Hamilton, Kim & Waleffe 1995; Jeong et al. 1997) where the turbulence should be independent of the outer fluid motions. The near-wall autonomous cycle is observed in Jimenez & Pinelli (1999). It is demonstrated through statistics of numerical simulations that a near-wall cycle exists to be local and does not depend on the outer flow. The cycle involves streamwise vortices extracting energy from the mean flow to generate longitudinal velocity streaks, which in turn produce inflectional instabilities for the secondary vortices. In this way, the near-wall flow field is seemingly independent of Reynolds numbers or external flow configurations.

It is also noted by Jimenez & Pinelli (1999) that the near-wall autonomous cycle is presumably not the only mechanism but the dominant one. It self-maintains in the absence of any outer flow with little Reynolds number effect in their studied

cases at moderate Reynolds numbers $Re_\tau = u_\tau \delta / \nu$, which is based on the wall friction velocity u_τ, the half channel height δ and the kinematic viscosity ν, reaching around 600. They noted that other mechanisms that contribute to weaker phenomena could presumably exist. The Reynolds number effect of the outer flow remained at that time unclear at much higher Reynolds numbers.

The local near-wall behaviour is believed to exist with limited length scales (typically in the order of 100 in wall units) and thus is usually studied by direct numerical simulations in truncated domains as minimum flow units (MFU) in Jiménez & Moin (1991) and Jimenez & Pinelli (1999), for example. It is found that the near-wall turbulence can sustain in local simulation units and can be accurately predicted regarding low-order statistics. More recently, Carney, et al. (2020) focus on non-flow interfacing between a near-wall patch and its global-domain environment. A fringe layer is introduced for which the boundary conditions and a transitional forcing are established based on the time-mean momentum balance. The ability of the near-wall patch in capturing and resolving the self-sustained 'universal' dynamics is clearly demonstrated, and the challenges associated with the patch in capturing the outer large-scale influence are also underlined.

2.1.4 Boundary Layer Transition

The concept of the turbulent boundary layer (TBL) is introduced by Prandtl (1904) with its prevalence in a wide range of real-life practices. Generally, the boundary layer develops from an initial laminar state via a transition route towards a fully turbulent state. Natural laminar-to-turbulent transition usually triggered by Tollmien–Schlichting (TS) waves is spatially exceptionally long as it follows the

complete route of evolution from primary disturbances to secondary instability (Sayadi, et al. 2013) and is extremely sensitive to external disturbances (Tani 1969).

It is noted that in many experimental studies, in order to trigger the transition to obtain a TBL, the forced bypass transition has been widely explored and relevant experience has been established based on carefully designed trips for the TBL development. It is widely accepted that tripping elements (e.g., roughness elements) can induce rapid transition via a linear amplification of, or directly bypass the primary instabilities (Reshotko 2001). In this way, the roughness elements can be typically regarded as tripping to not only shorten the transition process but also to ascertain the inception of rapid bypass transition to TBL. In those experimental studies, the influence of the different tripping devices including wires, grits, and pins on the downstream turbulent regime is scrutinised by Erm and Joubert (1991). Some rather simple tripping devices, for instance 2-dimensional (2-D) simple step roughness elements, have been proven to be relatively successful (Klebanoff & Tidstrom 1972). This type of roughness-induced bypass transition results from the forced generation of flow instabilities (Wu, et al. 2019) as reviewed by Kadivar et al. (2021). The process involves the formation of vortical structures which will eventually break down and evolve into hair-pin-type smaller-scale vortices in the turbulent regime (Brinkerhoff & Yaras 2011). The early stage of instability involves the growth of flow separation-associated vortical structures over the tripping element.

2.2 Numerical Simulations and Turbulence Modelling

2.2.1 Computational Cost of Numerical Simulations

Along with the rapid development in the capacity and the potential of those High Performance Computers (HPCs), more advanced simulation techniques have become available. Computational Fluid Dynamics (CFD) is playing an increasingly important role to support fluid dynamics research and development. The high-fidelity simulations would help analyse and predict highly turbulent fluid behaviours to provide guidelines for engineering design or even replace impregnably expensive experiments on certain occasions.

Moore's law (Moore 1965) hypotheses a doubling per year in the number of components per integrated circuit and indicates the rapid development of modern computers. Initially proposed in 1965, and projected to continue for at least a decade, Moore's law has witnessed the plausibly unstoppable growth of computing power nourishing the development of CFD. However, it has probably been approaching a slowing-down 'curbed' stage due to the physical limitations of integrated chips (Eeckhout 2017) since the early 2010s. Thus, envisioning the future of CFD and the computational power with limited growth speed, more efficient CFD methods are generally desired.

The most accurate method to numerically approach the solutions of the Navier-Stokes partial differential equations as the governing equations of a continuous fluid (under Eulerian specification) is apparently to numerically solve them under the high-resolution discretisation. This certain CFD method refers to direct numerical simulations (DNS) introduced by Orszag (1970), resolving stirrings

of fluids from the largest to the smallest dissipating eddies (Figure 2.3). The high-fidelity DNS should be excessively accurate as long as the numerical approximations are negligible, given that not a single modelling assumption is introduced.

To satisfy the spatial discretisation requirements of DNS, two requirements should be met. First, the product of the number of mesh points N times a mesh spatial increment h along a given direction should cover the integral scale length L, as

$$Nh > L \tag{2.5}$$

Second, the spatial increment h should be smaller than the Kolmogorov micro-scale η as introduced in equation (2.4) as

$$h \leq \eta \tag{2.6}$$

These two requirements directly address the upper and lower bounds of the physical scales to resolve. As a result, the DNS of turbulent flows has been challenging especially under a high Reynolds number condition, on which occasion the disparity of scales is magnified. The wall-bounded highly turbulent flows are particularly demanding computationally due to a wide range of temporal and spatial length scales involved, from very large eddies scaling with the main flow path down to local Kolmogorov micro-scales.

Consequently, the computational cost of the wall-bounded turbulent flows in terms of mesh count roughly scales with the Reynolds number as $O(Re^3)$

(Jimenez 2003) for DNS. Thanks to the rapid development of scientific computing technologies, high-fidelity DNS studies relying on supercomputer clusters have provided credible and meaningful results helping academia to understand intrinsic fluid physics (e.g., Jiménez & Moin 1991; Moser, et al. 1999). However, DNS to resolve all turbulence scales are so far still prohibitively expensive for Reynolds numbers of practical interest.

2.2.2 Resolving and Modelling Turbulence

In engineering practice, given the computational capability at the current stage, Reynolds Averaged Navier-Stokes (RANS) approach is still the most popular pathway to simulate high Reynolds number cases. RANS models solve only the time-averaged flow field. For a given instantaneous value with the time mean component (denoted as ' $\overline{\boldsymbol{u}}$ ') plus the fluctuation part (denoted as '$\boldsymbol{u}'$'):

$$\boldsymbol{u} = \overline{\boldsymbol{u}} + \boldsymbol{u}' \tag{2.7}$$

If the ensemble averaging is applied to the governing Navier-Stokes equations, due to non-linearity, namely the Reynolds stress term as a symmetric tensor can be obtained. The idea of the RANS approach is to separately work out the Reynolds stress term based on the Boussinesq hypothesis (Boussinesq 1877), through Reynolds stress models (Hallback et al. 1989), Spalart-Allmaras models (Spalart & Allmaras 1994), $k-\epsilon$ models (Launder & Spalding 1974), $k-\omega$ models (Wilcox 2006), etc. Given that only the time-averaged flow is studied via the involved modelling techniques, the computational cost of RANS is widely regarded as being insensitive

to the increase of the Reynolds number. The mesh count of the turbulent boundary layer flows roughly scales with Reynolds number as $O(Re^{0.4})$ (Chapman 1979) for RANS.

With the rapid development of computing power since then, a much lower level of modelling is expected to be involved with higher fidelity being expected in the scale-resolving numerical simulations. At a sufficiently high Reynolds number, the small-scale motions should be statistically 'universal' according to the Kolmogorov theory (Kolmogorov 1941), and thus could be approximated and modelled. Meanwhile, the large-scale unsteady motions transporting the majority of energy can be fully resolved. Smagorinsky (1963) introduced Large Eddy Simulations (LES). Overall, the LES approach filtering small scales to be modelled at a sub-grid level is a less costly alternative to DNS with generally clear and consistent modelling fidelity (Sagaut & Deck 2009).

In order to retain the large-scale portion of the flow variables with the small-scale modelled, a filtering operator is applied. In most of the implicit filters (explicit filters, see Lund 2003) as widely implemented in commercial solvers, only the filter width Δ is specified, which usually directly correlates with the mesh grid spacings. This is the characteristic scale for large ones to be retained and resolved. In brief, the mesh-grid discretisation and the low-pass characteristics of the operators act together as the implicit filter to decompose and separate the resolved and modelled. Note that in a properly resolved LES case, the contribution of the small-scale modelled part should be trivial.

Through scale-resolving the large scales, LES is generally regarded as a more accurate method than RANS in revealing the actual fluid physics of the

instantaneously active flow fields, yet at the same time takes more computational expense given finer mesh requirements and time-marching restrictions. The mesh count required for LES in wall-bounded flows scales with the Reynolds number roughly as $O(Re^2)$ (Mizuno & Jiménez 2013). Thus, the cost of full LES computations, though considerably lower than DNS as $O(Re^3)$, is still far too high for wide engineering applications (Jimenez & Moser 2000). Even with the projected increase in computer processing power, the challenging situation will remain in a foreseeable future. In 1997, Spalart, et al. (1997) sized up the common computational cost of an LES for the wing of a commercial aircraft. Even under their highly optimistic assumptions, the number of grid points and time steps is out of reach for simulations at the moment given the limited computational resource. More than two decades later, the issue remains, even with the rapid development of computer engineering. The report produced by a renowned expert panel (*CFD Vision 2030 Study*, Slotnick et al. 2014) projects that LES will not be widely applicable and technically mature until the early 2030s. It also foresees a promising future for CFD urging for the progress of hybrid turbulence modelling, expecting a massive reduction of computational cost simultaneously with the fidelity secured. In other words, multi-scale approaches are expected to explore the implementation of various turbulence models in different flow regions as per disparate turbulence length scales.

2.2.3 Near-wall Modelling

For wall-bounded turbulence, of great relevance and interest is the near-wall region. This is where the turbulence activities are most intensive, not only in terms of the level of turbulence but also in terms of the dynamics affecting the overall time-

mean flow performance. This is also where the required resolution is the highest due to the very small spatial and temporal scales of turbulence fluctuations. Consider a near-wall region to compare LES with DNS. The local Kolmogorov micro-scales are naturally smaller than those usually set by typically modelled sub-grid scales in LES. As a result, the mesh resolution of a wall-resolved LES would approach that of a DNS in the near-wall region, as suggested by Moin & Jimenez (1997) and Jimenez & Moser (2000). Being the main culprit of high mesh count requirement, the near-wall region becomes a focal part for which the development of approaches with different fidelities and costs has evolved.

A pearl of prevalent wisdom based on past observations is that all near-wall turbulence behaves similarly in a self-sustained manner. The seemingly ‘universal’ autonomous behaviour as observed provides a strong impetus to develop a modelled, instead of resolved, treatment for the near wall turbulent flow region. This consideration leads to the development of the hybrid approach with a scale-resolving outer flow region coupled with a modelled (typically with a RANS model) near-wall region, notably by the work of Spalart, et al. (1997), as overviewed by Spalart (2009).

The detached eddy simulation (DES) with RANS wall modelling is first introduced by Spalart, et al. (1997). Since its birth, the DES approach has been widely implemented in engineering practice as a decent compromise to LES, but meanwhile has kept being challenged and has been facing various issues. Spalart (2009) reviewed the early starting point of the DES development and mentioned major weaknesses of the model, including the practical issues as well: grid-induced separation and logarithmic-layer mismatch. Unexpected early flow separation can be

induced by arbitrary mesh grid spacings. Besides, a mismatch of the mean velocity profile in the log-layer in a fully developed turbulent channel flow is observed in high-Reynolds-number cases. The velocity profile is seemingly not able to be corrected through mesh refinement, and the issue is instead adversely aggravated. In this case, DES seems to be incapable of showing general mesh convergence.

In order to tackle these issues, the ‘delayed DES’ (Spalart, et al. 2006) and ‘improved delayed DES’ (Shur, et al. 2008) are introduced and developed to fix the early separation and the log-layer mismatch, respectively. Throughout the development from DES to the ‘improved delayed DES’, the existing issues have practically been dealt with. However, regardless of how the models can be revised for improvement, the bottom-line issue of the hybrid approach is unreached. The conceptual issue is raised as: the coefficients of the empirical models are adjusted and tuned as per the recognised wrongly produced mismatched solutions rather than a one-off calibration based on valid and credible databases. In the RANS-LES-switching region referred to as the ‘grey area’, plausible result-based parameter tuning is playing the role rather than a general criterion and standard. The switching has never been clean and abrupt, which would, by all means, be challenging to agree on a uniform theory, given the apparent disparity between the modelled mean flow and scale-resolved instantaneous outer flow. As an example of the existence of a ‘grey area’, the velocity fluctuations near the wall can be double accounted for by the RANS models and the LES resolutions as addressed in Hickling & He (2021).

Overall, the development of wall-modelled LES (Cabot & Moin 2000; Piomelli & Balaras 2002; Spalart 2009; Larsson, et al. 2016; Bose & Park 2018) makes scale-resolving turbulent flow solutions feasible for various practical

applications, though solution accuracy and applicability are restricted expectedly by the empirical nature of the near-wall RANS modelling as well as by how the transition from a scale-resolving outer flow region to a modelled near-wall region is realised.

2.2.4 Numerical Inflow Conditioning for Turbulent Boundary Layer

As introduced in section 2.1.4, a boundary layer naturally develops from the laminar state through a transition towards a fully turbulent status. In many cases of scale-resolving numerical studies, if only the fully turbulent portion is of interest, the pre-requisite to numerically studying the TBL flow is to have a properly initiated turbulent flow regime. A popular way to avoid a much-too-long transition route from laminar to turbulent (Sillero et al. 2013) is to recycle and rescale the downstream characteristics to generate synthetic turbulent inflow conditions (Lund, Wu & Squires, 1998). In so doing, the aimed Reynolds number can be reached efficiently with the turbulent profile rescaled from downstream. However, these forms of non-physical approximation introduce a certain level of arbitrariness that the artificial inflow does not reveal the true history of turbulence development but depends on the future evolution from which it should start (Schlatter and Orlu 2010). Other synthetic inflow generation methods include those built on theoretical properties of well-developed turbulence (Kraichnan 1970) and empirical information (Jarrin, et al. 2006; Adler, et al. 2018). Above all, these methods all facilitate efficient calculations in truncated domains yet lack physical coherence and usually require a long distance for the artificial history effects to be removed.

Schlatter and Orlu (2012) introduced an artificial tripping method with a function constructed to exert a volume forcing to trigger a rapid transition. By tuning the representative parameters, a fully developed boundary layer can be seemingly generated almost immediately after the trip, with ‘optimal configurations’ (Hutchins 2012). On the one hand, the optimal tripping in numerical simulations, unlike real-life experiments, takes advantage of the synthetic nature to minimise the spatial length for developing towards a full equilibrium turbulence boundary layer. On the other hand, the optimised tripping function is based on a ‘collective history’ from the tuning procedure instead of a true development history from which the flow is physically transitioned. Therefore, the artificial tripping may not easily correspond to specific set-ups, and thus lack general transferability and comparability with experimental studies. Besides, there is little chance for the optimal tripping to be linked to many practical situations where the corresponding boundary layer flows cannot be idealised as a fully developed boundary layer in an equilibrium state. In fact, an under-developed non-equilibrium TBL may well affect a considerable part of the flow field with a non-negligible impact on aerodynamics performance (e.g., Wheeler, et al. 2018). It is recognised that generating effective artificial inflow conditions is needed for studying a fully developed TBL at a high Reynolds number in a truncated domain. An easily implementable physical tripping method should be explored to cover also a non-equilibrium part of the TBL leading to a fully developed equilibrium one with reasonable controllability and comparability to physical experiments.

It is worth noticing that in contrast to many previous experimental studies, very few efforts (e.g., Boudet, et al. 2015) have attempted to resolve properly

physical trips in numerical simulations for TBL inflow generation. As mentioned, the early stage of instability involves the growth of vortical structures over the trip. Therefore, it is necessary to locally resolve the associated flow instabilities at different frequencies in the numerical simulations. In this context, one may concern if and how much extra computational resource would be required to fully resolve a local roughness element for tripping in the numerical simulations.

Another relevant aspect of inflow conditioning is the physical behaviour and impact of those tripping-induced large-scale disturbances. One may ask where in a boundary layer these large-scale disturbances reside, how they evolve streamwise and if they influence the near-wall turbulent flow development. These issues are particularly of interest in the light of the influence of large-scale coherent structures in outer flow (log-law region) on the near-wall region for well-developed wall-bounded turbulent flows (e.g., reviewed in Marusic, et al. 2017, to be introduced in section 2.3). An overly disturbed boundary layer with a trip of large size can lead to rather persistent large structures in an outer flow region much further downstream of a TBL, as experimentally observed by Marusic, et al. (2015). The sizing of the tripping element thus deserves attention. In general, it would be of interest to see how those tripping-induced large-scale disturbances behave in comparison to those outer flow coherent structures in a well-developed TBL.

2.3 Recent Progress in Understanding Wall Turbulence

Noteworthy is the significant progress in the fundamental understanding of wall-bounded turbulent flows at high Reynolds numbers made in the past decade or so through both advanced experimental measurements and high-resolution DNS

analyses. An emerging new consensus recognises that the near-wall turbulence behaves distinctively with some interesting ‘dual’ characteristics. In addition to the self-sustained ‘universal’ behaviour and dynamics, there is a clear Reynolds-number-dependent part, which seems to be largely passive as influenced by large-scale coherent structures in the outer flow region.

2.3.1 Outer Plateau in Energy Spectrum

Along with the rapid CFD development of both numerical methods and computational resources, a soaring number of DNS calculations are available to help better understand high Reynolds number turbulence. Lee & Moser (2015) published the database of DNS results in canonical incompressible channel flows with a range of friction Reynolds numbers up to $Re_\tau = 5200$, where $Re_\tau = u_\tau \delta / \nu$. Figure 2.4 demonstrates the generated one-dimensional pre-multiplied energy spectra from the DNS database. The energy spectra present a clear picture of the two distinctive parts of interest: the ‘universal’ first energy peak near wall and the departing second peak in the outer flow with increasing Reynolds numbers.

Figure 2.4 first shows the ‘universality’ of the first energy peak regarding the core location at around $y^+ \sim 13.5$ independent of Reynolds number. Clearly, the near-wall universal first peak is associated with the near-wall small scales with short wavelengths. These small scales are engaged in the near-wall self-sustained autonomous cycle as discovered by Jimenez (1999).

In contrast to the near-wall small scales, there is a clear Reynolds-dependent part away from the wall with increasing y^+. This second peak (namely the outer ‘plateau’ in some contexts) demonstrates in Figure 2.4 a clear departure with the

increment of the Reynolds number. The wall-normal location of this second peak is discovered to scale with the square root of the boundary layer thickness or the half-channel height in wall units as $(\delta^+)^{0.5}$. The dominant wavelengths of the large-scale coherent structures follow a similar scaling trend. Therefore, one can expect the energy peak associated with the large-scale structures to increase with λ^+ and y^+ (Marusic, et al. 2017).

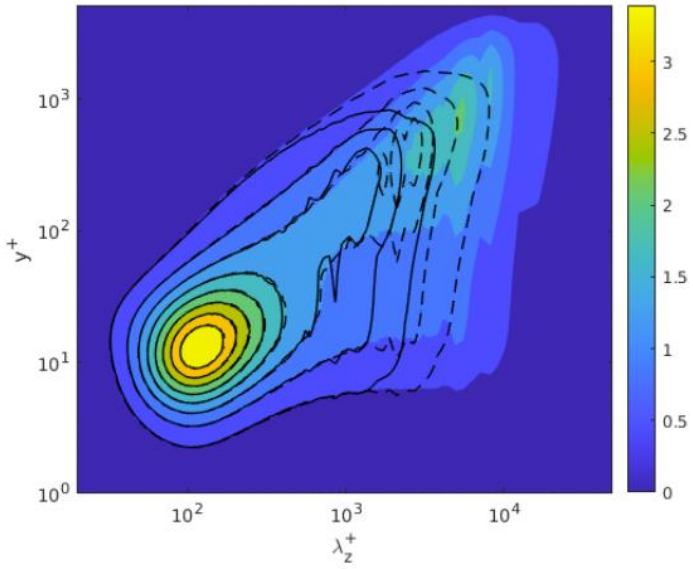


Figure 2.4. **One-dimensional pre-multiplied energy spectra reproduced from DNS data (Lee & Moser 2015) with respect to spanwise wavelengths at $Re_\tau \approx$ 1000 (solid lines '—'), 2000 (dash lines '— —') and 5200 (shaded contours).**

For decades, the 'universality' of the complete near-wall inner region is accepted, providing a valid rationale for various wall-modelling techniques. However, the outer energy peak as a manifestation of the existence of outer large-scale coherent structures puts some concerns on whether and how these structures would influence the inner layer. In fact, they exert a Reynolds-number-dependent

impact in the way of ‘foot-printing’ and ‘modulation’ on the near-wall long wavelength part in the energy spectra.

2.3.2 Foot-printing and Modulation

An important aspect is the ‘foot-printing’ in the near wall turbulence by the large coherent structures far away from the wall. The velocity field below the buffer region exhibits clear signatures of the long streaky outflow structures, as revealed in experiment data (Hutchins & Marusic 2007; Marusic et al. 2010) and DNS results (Jimenez 2013; Bernardini, et al. 2013; Agostini & Leschziner 2014; Lee & Moser 2015). As illustrated in Figure 2.5 as plotted in wall-parallel planes, the inner and outer flows are highly correlated as a manifestation of the ‘foot-printing’ phenomenon. The instantaneous velocity fields are extracted at the inner and outer locations with different wall-normal distances in Figure 2.5(a) and (b), respectively. These are essentially the raw fields for further data processing in Figure 2.5(c) and (d). Marusic et al. (2017) demonstrate the implementation of the Empirical Modal Decomposition (EMD) method, serving as a filter to retain large-scale structures. The corresponding shorter wavelengths are thus filtered out under the long-wavelength-pass filter in Figure 2.5(c) and (d), generated from the raw fields in Figure 2.5(a) and (b), respectively. In this way, the correlation between the inner and outer flow fields is clearly demonstrated.

The inner large scales are actually the ‘foot-prints’ of the outer long streaky coherent structures, given the fact that they will immediately decay and diminish after the removal of outer energetic large scales (Carney, et al. 2020). While on the other hand, the outer coherent structures can be reproduced and accurately predicted

as if in the way without the inner, where the near-wall structures are replaced by a mimicking off-wall boundary condition synthesised from a rescaled flow plane (Mizuno & Jimenez 2013) indicating that the outer flow field should be independent of the near-wall dynamics. The 'foot-printing' behaviour is argued to be quasi-steady locally in a very near-wall region (Zhang & Chernyshenko 2016; Agostini & Leschziner 2016a).

Additionally, the near-wall turbulence seems to be subject to some interactions between local small scales and those large 'foot-prints', through a 'modulation' (Mathis, et al. 2009), an aspect subject to some further analyses and discussions (Talluru, et al. 2014; Baars, et al. 2017; Agostini & Leschziner 2019).

These recent findings on near-wall turbulence have certainly provided some extra challenges to existing modelling approaches and underlying wisdom. Some new wall-modelling efforts are sought to recognise the distinctive scale-dependent behaviour as observed, by generating a synthetic boundary condition to mimic the wall effect (Mizuno & Jiménez 2013), or super-imposing the traditional 'universal' part and the Re-dependent passively influenced part (Marusic, et al. 2010; Agostini & Leschziner 2016b, and Wang, et al. 2021). Typically, modelling efforts of this kind are based on and tested against a single or a small set of DNS data, and the Reynolds number dependency of their applicability remains to be a main issue of interest.

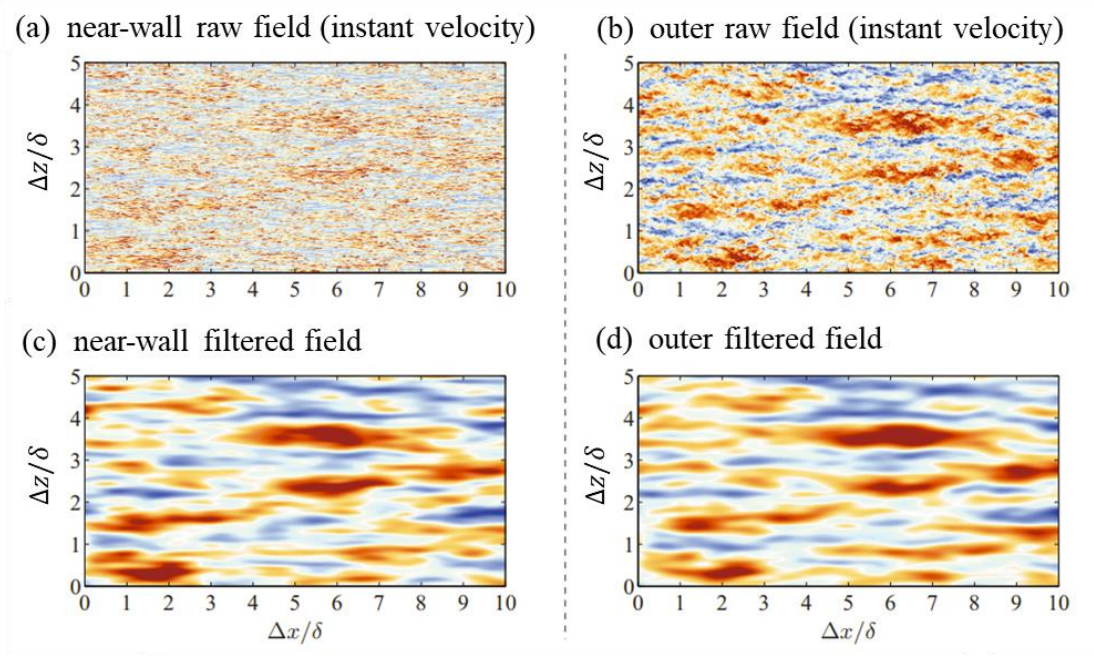


Figure 2.5. **The foot-printing effect illustrated in Marusic et al. (2017) (a) The original raw inner flow field. (b) The original raw outer flow field. (c) The filtered inner flow field. (d) The filtered outer flow field. The streamwise and spanwise directions are denoted as *x* and *z*, respectively.**

2.3.3 Minimum Flow Unit Approach

It is recognised that there have been some previous efforts in developing scale-resolving near-wall turbulent flow in a small local truncated domain. Pascarelli, et al. (2000) develop a method to couple a global coarse-mesh outer flow domain with a local small fine-mesh near-wall block, which is often labelled as 'Minimum Flow Unit (MFU)' with direct periodic conditions in the two wall-parallel directions. Their corresponding instantaneous global near-wall flow field is created by mapping the local solution of a small fine-mesh block (MFU) solution directly periodically in space. The resultant instantaneous near-wall flow is thus subject to the artificial

signatures of the imposed spatial periodicity with the small block length and width, which are clearly incompatible with the ‘foot-prints’ of the outer flow large-scale coherent structures. Tang & Akhavan (2016) adopt a two-domain ‘nested’ system with an MFU fine-mesh block and a coarse-mesh domain for a channel flow. The two domains are solved separately without direct interfacing but coupled by rescaling the flow instantaneously based on spatially averaged quantities. The spatial averaging would smear out any spatial structures in the global domain, thus diminishing the source of the ‘foot-printing’ of the large scales on the local fine-mesh domain. In addition, the coarse-mesh domain in the near-wall region, though rescaled by the fine-mesh solution in the minimal unit domain, would be subject to large discretisation errors due to the under-resolved mesh. Sandham, et al. (2017) develop a method on two distinctively separated scales. The near-wall flow solutions are obtained in discrete non-space filling fine-mesh ‘patches’ which interact with the global coarse-mesh domain by providing instantaneous wall-tangential boundary conditions without any cross flow to each other. The near-wall coarse-mesh domain is obviously under-resolved. A common key limitation suffered by those previous local-domain-based methods seems to arise from the use of a near-wall MFU subject to the spatial periodic conditions, inherently impeding the ‘foot-printing’ by large-scale turbulence structures in an outer flow region. Without the ‘foot-prints’, a ‘modulation’ of near-wall flow has no starting point.

2.4 Summary

This chapter provides a brief literature review on the basics of turbulence emphasising the various length scales involved in high-Reynolds-number wall-

bounded turbulent flows and the resulting difficulty and challenge in resolving them numerically. The prevalent wisdom in modelling the near-wall high-resolution requested portion to reduce the overall computational cost is highlighted, with also its ongoing technical issues addressed. It is noted that recent progress in understanding the wall turbulence prompts a new impetus for modelling development to capture and resolve the Reynolds-number-dependent influence of outer flow on near-wall turbulence in terms of the ‘foot-printing’ of the large-scale coherent structures and the scale-interaction associated ‘modulation’.

We are trying to develop a method capable of receiving the outer flow influence on the near-wall inner flow field. The potential advantage of the methodology taken in this thesis over many previous MFU approaches is to overcome the common limitation of artificial spatial periodicity enforced as the unit boundary conditions becoming profoundly incompatible with the prevalent ‘foot-printing’ of large scales from the outer flow on the near-wall flow, as the large-scale structures are inevitably truncated by the domain lengths of the MFU.

Besides, when implementing the two-scale source-term oriented framework to the canonical channel flows and the boundary layer flows for conditioning the deemed under-resolved near-wall region, different source-term mapping strategies can be expected, given whether or not global homogeneity holds in the streamwise direction. In many cases, the flow develops gradually (e.g., turbulent boundary layer) and the mean field can be accurately reproduced through coupling with sampling embedded domains with no need to introduce the detailed local distributions and breakdowns of all the viscous stresses, heat, and work fluxes (He 2021). Extra attention should be placed when the development of flow is experiencing any abrupt

change on the mean flow field in which case the flow history could be affecting the downstream greatly. Local activities should be scale-resolved and investigated on whether they are leaving non-trivial history effects on the downstream.

This chapter also reviews the fundamental physics of laminar-to-turbulent transition and the means to initiate TBL in numerical simulations. A clearly and consistently applied inflow condition should be studied with the two related issues: firstly, how much mesh resolution should be required if a physical tripping element for triggering bypass transition were to be numerically resolved; secondly, how those tripping-induced large-scale disturbances behave physically compared to those outer flow coherent structures in a well-developed TBL. More specifically, would the tripping-induced large-scale disturbances have a significant 'history effect' on the downstream, also would they influence the corresponding near-wall turbulence?

Overall, the objective and motivation of this thesis to develop, implement and validate an efficient two-scale method for wall-bounded flows should be articulated with a clear comparison of the cost - Reynolds number scaling between the existing and present approaches.

3 METHODOLOGY

In this section, the two-scale methodology is introduced, starting from an example in a simple case as the canonical channel flow in the first three sections then to an extension to the streamwise-developing turbulent boundary layer flow in section 3.4 with the focus on solution propagation in the non-homogeneous spatially evolving direction. The overall framework for the channel flows is introduced in section 3.1. The two attributes related to the first two research questions are highlighted, regarding how the locally embedded fine-mesh blocks could be enabled to receive the influence of outer large scales, and also, how the under-resolved global-coarse-mesh near-wall region could be conditioned with the minimised discretisation errors. These two aspects will be discussed in detail in section 3.2 and 3.3, respectively.

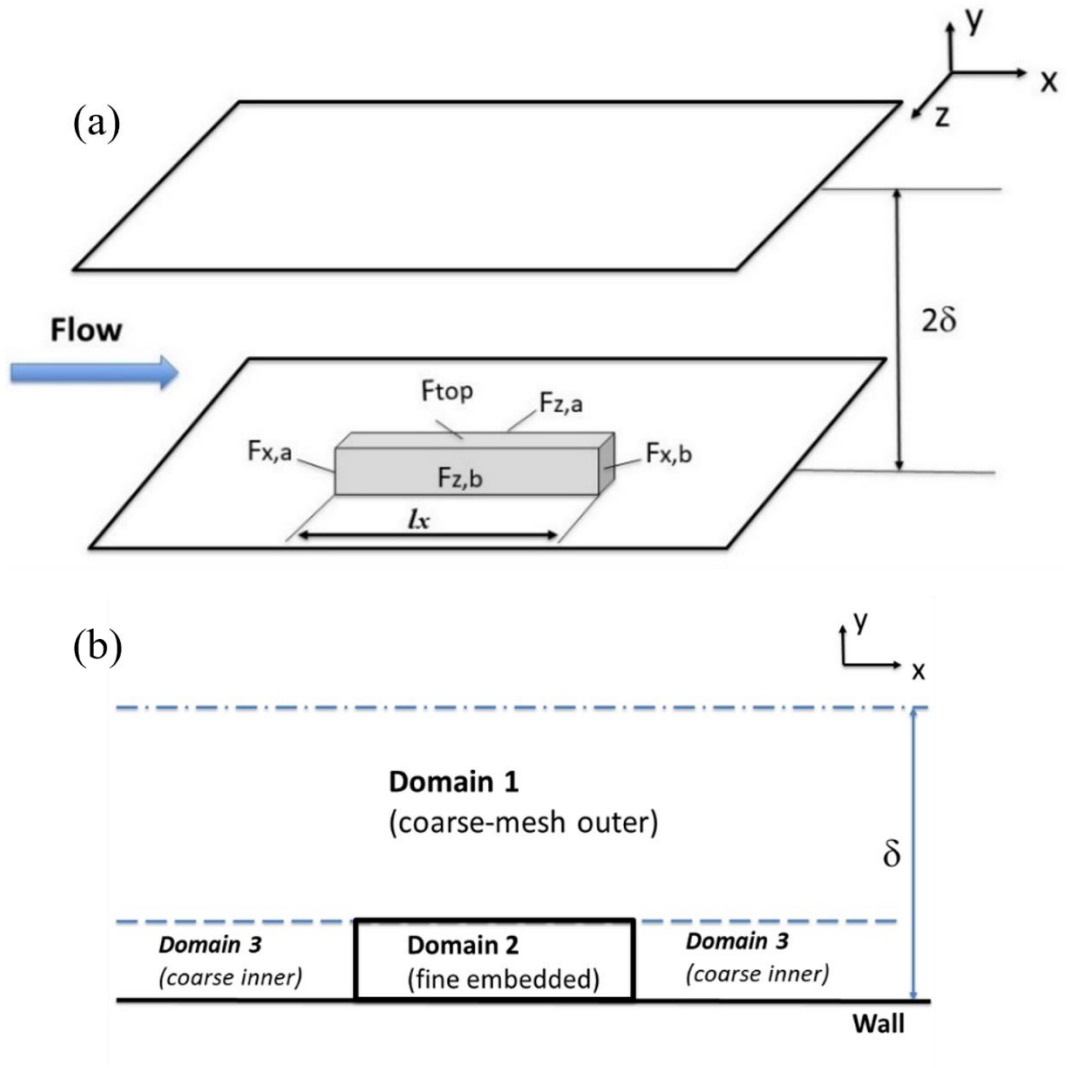


Figure 3.1. **Domain configurations for the channel flow with a locally embedded block.**

3.1 Overall Framework

A canonical channel flow domain is partitioned as shown in Figure 3.1. Phenomenologically, the two-scale method needs to be capable of capturing and resolving all key influences and interactions between and within corresponding domains as indicated in Figure 3.2. Firstly, we assume that the coarse mesh in the

global outer domain will be fine enough to resolve coherent large-scale turbulence structures in the log-law region. Thereafter, close attention is paid to two key considerations pertinent to the present work:

1) The local embedded fine-mesh domain should be able to receive the influence ('foot-printing') of the large-scale turbulence structures of outer flow.
2) The global inner coarse-mesh domain ('Domain 3' in Figure 3.1b) is under-resolved, and thus the corresponding discretisation errors need to be minimised.

For 1), the embedded block will have to be directly interfacing with the global coarse-mesh domain. This will certainly be the case for the top face of the local fine-mesh block (F_{top} as shown in Figure 3.1a). For the upstream and downstream faces ($F_{x,a}$ and $F_{x,b}$) and the spanwise side faces ($F_{z,a}$ and $F_{z,b}$), direct periodic conditions as in commonly adopted MFU are deemed not to be suitable as the resultant periodic flow patterns in the two directions will be clearly incompatible with the large-scale coherent turbulence structures of the outer region, thus impeding the 'foot-printing'. A key enabler adopted in the present work is a scale-dependent interface method in which the periodic condition is only applied for fine-scale fluctuations. As such, the large scales of the global coarse-mesh region can now directly interact with the local fine-mesh block to capture both the 'foot-printing' and the 'modulation' effects, as will be described in section 3.2.

For 2), the correction on the global coarse-mesh domain in the near-wall inner region is enabled by upscaling the fine-mesh solution to the corresponding coarse-mesh cells. The forcing source terms resulting from the upscaling in the local

embedded region are then simply mapped to the global inner domain to drive the coarse-mesh solution. The corresponding upscaling method with the source term generation will be described in section 3.3.

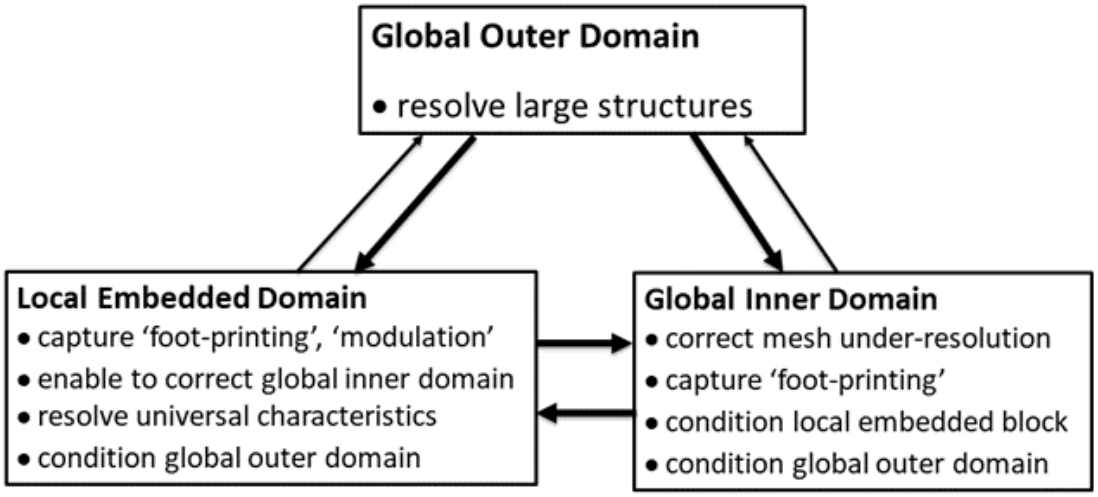


Figure 3.2. **Domain-domain influence and interaction in a two-scale framework.**

3.2 Dual Meshing and Interface Treatment

As shown in Figure 3.1, a local near-wall fine-mesh block is embedded in a global coarse-mesh domain. The dimensions of the local embedded block are given by the streamwise length l_x, the corresponding spanwise width l_z and the wall normal height l_y, in the x, z, and y directions respectively.

The local fine-mesh block is created by simply subdividing the corresponding coarse-mesh cells in the near-wall region. This dual-mesh system is purposely introduced to facilitate effectively the interactions between the local embedded fine-mesh block and the global coarse-mesh inner region.

A basic consideration for an interface treatment is flux conservation. For the present embedded meshing for the fine mesh block, there will be non-conforming hanging mesh nodes at the interface. The interface conservation is realised through the non-conforming arbitrary mesh interface (AMI) patches based on the Galerkin projection (Farrell & Maddison 2011).

Furthermore, two types of interface treatments are considered. For the interface at the top face of the embedded block (F_{top} as marked in Figure 3.1a), the baseline AMI treatment will pass the full flow variable data directly between the coarse-mesh and the fine-mesh sides, effectively by interpolation.

For a pair of side faces (either $F_{x,a}$ and $F_{x,b}$, or $F_{z,a}$ and $F_{z,b}$ as marked in Figure 3.1a), the interface treatment needs to accommodate both the large-scale signatures passed on from the coarse mesh side, and at the same time avoid accuracy loss due to the under-resolution of the coarse mesh. Noting that the fine-mesh is effectively a 'sub-grid' in relation to the local under-resolved coarse-mesh, we adopt a scale-dependent periodic condition treatment. An instantaneous full flow variable is decomposed into the coarse-mesh resolved base value and the fine-mesh resolved fluctuation:

$$\boldsymbol{u}(\boldsymbol{x},t) = \boldsymbol{u}_C(\boldsymbol{x},t) + \boldsymbol{u}_f''(\boldsymbol{x},t) \tag{3.1}$$

where $\boldsymbol{u}_C(\boldsymbol{x},t)$ is the coarse-mesh resolved, obtained based on the baseline AMI. For the fine-mesh fluctuation part $\boldsymbol{u}_f''(\boldsymbol{x},t)$, the direct spatial periodic condition is applied. For a pair of block side faces (e.g., $F_{x,a}$ and $F_{x,b}$), we shall thus have:

$$\begin{cases} \boldsymbol{u}_f''(\boldsymbol{x},t)_{x,a} = \boldsymbol{u}_f''(\boldsymbol{x},t)_{x,b} \\ \boldsymbol{u}(\boldsymbol{x},t)_{x,a} = \boldsymbol{u}_C(\boldsymbol{x},t)_{x,a} + \boldsymbol{u}_f''(\boldsymbol{x},t)_{x,b} \\ \boldsymbol{u}(\boldsymbol{x},t)_{x,b} = \boldsymbol{u}_C(\boldsymbol{x},t)_{x,b} + \boldsymbol{u}_f''(\boldsymbol{x},t)_{x,a} \end{cases}$$

(3.2)

Effectively, we have periodic fine-mesh fluctuations for the pairing side faces based on corresponding inhomogeneous instantaneous coarse-mesh variables.

3.3 Two-scale Formulation

We consider the flow governing equations in a simple form for the flow variable vector $\boldsymbol{u}$:

$$\frac{\partial \boldsymbol{u}}{\partial t} + R(\boldsymbol{u}) = 0$$

(3.3)

which in its original form will be directly solved numerically in the near-wall embedded fine-mesh block and in the global coarse-mesh outer domain as intended. For the global near-wall inner region (‘Domain 3’, Figure 3.1b), a set of augmented flow equations need to be introduced to link the global coarse-mesh solution to the local fine-mesh solution of the embedded block. Upscaling is typically referred to as the way to generate an approximate set of equations for a coarse-scale domain of the same form as those for the fine-scale domain (Farmer 2002). In the present two-scale framework, the upscaling is aimed at producing a coarse-mesh solution which approaches a target solution originated from the fine-mesh domain. In the following, we will first use the commonly known time-averaging (Reynolds-averaging) as an illustrative example to introduce the upscaling procedure and show how it may be

cast in two modes for a fine-scale and a coarse-scale domain respectively. We will then describe how to obtain the upscaled equations for the present work based on space-time averaging.

3.3.1 Upscaling for Time-averaging/Reynolds-averaging

We take conventional time-averaging to illustrate the upscaling with augmented equations. In this case, the fine-scale solution can be taken as a direct time-resolved turbulence solution (or detailed unsteady experimental measurement). For application purposes, we may be interested in a solution with a much lower temporal resolution, and in an extreme but very common case, we may only be interested in the solution with no temporal resolution at all (a time-averaged state). Then, the upscaling from the temporally finely resolved unsteady solution to a steady state solution for the corresponding time-averaged flow is considered.

Take a standard temporal decomposition of an unsteady flow variable into a time-averaged and a fluctuation part:

$$\boldsymbol{u}(\boldsymbol{x},t) = \overline{\boldsymbol{u}}(\boldsymbol{x}) + \boldsymbol{u}'(\boldsymbol{x},t).$$

(3.4)

By time-averaging the flow equations (3.3), we have:

$$\overline{R(\boldsymbol{u})} = 0.$$

(3.5)

However, due to nonlinearity, $\overline{R(\boldsymbol{u})} \neq R(\overline{\boldsymbol{u}})$, The equations with the time-averaged flow variables can only be balanced with extra terms:

$$R(\overline{\boldsymbol{u}}) = \boldsymbol{ST}_t$$

(3.6)

where $\boldsymbol{ST}_t$ is a 4-element vector for an incompressible flow. The first element should be zero if the divergence-free is fully achieved for the time-averaged flow. The other elements are three scalars representing the lumped Reynolds stresses in the momentum equations in the three directions respectively. The augmented equations (3.6) are the upscaled flow equations for the coarse-scale domain, with zero temporal resolution in this case. The lumped form of the Reynolds stresses underlines the simple but fundamental way in which the turbulence stresses affect the time-averaged flow by balancing the corresponding upscaled equations.

The upscaling can be expressed in two modes to be applied in the coarse scale (denoted with subscript 'C') and fine-scale domains (subscript 'f') respectively. A 'direct mode' of the time averaging as applied to the coarse-scale domain simply is:

$$R(\boldsymbol{u}_C) = \boldsymbol{ST}_t$$

(3.7)

Here the source term $\boldsymbol{ST}_t$ is taken as the input and the coarse-scale solution $\boldsymbol{u}_C$ is the output. It then follows that as long as we have a correct source term regardless of its origin (empirically, experimentally, numerically or analytically), we will get a correct coarse-scale solution as intended. Alternatively, we can view the upscaled equation in an 'inverse mode' to be used in the fine-scale domain:

$$\boldsymbol{ST}_t = R(\overline{\boldsymbol{u}}_f)$$

(3.8)

In this case, a known time-averaged fine-scale solution $\overline{\boldsymbol{u}}_f$ is taken as the input and the source terms as the output. This is a well-posed problem with the four elements of the source term vector as unknowns and the four flow equations. The source terms are conveniently obtained simply from the flux residual evaluations using the given fine-scale solution. After generating the source terms from the inverse mode, i.e., equation (3.8), and driving the coarse-mesh domain to converge, we will have $\boldsymbol{u}_C = \overline{\boldsymbol{u}}_f$ as intended.

The inverse mode for time averaging itself is rarely used as it seemingly does not serve any practical purpose because one will need to get the fine-scale solution in the first place. The possibility of getting a time-averaged solution through an inverse mode is illustrated for self-excited unsteady flows in the context of trailing-edge edge vortex-shedding (Ning & He, 2001). As will be shown in the following, however, the inverse mode can be effectively utilised when the averaging and upscaling are extended to space as well as time.

3.3.2 Upscaling for the Present Space-time Averaging

In the channel flow domain with distinctive two-scale regions, the flow solution of the fine mesh block is first upscaled to the corresponding coarse-mesh cells by a local volume-weighted averaging. For a coarse mesh cell with m fine mesh cells, the corresponding local spatially averaged coarse-mesh variable is

$$\widetilde{\boldsymbol{u}}_f(\boldsymbol{x},t)=\frac{1}{\Delta v_C}\sum_{i=1}^{m}[\boldsymbol{u}_f(\boldsymbol{x},t)\Delta v_f]_i$$

(3.9)

where Δv_C is the volume of the coarse mesh cell: $\Delta v_C=\sum_{i=1}^{m}(\Delta v_f)_i$.

Similarly to the time-averaging, the upscaled equations on the coarse mesh can only be balanced with extra source terms

$$\frac{\partial\widetilde{\boldsymbol{u}}_f}{\partial t}+R\left(\widetilde{\boldsymbol{u}}_f\right)=\boldsymbol{ST}_s(\boldsymbol{x},t)$$

(3.10)

where $\boldsymbol{ST}_s(\boldsymbol{x},t)$ is effectively the source term vector needed to eliminate the spatial discretisation errors resulting from the under-resolved coarse mesh in order to reach the target upscaled solution $\widetilde{\boldsymbol{u}}_f$ in the coarse-mesh domain. Note that $\boldsymbol{ST}_s(\boldsymbol{x},t)$ is both space and time-dependent. Thus, if one simply propagates the spatial averaging associated source terms to the global coarse mesh domain, there will have to be artificial periodic signatures characterised by the streamwise and spanwise lengths of the embedded block. This is of course to be avoided given the primary intent of the present method development as introduced earlier.

A basic motivating consideration is that for typical wall-bounded turbulent flows, a time-averaged field is much smoother than its unsteady counterpart. Furthermore, for a fully developed channel flow, we effectively have homogeneous statistics in both the streamwise and spanwise directions. This property appeals greatly in relation to propagating the upscaling effect from the local embedded

domain to a global one. We thus introduce space-time averaging to enable the use of the spatially homogenous time-averaged flow in the two directions.

For a coarse-mesh cell embedded with m fine-mesh cells, the space-time averaged flow variable can be simply defined as the local volume-average of time-averaged variables of m fine-mesh cells:

$$\widetilde{\overline{\boldsymbol{u}}}_f(\boldsymbol{x}) = \frac{1}{\Delta v_C}\sum_{i=1}^{m}[\overline{\boldsymbol{u}}_f(\boldsymbol{x})\Delta v_f]_i \tag{3.11}$$

Noting the averaging being a linear operator, we see that the space-time averaging can be also taken as a time-averaging of the volume-averaged on the coarse mesh cell as $\widetilde{\overline{\boldsymbol{u}}}_f(\boldsymbol{x}) = \widetilde{\overline{\boldsymbol{u}}}_f(\boldsymbol{x})$. The upscaled equations in the coarse mesh domain ('direct mode') become

$$\frac{\partial \boldsymbol{u}_C}{\partial t} + R(\boldsymbol{u}_C) = \boldsymbol{ST}_{st}(\boldsymbol{x}) \tag{3.12}$$

The source term $\boldsymbol{ST}_{st}(\boldsymbol{x})$ is time-independent, thus homogeneous in x and z directions. It consists of two parts:

$$\boldsymbol{ST}_{st} = (\boldsymbol{ST}_{st})_f + (\boldsymbol{ST}_t)_C \tag{3.13}$$

The first part is generated by applying the 'inverse mode' of the space-time averaging to the fine-mesh time-averaged solution, with the $R(\blacksquare)$ operator applied on the coarse mesh grid:

$$(\boldsymbol{ST}_{st})_f = R(\widetilde{\overline{\boldsymbol{u}}}_f)$$

(3.14)

The second part is due to the nonlinear time-averaging effect of the unsteady solution on the coarse mesh which needs to be accounted in order to balance the upscaled equation for the targeted space-time averaged solution with the $R(\blacksquare)$ operator applied on the coarse mesh grid:

$$(\boldsymbol{ST}_t)_C = \overline{R(\boldsymbol{u}_C)} - R(\overline{\boldsymbol{u}}_C)$$

(3.15)

With the source terms as defined in equations (3.14) and (3.15), when a scale-resolving turbulent flow solution in the coarse-mesh domain is statically converged with a constant time-averaged state, we will get the following by time averaging the upscaled equation (3.12):

$$R(\overline{\boldsymbol{u}}_C) = R(\widetilde{\overline{\boldsymbol{u}}}_f)$$

(3.16)

Hence, the time-averaged coarse-mesh solution $\overline{\boldsymbol{u}}_C$ should converge to the target space-time averaged fine-mesh solution $\widetilde{\overline{\boldsymbol{u}}}_f$ as intended. The time-averaging is carried out on the fly during the solution (He, 2018).

A flowchart showing the main elements of the present two-scale method as implemented in the OpenFOAM for incompressible flow is shown in Figure 3.3.

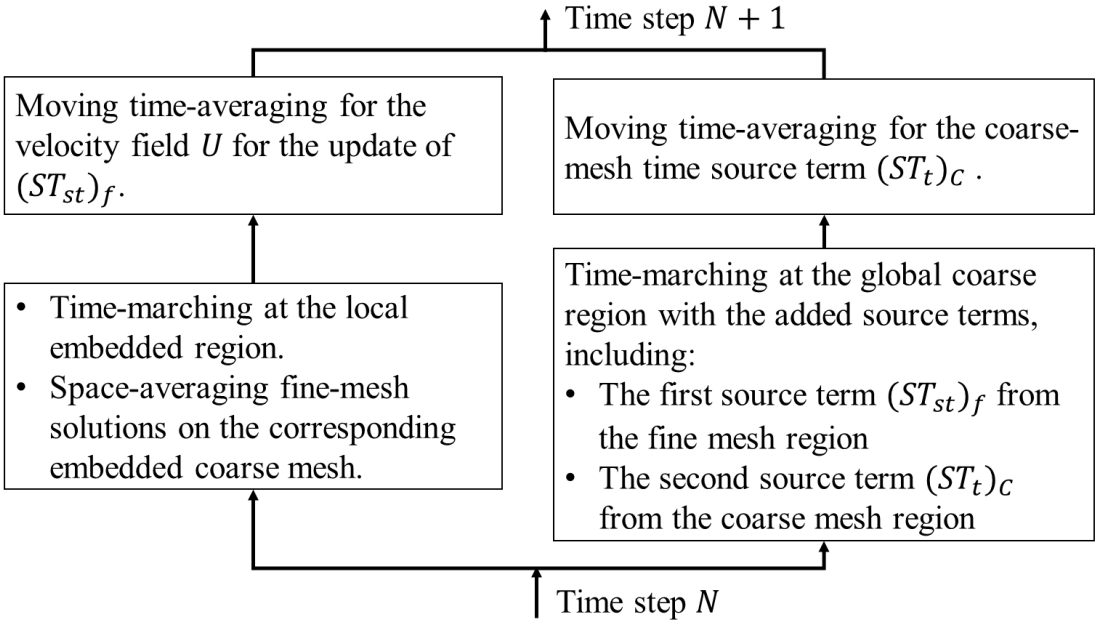


Figure 3.3. **Flowchart of the two-scale solution process as implemented.**

Some extra remarks should be made regarding the source term propagation in the context of capturing the 'modulation'. In the phenomenological discussions so far, the large-scale coherent structures are regarded effectively as an external forcing from the outflow region originating the foot-printing and the modulation within the embedded near-wall block, which will in turn improve the conditioning of both the global inner coarse-mesh region and the outer flow coarse-mesh region. The related assumption is that those intermediate scales generated and affected by the modulation in the near-wall region should have negligible feedback effects on the large scales in the outer flow region. This assumption is deemed to be justifiable based on the present results, as presented in chapter 5. A simple option to further address this will also be introduced and presented in Appendix for completeness.

3.4 Two-scale Block-spectral Method for Turbulent Boundary Layer

As introduced in chapter 2, the way to initiate the turbulent boundary layer (TBL) is of great importance and worthwhile studying. The related issues will be investigated in detail in chapter 6. Here in this section, suppose a TBL is properly initiated by a physical trip, we focus on solving the tripped TBL efficiently and accurately.

Previously in this chapter, the validity for the local solution to be mapped globally is attributed to the spatial smoothness due to time-averaging and the global homogeneity in the two wall-parallel directions for channel flows. For a 2-D TBL, compared with the channel flow, the global homogeneity still lies in the spanwise direction, while the 'local' homogeneity exists due to the smooth variation of the time-averaged flow in the streamwise direction. The local source terms could be analogously generated as a representative of the target space-time-averaged local fine-mesh solutions, which is amendable to spectral propagation to deal with the global streamwise inhomogeneity. Chebyshev and Fourier spectral methods have been widely used in solving differential equations and many other applications of data interpolation (Boyd 2001). The block-spectral (BS) method is applied to inhomogeneous micro-structured surfaces (He 2018; Kapsis, et al. 2020), based on Fourier spectral mapping. The Chebyshev method built on the polynomial group is preferred here for the source-term spectral mapping without requiring any special periodicity. To this end, we resort to the two-scale BS method with locally embedded fine DNS blocks in the near-wall region.

The local fine-mesh DNS blocks embedded in a near-wall region, as illustrated in Figure 3.4(a), are generated by subdividing corresponding coarse-mesh cells. At the inlet to the computational domain, a laminar Blasius profile can be specified to reduce the domain size for the laminar part. The whole computational domain can be divided into three parts as shown in Figure 3.4(b): the global outer flow region (coarse-mesh) where the large-scale structures are directly resolved on the base coarse mesh, the local near-wall DNS blocks (fine-mesh), and the global inner region (coarse-mesh). The key working of the present two-scale method is that the solution in the under-resolved global inner coarse-mesh region will be corrected using the time-invariant source terms originated from local fine-mesh blocks and propagated spatially by block-spectral mapping.

The interface flux conservation between the coarse and fine regions is achieved through the non-conforming arbitrary mesh interface (AMI), introduced in Farrell & Maddison (2011). It is applied directly as the interface condition to the top surface of each embedded block. For a pair of side faces of a block embedded in the developed turbulent region (either $F_{x,a2}$ and $F_{x,b2}$, or $F_{z,a2}$ and $F_{z,b2}$, as marked in Figure 3.4a), a scale-dependent periodic boundary condition is adopted. The local flow variable is decomposed into a coarse-mesh base value and a fine-mesh perturbation as in equation (3.1):

$$\boldsymbol{u}(\boldsymbol{x},t) = \boldsymbol{u}_C(\boldsymbol{x},t) + \boldsymbol{u}_f''(\boldsymbol{x},t)$$

where $\boldsymbol{u}_C(\boldsymbol{x},t)$ is the coarse mesh-resolved, obtained directly via the baseline AMI. For the fine-scale fluctuation part $\boldsymbol{u}_f''(\boldsymbol{x},t)$, the periodic condition is applied.

The scale-dependent interface treatment can also be applied to the spanwise pairing points of the frontal block ($F_{z,a1}$ and $F_{z,b1}$). The upstream boundary of the frontal block ($F_{x,a1}$) is consistent with the global region and assigned with the laminar Blasius profile. The downstream boundary of the frontal block ($F_{x,b1}$) is simply dealt with by the AMI treatment.

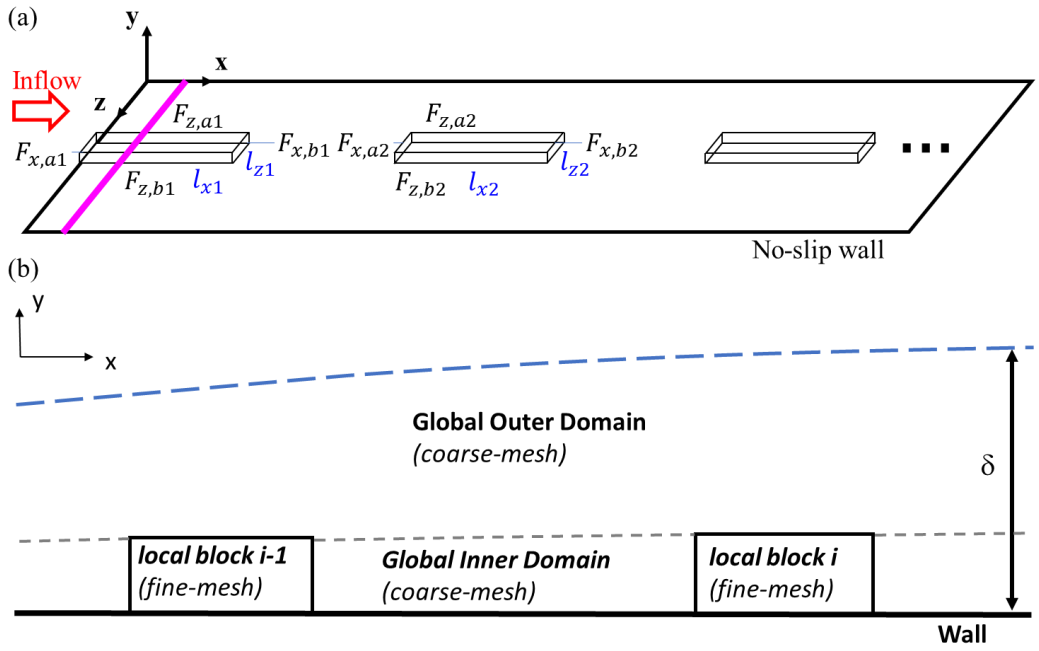


Figure 3.4. **Illustration of computing domains with near-wall embedded DNS blocks. (a) The overall view of the configuration (the solid magenta line indicates the trip); (b) a close-up $x-y$ plane view.**

The principal working of the two-scale methodology consists of two related aspects: a) generating the source term from the local fine mesh blocks, and b) propagating the source terms to the global inner coarse-mesh region (Figure 3.4b). Consider again the flow governing equations in a simple form for flow variable vector $\boldsymbol{u}$ as equation (3.3):

$$\frac{\partial \boldsymbol{u}}{\partial t} + R(\boldsymbol{u}) = 0$$

which in its original form will be directly solved numerically in the global outer domain and local inner blocks (Figure 3.4b). For the global under-resolved coarse-mesh inner domain in the near-wall region (Figure 3.4b), the upscaling is introduced leading to the augmented equation with extra source terms to drive the coarse-mesh solution toward the target solution equivalently subject to a fine-mesh locally.

Same as that in the channel flow, the upscaling is facilitated through space-time averaging. For a coarse-mesh cell embedded with n_f fine-mesh cells, the space-time averaged flow variable can be simply defined as the local volume-average of time-averaged variables of n_f fine-mesh cells in equation (3.11):

$$\widetilde{\overline{\boldsymbol{u}}}_f(\boldsymbol{x}) = \frac{1}{\Delta v_C} \sum_{i=1}^{n_f} [\overline{\boldsymbol{u}}_f(\boldsymbol{x}) \Delta v_f]_i.$$

where Δv_C is the volume of the coarse mesh cell: $\Delta v_C = \sum_{i=1}^{n_f} (\Delta v_f)_i$. The overbar '$-$' and '$\sim$' denote the time-averaged and the spatial-averaged values, respectively. The upscaled equation in the coarse mesh domain becomes equation (3.12):

$$\frac{\partial \boldsymbol{u}_C}{\partial t} + R(\boldsymbol{u}_C) = \boldsymbol{ST}_{st}(\boldsymbol{x})$$

Once the local sample source terms are generated, we need to effectively utilise the sample value for mapping in a spatially developing direction with inhomogeneity. He (2018) resorts to constructing and propagating the global spatial variations in the two wall-parallel directions through a Fourier spectral mapping for a periodic domain or a half of the Fourier spectrum for a non-periodic domain. In the present work, the Chebyshev spectral method is used for a clear non-periodic TBL

flow in the streamwise direction. The orthogonal group of Chebyshev polynomials are constructed as

$$T_n(x) = \cos[n \cdot arccos(x)], n = 1, 2, \ldots$$

(3.17)

The sampling points on the transformed interval [−1, 1] are based on the Chebyshev-Gauss-Lobatto points as

$$x_n = -\cos\left(n \cdot \frac{\pi}{N}\right), n = 0, 1, 2, \ldots, N.$$

(3.18)

The corresponding values at sampling points are $f_n(x_n), n = 0, 1, \ldots, N$. The interpolated function can be expressed as a linear combination of coefficients C_n and the basis functions $T_n(x)$ as

$$f^{approx}(x) = \sum_{n=0}^{N-1} C_n T_n(x).$$

(3.19)

Herein, the discrete cosine transform can be used to acquire the coefficients $\boldsymbol{C} = [C_1, C_2, \ldots, C_N]^T$ from the sampled function values $\boldsymbol{f} = [f_1, f_2, \ldots, f_N]^T$ as

$$\boldsymbol{C} = \boldsymbol{\Lambda f}$$

(3.20)

where the constructor matrix $\boldsymbol{\Lambda}$ is a linear system of $N + 1$ dimensions (Trefethen, 2000). The constructor matrix can be expressed as

$$\Lambda_{nm} = \begin{cases} \dfrac{1}{N}, m = 0 \\ \dfrac{2}{N} cos \dfrac{nm\pi}{N}, m = 1, \dots, N-1 \\ \dfrac{1}{N} \cos(n\pi), m = N \end{cases}$$

(3.21)

A flowchart showing the main parts of the present two-scale block spectral method during one time-marching step is given in Figure 3.5, for the method as implemented in the OpenFOAM for incompressible flows.

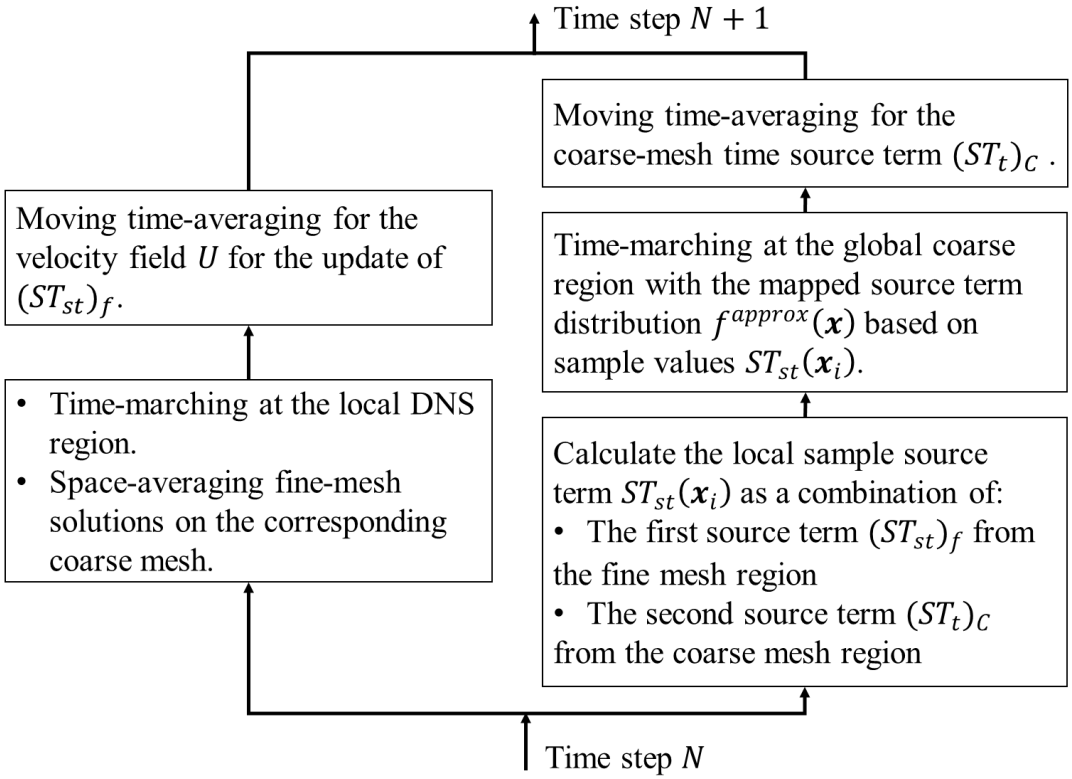


Figure 3.5. **Flowchart of the two-scale block-spectral solution process as implemented.**

4 INITIAL IMPLEMENTATIONS AND ASSESSMENTS FOR RANS

Having introduced in detail the two-scale framework and the block-spectral methodology, in this section, some preliminary RANS implementations in channel flows and turbulent boundary layer flows will be presented. The aim is to demonstrate how the spatial or temporal non-linear terms in the governing equations can be utilised in the two-scale formulation through ‘upscaling’, and besides, to investigate the validity and effectiveness of the two-scale method as an implementation of practical RANS calculations.

4.1 Channel Flow

Special demonstration cases in plane channel flows are chosen in this section. First of all, in section 4.1.1, no spatial non-linearity is involved with a clear manifestation of how the temporal non-linearity source terms can be used to reproduce the time-averaged solution results. In section 4.1.2, no temporal non-linearity is involved with the laminar case showing how the spatially averaged laminar solutions can be reproduced on a much coarser mesh under the source-term driving. Finally, in section 4.1.3, a RANS case is introduced as a practical implementation of the two-scale block-spectral method.

4.1.1 Temporal Non-linearity

In the previous chapter, we have introduced lumped governing equations in a simple form for flow variable vector $\boldsymbol{u}$ in equation (3.3):

$$\frac{\partial \boldsymbol{u}}{\partial t} + R(\boldsymbol{u}) = 0.$$

Recall that we will have equation (3.5) after time-averaging the flow equations:

$$\overline{R(\boldsymbol{u})} = 0.$$

Due to nonlinearity, $\overline{R(\boldsymbol{u})} \neq R(\overline{\boldsymbol{u}})$. The equations with the time-averaged flow variables can only be balanced with extra terms as in equation (3.6):

$$R(\overline{\boldsymbol{u}}) = \boldsymbol{ST}_t$$

served as the ‘direct mode’. Alternatively, as demonstrated, we can also view the upscaled equation in an ‘inverse mode’ to be further used in upscaling the fine-scale solutions to the coarse region:

$$\boldsymbol{ST}_t = R(\overline{\boldsymbol{u}})$$

(4.1)

As mentioned, the 'inverse mode' should be able to reproduce the time-averaged solution as a balancing source term added back to the governing equation, should the simulation be statistically converged to a time-mean flow field (Ning & He 2001). In other words, supposing a time-averaged target flow field is given, a non-linear source term can be generated accordingly to reproduce the exact same time-mean flow field. This procedure essentially works for the RANS closure purpose. For general concept proof purposes, a simple LES demonstration case is first introduced as follows to obtain the target solutions.

For validation purpose, a baseline LES case of the channel flow is first set up. We have a canonical turbulent channel flow at Reynolds number $Re_\tau \approx 400$ simulated using the open-source CFD solver OpenFOAM. The baseline unsteady incompressible flow equations in a channel flow domain $\Omega = [0, L_x] \times [0, 2\delta] \times [0, L_z]$ are

$$\nabla \cdot \boldsymbol{u} = 0$$

$$\frac{\partial \boldsymbol{u}}{\partial t} + (\boldsymbol{u} \cdot \nabla)\boldsymbol{u} + \frac{1}{\rho}\nabla p - \nu \nabla^2 \boldsymbol{u} = \boldsymbol{f}$$

(4.2)

where $\boldsymbol{u} = (u, v, w)^{-1}$. The only nonzero element of the baseline source term vector $\boldsymbol{f}$ is the streamwise pressure gradient, $f_x = dP/dx$. The corresponding boundary conditions for the domain are:

$$\begin{cases} \boldsymbol{u} = (0,0,0), at\ y = 0\ and\ y = 2\delta \\ \boldsymbol{u}\ and\ p\ periodic\ in\ x\ and\ z\ directions\ in\ \Omega \end{cases}$$

(4.3)

The size of the domain is taken to be $L_x = 2\pi\delta$, $L_y = 2\delta$ and $L_z = \pi\delta$ in the streamwise (x), wall-normal (y) and spanwise (z) directions, respectively, where δ is the half height of the channel.

The flow equations are discretised in a finite volume scheme, using the 2nd order central difference scheme for spatial discretisation and the implicit 2nd order time-marching method. A constant time-step is taken in keeping the maximum Courant numbers below 0.5. The PISO (Pressure-Implicit with Splitting of Operators) algorithm is used to solve the flow field. The message passing interface is used for transferring data between neighbouring blocks in parallel computing.

The fully developed channel flow is driven by a set mass flow. Given a bulk mean velocity $U_b = \frac{1}{2\delta}\int_0^{2\delta} \bar{u}(y)\, dy$ in the streamwise direction, the present simulations are carried out at bulk Reynolds numbers in line with those of the published DNS data (Moser, et al. 1999). The simulations are initialised with a laminar parabolic Poiseuille profile (de Villiers 2006) and run for a sufficiently long time to reach a statistically steady state with mean statistics to differ less than 1%. The turbulence statistics to be reported are obtained by ensemble-averaging the flow quantities spatially in the two homogeneous directions and in time over at least ten eddy turnover times δ/u_τ.

Uniform grids are implemented in streamwise and spanwise directions. In the wall-normal direction (y), grids are allocated with a geometric stretching ratio of

around 1.05. The mesh grid spacings Δx, Δy and Δz follow a general LES guidance: $\Delta x^+ \approx 15$, $\Delta z^+ \approx 10$, $\Delta y^+_{min} \approx 1$ and $\Delta y^+_{max} \approx 8$.

In the present calculations, no explicit sub-grid model is included, the solutions can thus be regarded as implicit LES where the sub-grid scales are dampened by numerical dissipations. Also, not a single wall function is involved.

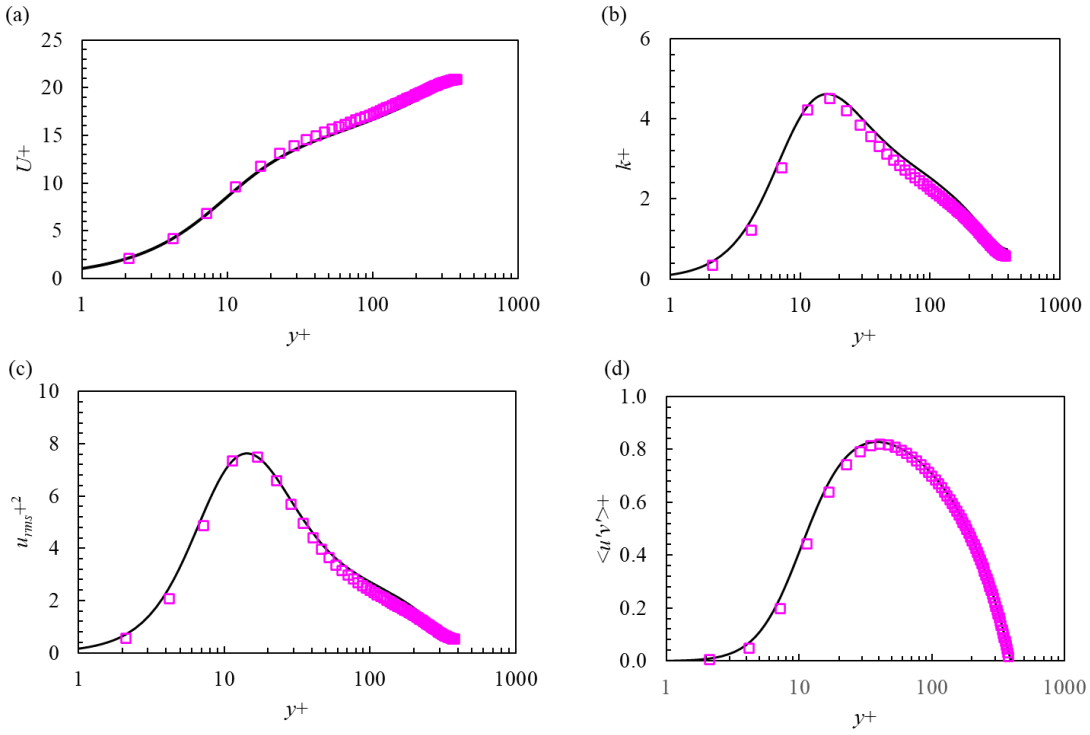


Figure 4.1. **The present LES solutions compared with the DNS database (Moser, et al. 1999) shown in black solid lines '—'. (a) Mean velocity profiles (b) kinetic energy profiles (c) Reynolds stress $u_{rms}^{+\,2}$ (c) Reynolds stress $< u'v' >^+$. Present results are shown in magenta open squares '□'.**

The simulation results as the time-mean statistics are shown in Figure 4.1. Overall, the mean velocity profile, the kinetic energy together with the Reynolds stress predictions are all in good agreement with the DNS results (Moser, et al.

1999). Again, the superscripts '+' here denote results in wall units. The ensemble averaging is denoted by '$<\cdot>$' and the subscript 'rms' denotes the root-mean-squared values. Moin & Jimenez (1997) and Jimenez & Moser (2000) stress that the near-wall mesh resolution of a wall-resolved LES should be approaching that of a DNS, given that Kolmogorov micro-scales gather in the near wall. Further near-wall refinement should be needed for more accurate solutions. For the present validation purpose in this section, the LES mesh resolution should be sufficient.

Having the statistically converged LES solutions on hand, we are now aiming to reproduce the time-mean solutions on the exact same mesh grids:

$$\frac{\partial \boldsymbol{u}}{\partial \tau} + R(\boldsymbol{u}) = \boldsymbol{ST}_t \tag{4.4}$$

where τ is the pseudo marching time-step, with the time-averaged solution $\overline{\boldsymbol{u}}$ is intended at the converged state. The source terms $\boldsymbol{ST}_t$ is obtained as the residual as $R(\overline{\boldsymbol{u}})$, where $\overline{\boldsymbol{u}}$ is the target time-averaged solution of the baseline LES case. To reproduce the solutions, both the meshing and discretisation schemes are kept the same as the baseline case with the target solutions.

In fact, the reproduction of simulation results using existing databases, usually via machine learning tools, is a branch of study drawing growing interest. It is recently discovered that the explicit data-driven Reynolds stress closure of RANS equations can sometimes be 'ill-conditioned' (e.g., Wu, et al. 2019) due to the lack of numerical stability.

Ning and He (2001) suggest that $\boldsymbol{ST}_t$ provides considerable damping to enable a steady-state convergence. It is later discovered that the damping could be insufficient given the specific numerical schemes and meshes used (He 2018), in which case the solution could be diverging. For remedy, a simple artificial damping term is added to the governing equation and is surprisingly effective as shown in He (2018). Briefly, the damping term is in the form of physical viscous diffusion terms using an artificial viscosity based on mixing-length:

$$\nu_d = [\min(\kappa, L_d)]^2 |\bar{\boldsymbol{\omega}}| \tag{4.5}$$

where $\kappa = 0.41$ is the von Karman constant; y is the wall distance; L_d is the empirical cut-off mixing length; $|\bar{\boldsymbol{\omega}}|$ is the magnitude of the time-averaged vorticity. With the damping terms added, equation (4.4) is modified as

$$\frac{\partial \boldsymbol{u}}{\partial \tau} + R(\boldsymbol{u}) = \boldsymbol{ST}_t + D(\boldsymbol{u}) - D(\bar{\boldsymbol{u}}) \tag{4.6}$$

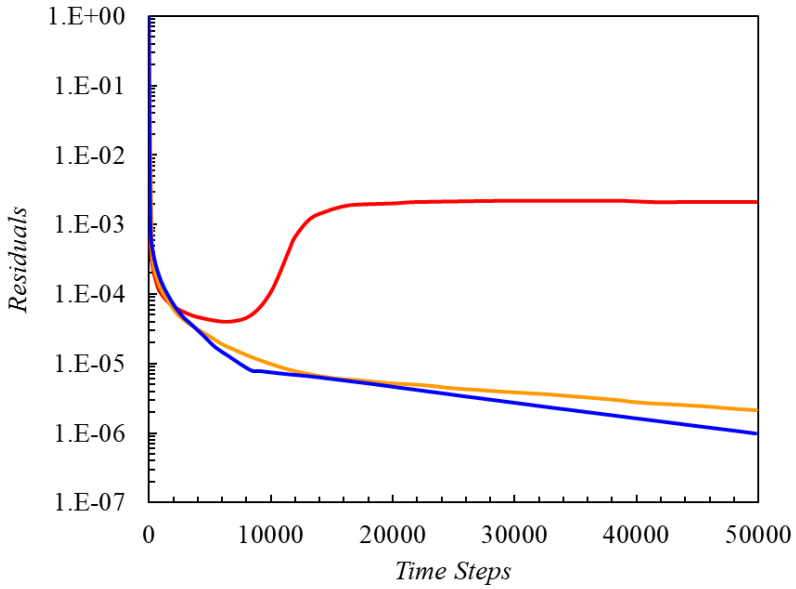


Figure 4.2. **Convergence history as the normalised residual versus marching time steps of cases using different damping parameters. Red solid line '—': L_d = 0; Yellow solid line '—': $L_d = 0.1\delta$; Blue solid line '—': $L_d = 0.2\delta$.**

Note that should equation (4.6) be converged, the difference between the two damping terms $D(\boldsymbol{u})$ and $D(\bar{\boldsymbol{u}})$ is negligibly small, being balanced out with $\boldsymbol{u}$ approaching $\bar{\boldsymbol{u}}$. In this case, the uncertainty brought by the empirically specified mixing-length L_d should be trivial. The convergence history of numerical residual plotting regarding the present case is shown in Figure 4.2. Three cases are compared here, including:

1) The solution without added damping term (L_d = 0),

2) The solution with the damping term where $L_d = 0.1\delta$, and

3) The solution with the damping term where $L_d = 0.2\delta$.

It is observed in Figure 4.2 that the addition of damping terms gives rise to a significant stabilising effect and enhances convergence. The influence of the

damping configurations on the final results is shown in Figure 4.3. The results of the two cases with different L_d both show little difference compared with original LES solutions.

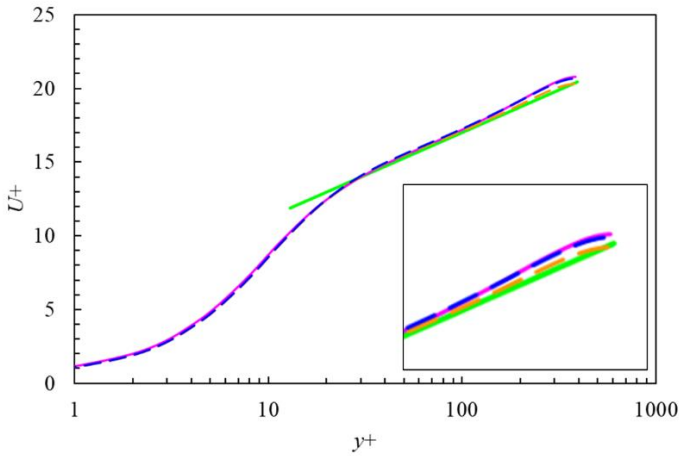


Figure 4.3. **Mean velocity profiles as solutions using different damping parameters. Results are compared with the baseline LES solutions shown in the solid magenta line '—'. Yellow dashed line '— —': $L_d = 0.1\delta$; Blue solid line '— —': $L_d = 0.2\delta$. The green solid line '—' marks $U^+ = 2.5\ln(y^+) + 5.5$. The magnified view is also included indicating the difference between the three cases at the wake region.**

4.1.2 Spatial Non-linearity

In this section, the demonstration case is aiming to show the reproduction of fine-scale solutions on the coarse mesh, using the spatial non-linear source terms generated due to purely the resolution difference between the fine and coarse meshes. Thus, the steady-state laminar case is chosen to be studied without any time invariants involved. The Navier-Stokes equations effectively depict the laminar Poiseuille flow in the 2-D channel in this case.

The spatially averaged fine-mesh solutions should not satisfy the governing equations discretised as per the coarse mesh, while there should be inaccurate solutions satisfying the converged coarse-mesh discretised equations with discretisation errors. We again obtain the spatial source terms as the 'inverse mode':

$$\boldsymbol{ST}_s = R(\widetilde{\boldsymbol{u}}_f) \tag{4.7}$$

In this case, a known fine-scale laminar solution $\boldsymbol{u}_f$ is taken as the input and the source terms as the output. The source terms should drive the coarse-mesh domain to converge, with $\boldsymbol{u}_C = \widetilde{\boldsymbol{u}}_f$ as intended in the present case of the laminar flow field.

Note that in this certain laminar case, for a coarse mesh cell with m fine mesh cells, the corresponding local spatially averaged coarse-mesh variable as demonstrated in equation (3.9) is:

$$\widetilde{\boldsymbol{u}}_f(\boldsymbol{x}) = \frac{1}{\Delta v_C}\sum_{i=1}^{m}[\boldsymbol{u}_f(\boldsymbol{x})\Delta v_f]_i$$

The upscaled equation in this case simply reduces to

$$\frac{\partial \boldsymbol{u}_C}{\partial t} + R(\boldsymbol{u}_C) = \boldsymbol{ST}_s(\boldsymbol{x}) \tag{4.8}$$

Consider a 2-D laminar channel flow requesting a certain level of spatial resolution. We deliberately introduce an overly coarsened mesh of 10 and 5 mesh cell centres evenly distributed in the streamwise (x) and the wall-normal (y) directions respectively. We thereafter refine the mesh in an embedded manner with

the resolution of 50 and 50 mesh cell centres evenly distributed in the x and y directions, respectively. Each coarse-mesh cell, therefore, corresponds to 50 (5×10) fine-mesh cells.

The corresponding results are shown in Figure 4.4. First of all, for validation purposes, the numerical solutions on the fine mesh matching up with the analytical solution of 2-D Poiseuille channel flow indicates that the fine-mesh resolution is adequate. Meanwhile, the coarse-mesh solutions show non-negligible differences compared with the analytical solutions. The fine-mesh solutions are thereafter spatially averaged according to equation (3.9) and are mapped to the coarse mesh for the source term generation as equation (4.7). With the source term added, the governing equation eventually converges to the spatially averaged fine-mesh solution as reproduced on the coarse mesh.

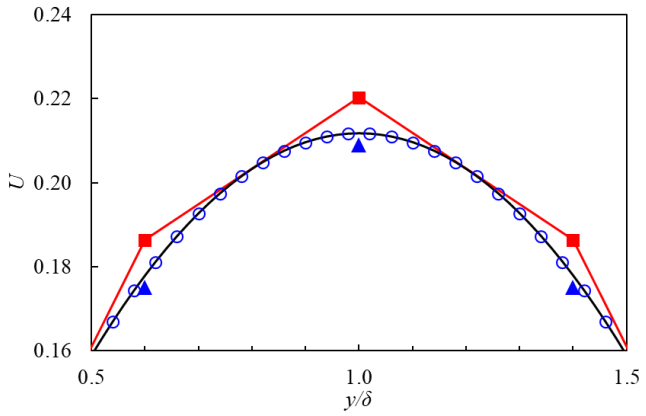


Figure 4.4. **Velocity profiles in the laminar channel flow. The black solid line '—': analytical solutions; open blue circles '○': fine-mesh numerical solutions; solid red squares connected by solid red lines '—■—': coarse-mesh numerical solutions; solid blue triangles '▲': numerical solutions using the source-term approach.**

4.1.3 RANS Solution

In this section, the source-term method is implemented in a 3-D RANS case in the channel flow for demonstration. Recall that we have the 'direct mode' equation (3.6) as:

$$R(\overline{\boldsymbol{u}}) = \boldsymbol{ST}_t$$

From the aspect of general CFD applications taking the RANS approach, it aims at solving the time-mean flow field with the Reynolds stresses modelled by a set of extra supplementary equations (e.g., Hallback et al. 1989; Launder & Spalding 1974; Wilcox 2006) or only one in the one-equation models (Spalart & Allmaras 1994). The 'direct mode' can be simply seen as the governing equation of a RANS approach with the $\boldsymbol{ST}_t$ calculated via the 'Reynolds stress term' modelling.

Here, we take the source-term approach to calculate the $\boldsymbol{ST}_t$ using the 'inverse mode' by upscaling the fine-mesh solutions:

$$(\boldsymbol{ST}_t)_f = R(\widetilde{\overline{\boldsymbol{u}}}_f) \tag{4.9}$$

The intended coarse mesh solution should be converged as equation (3.16):

$$R(\overline{\boldsymbol{u}}_C) = R(\widetilde{\overline{\boldsymbol{u}}}_f)$$

Note that the supplementary equation is also lumped in $R(\widetilde{\overline{\boldsymbol{u}}}_f)$. For instance, in the Spalart-Allmaras (S-A) one-equation model adopted in the present calculations (Spalart & Allmaras 1994), $\boldsymbol{u}$ denotes the variable vectors, including the turbulent eddy viscosity ν_t as one of the four scalar variables (besides the velocity scalars in the three directions as u_x, u_y and u_z).

Note that a certain level of mesh resolution is requested for accurate RANS solutions. Usually, mesh points are clustered towards the wall with increasingly finer mesh in the wall-normal direction. In the present demonstration case, we remove the near-wall fine mesh and replaced it with the coarse mesh in the global domain, while the fine mesh is retained in certain regions in an embedded manner. The entire simulation domain is thus partitioned into a 'dual meshing' system introduced in section 3.2 (Figure 3.1).

The baseline 3-D RANS channel flow case is first set up with the targeted Reynolds number $Re_\tau \approx 400$ simulated using the open-source CFD solver OpenFOAM. The domain size is again taken to be $L_x = 2\pi\delta$, $L_y = 2\delta$ and $L_z = \pi\delta$ in the streamwise (x), wall-normal (y) and spanwise (z) directions, respectively, where δ is the half height of the channel. The no-slip boundary condition is applied to the wall. Both the streamwise and spanwise patches are implemented with periodic boundary conditions. The SIMPLE (Semi-Implicit Method for Pressure Linked Equations) solver is used to calculate the time-mean flow field.

Uniform grids are implemented in streamwise and spanwise directions. In the wall-normal direction (y), grids are allocated with a geometric stretching ratio of around 1.2. The mesh grid spacings Δx, Δy and Δz follow a general RANS guidance: $\Delta x^+ \approx 80$, $\Delta z^+ \approx 40$, $\Delta y^+_{min} \approx 0.6$ and $\Delta y^+_{max} \approx 50$.

For the two-scale approach, the methodology follows that introduced in chapter 3 with the RANS cases set up here for concept proof purposes and as simple demonstration cases of RANS implementation with the space-time source term $\boldsymbol{ST}_{st}$ reduced to $\boldsymbol{ST}_t$ in equation (4.9). The fine local mesh near wall is kept the same

resolution as the baseline RANS case and is embedded as a near-wall block as in Figure 3.1 ('Domain 2'), denoted as 'L'. The block size is chosen to have streamwise length $l_x^+ = 1600$ and spanwise width $l_z^+ = 800$, which are tested to be insensitive on the final solutions as in the RANS cases. Three test cases (namely '*Case 1*', '*Case 2*' and '*Case 3*') with three different block heights $l_y^+ = 20$, 40 and 60 are simulated. The coarse global mesh near wall ('Domain 3' in Figure 3.1), denoted as 'G', keeps the same streamwise and spanwise resolution as the baseline RANS, whereas the wall-normal resolution is replaced by one mesh cell point under $y^+ = l_y^+$. The outer coarse mesh ('Domain 1' in Figure 3.1) is kept the same as the baseline RANS case. The simulation parameters are gathered to be shown in Table 4.1, with $\Delta_{y,w}^+$ denoting the mesh resolution at wall.

Table 4.1 RANS simulation parameters within global ($\boldsymbol{G}$) and local-embedded ($\boldsymbol{L}$) domains.

$\boldsymbol{Re_\tau}$	Domain	$\boldsymbol{G}$: $\boldsymbol{L_x, L_z}$ $\boldsymbol{L}$: $\boldsymbol{l_x^+, l_z^+}$	$\boldsymbol{\Delta_{y,w}^+}$	$\boldsymbol{\Delta_x^+, \Delta_z^+}$
400	G	$2\pi\delta, \pi\delta$	*Case 1*: 20 *Case 2*: 40 *Case 3*: 60	80, 40
	L	1600, 800	0.6	

A flowchart showing the main elements of the present two-scale method as implemented for RANS simulations in the OpenFOAM for incompressible flow is demonstrated in Figure 4.5.

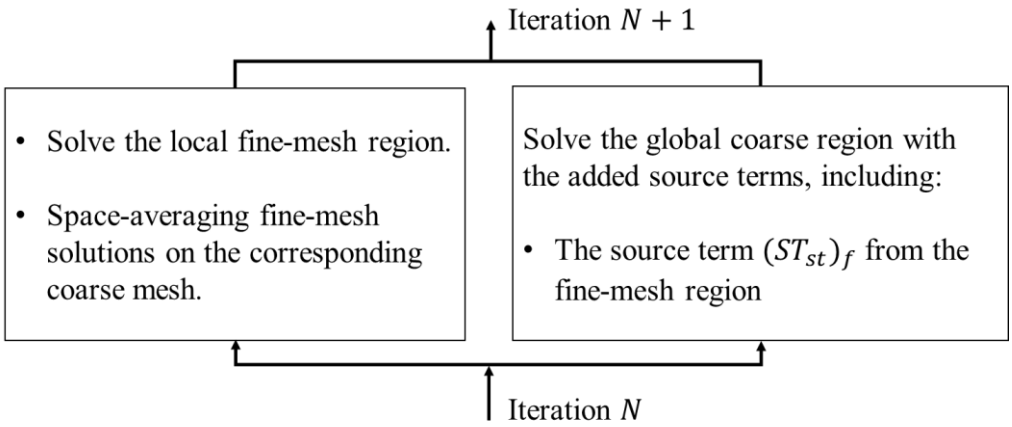


Figure 4.5. Flowchart of the two-scale block-spectral solution process as implemented in RANS channel flows.

The results as the mean velocity profiles in the global coarse region are presented in Figure 4.6. The cases computed by using the present two-scale method are labelled as '*Two-scale'*. The '*Two-scale'* solutions consistently match up with the DNS solutions. The wall shear stress in this RANS case is determined using the solutions at the fine-mesh region, calculated using the mean velocity at the first mesh cell at the no-slip wall.

The predictions on the turbulent eddy viscosity ν_t are shown in Figure 4.7. Again, the cases using the two-scale method are labelled as '*Two-scale*'. Also included are the cases computed without the source-term coupling in the global coarse inner region, which are effectively single-scale direct solutions, and thus are labelled as '*One-scale*'.

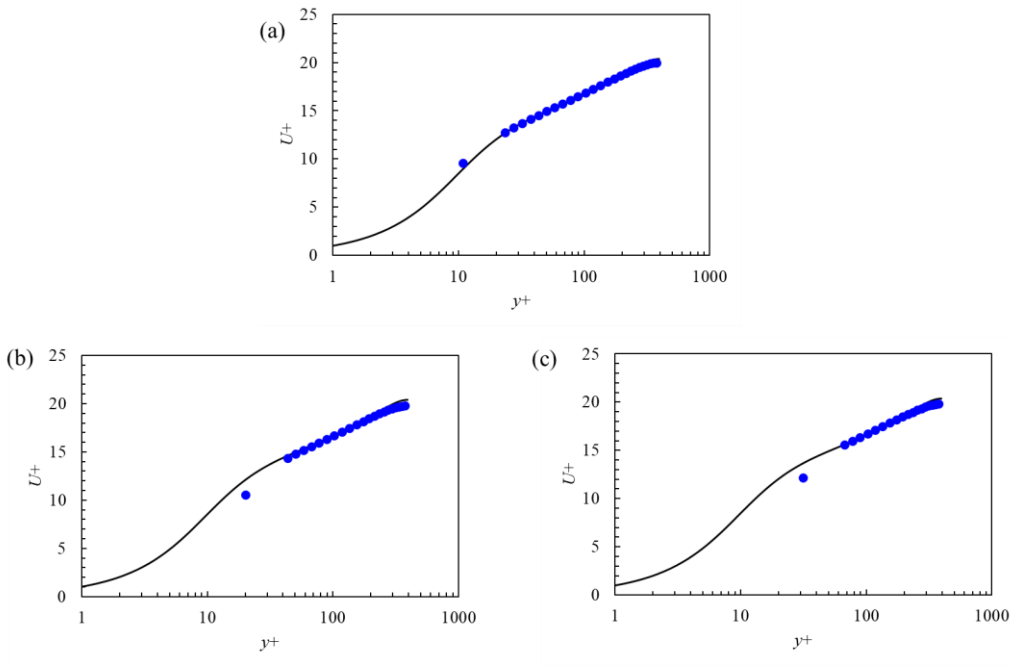


Figure 4.6. **Mean velocity profiles of RANS compared with DNS solutions (Moser, et al. 1999) shown in black solid lines '—'. '*Two-scale*' solutions are shown in solid blue circles '●'. (a) Results of '*Case 1*'; (b) Results of '*Case2*'; (c) Results of '*Case 3*'.**

In Figure 4.7(a), when the first coarse-mesh cell centre in the wall-normal direction lies in the viscous sublayer in this channel flow case, the global coarse mesh itself is capable of producing the accurate turbulent eddy viscosity as the *'One-scale'* solutions. In the cases where the mesh resolution at the wall becomes even coarser, the *'One-scale'* results deteriorate, while the '*Two-scale'* solutions consistently match up with the DNS solutions. Notice that the flow variables at the first mesh cell are accurately reproduced as the spatially weighted averaged fine-mesh solutions on the coarse mesh via the source-term approach.

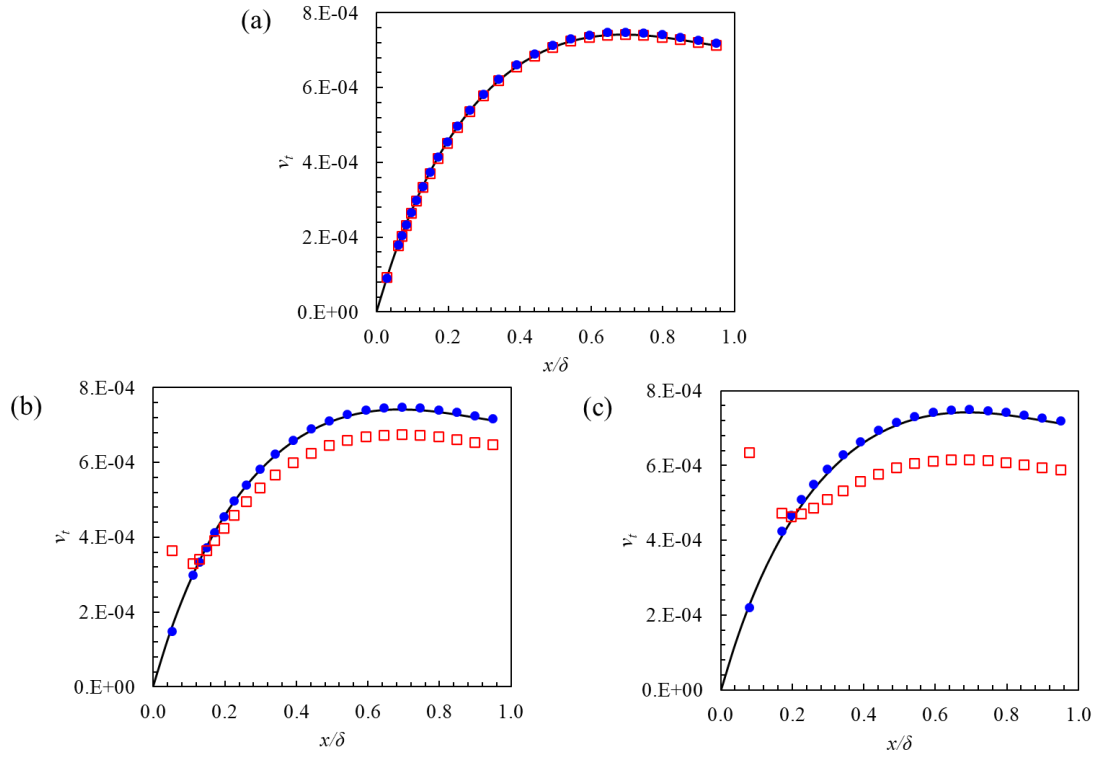


Figure 4.7. **Turbulent eddy viscosity ν_t modelled from the S-A model compared with those solved by the fine mesh shown in black solid lines '—'. '*Two-scale*' solutions are shown in solid blue circles '●'. '*One-scale*' solutions are shown in open red squares '□'. (a) Results of '*Case 1*'; (b) Results of '*Case2*'; (c) Results of '*Case 3*'.**

4.2 Turbulent Boundary Layer

At the end of the previous section, it demonstrates the source-term method being implemented in the plane channel flows as an application in RANS. Given the homogeneity in both of the wall-parallel directions, the propagation of the source term as expected is rather straightforward. Uniform source terms generated from the

embedded fine-mesh region are simply copied and added to the entire near-wall coarse-mesh region.

In this section, the global homogeneous streamwise direction no longer holds as we are intending to investigate the 2-D turbulent boundary layer flows as another implementation in RANS. Hence, the interpolation of source terms should be involved during the propagation process. The local source terms could be generated as a representative of the target space-time-averaged local fine-mesh solutions, which are amendable to the Chebyshev spectral propagation to deal with the global streamwise inhomogeneity, as shown in section 3.4. Notice that the initiation of TBL will be studied in chapter 6, and here in this section, the focus will be placed on the source term propagation and the time-mean flow field reproduction. The laminar-to-turbulent transition is decided to be placed less attention in the RANS cases and no tripping techniques should be involved.

First of all, the baseline RANS cases are set up as a simple 2-D boundary layer flow on a smooth flat plate. All configurations are set up identical to Rumsey (2014). The one-equation S-A turbulence model is applied. The boundary layer is developing in the streamwise x direction. The y direction is normal to the bottom no-slip wall. The pressure gradient in the x and y direction should be ideally zero. The velocity inlet and the zero-pressure-value outlet are chosen as the boundary conditions. The upper boundary is set as a slip wall to mimic an infinite wall-normal height of the domain. The 2-D simulation domain is in the size of $\Omega = [0, L_x] \times [0, L_y]$. The free stream velocity is at 0.2 Mach, giving the local Reynolds number $Re_x = 5 \times 10^6$ at the outlet, where $x = L_x$. The domain height L_y is sufficiently large as $L_y = 0.5L_x$ to hold at least 10 local boundary layer thicknesses. The

SIMPLE (Semi-Implicit Method for Pressure Linked Equations) solver is used to calculate the time-mean flow field.

Two baseline cases are simulated, namely '*baseline-Coarse*' and '*baseline-Fine*'. For the coarse-mesh simulation '*baseline-Coarse*', in the streamwise direction, 100 mesh cell points are uniformly distributed. In the wall-normal direction (y), the mesh is clustered to the wall with the first grid spacing at wall $\Delta y^+_{w,C} = 10$. Grids are allocated with a geometric stretching ratio of around 1.05. The first grid spacing at wall is further refined in the y direction for the fine-mesh simulation '*baseline-Fine*'. For each mesh cell adjacent to the wall in '*baseline-Coarse*', it is evenly divided into ten layers as $\Delta y^+_{w,f} = 1$ for '*baseline-Fine*'. Note that the wall units in this section denoted by '$+$' are all calculated based on the local shear velocity u_τ predicted by '*baseline-Fine*'.

The solutions at $Re_x = 5 \times 10^6$ are compared with the data published by Langley Research Center, NASA (Rumsey 2014) as shown in Figure 4.8. It can be observed that the '*baseline-Fine*' solutions show little difference compared to the published reference data.

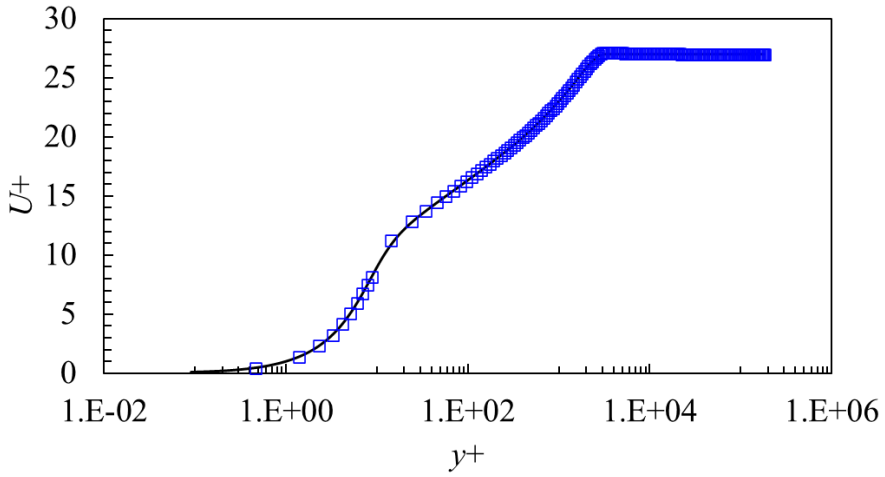


Figure 4.8. **Baseline validation against NASA data (Rumsey 2014) shown in the solid black line '—'. The present RANS solutions are: '*baseline-Fine*' shown in open blue squares '□'.**

We embed the local fine-mesh blocks (Figure 3.4b) with mesh resolution the same as '*baseline-Fine*' to the global coarse mesh. The two-scale methodology adopted follows that introduced in section 3.4, apart from that the space-time source terms $\boldsymbol{ST}_{st}$ are reduced to $\boldsymbol{ST}_{t}$ in equation (4.9) for the present RANS case, same as that in section 4.1.3. The embedded fine mesh blocks are evenly distributed on $x = [0, L_x]$. For example, if only two blocks are embedded, the locations of them are at $x = 0$ and L_x respectively. If four blocks are embedded, the corresponding locations are $x \in \{0, L_x/3, 2L_x/3, L_x\}$. The block size is chosen to have streamwise length covering 5 coarse mesh cells and the wall-normal height l_y essentially being $l_y^+ = \Delta y_{w,C}^+ = 10$.

A flowchart as implemented for RANS simulations in the OpenFOAM for the incompressible boundary layer flow is demonstrated in Figure 4.9.

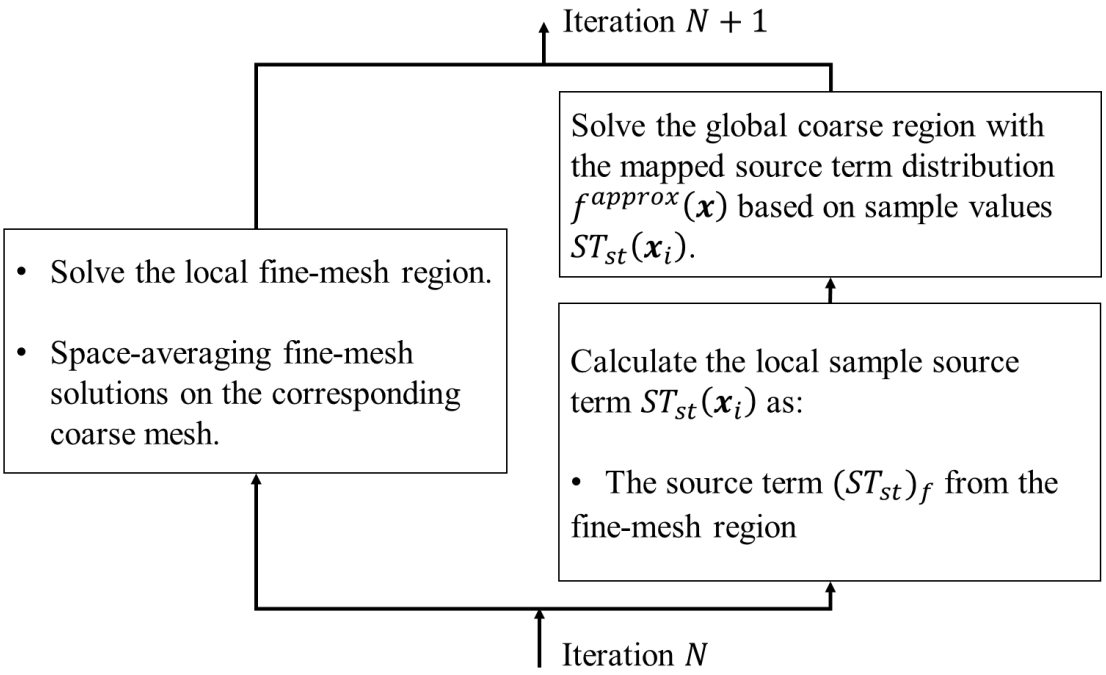


Figure 4.9. **Flowchart of the two-scale block-spectral solution process as implemented in RANS boundary layer flows.**

The solutions in the global coarse region of the calculation using the present two-scale block-spectral method with only two fine-mesh blocks embedded are shown in Figure 4.10, labelled as '*Two-scale*', which shows little difference from the '*baseline-Fine*' results. Again, the wall shear stress is determined using the solutions at the fine-mesh region, calculated based on the mean velocity at the first mesh cell at the wall.

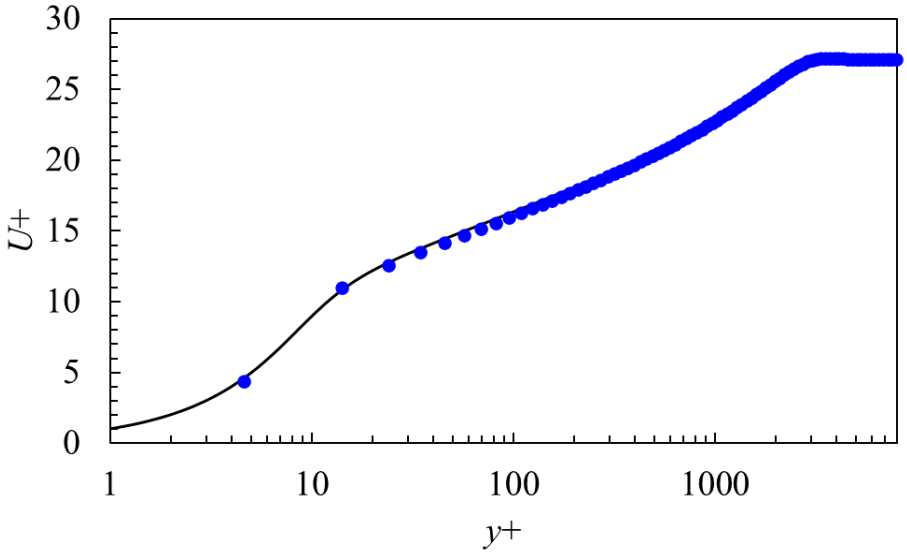


Figure 4.10. **Velocity profiles compared with the '*baseline-Fine*' shown in the black solid line '—'. '*Two-scale*' solutions with 2 fine-mesh blocks embedded are shown in solid blue circles '●'. The results are at $Re_x = 5 \times 10^6$.**

Other than the streamwise location $x = L_x$, velocity profiles at $x = 0.4L_x$ ($Re_x = 2 \times 10^6$) are shown in Figure **4.11**. Solutions of '*Two-scale*' calculations using 2 embedded fine-mesh blocks and 4 blocks are compared as can be observed to have trivial differences, both matching up quite well with the '*baseline-Fine*'.

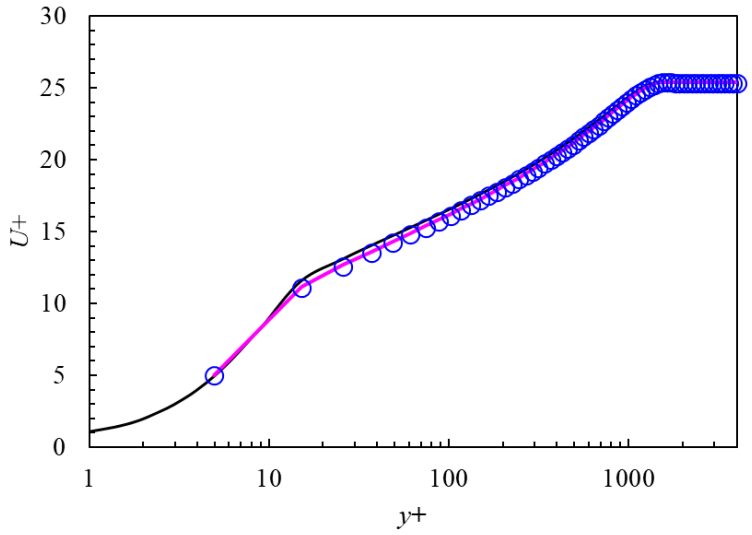


Figure 4.11. **Velocity profiles compared with the '*baseline-Fine*' shown in the black solid line '—'. 'Two-scale' solutions with 2 fine-mesh blocks embedded are shown in open blue circles '○'. 'Two-scale' solutions with 4 fine-mesh blocks embedded are shown in the magenta solid line '—'. The results are at $Re_x = 2 \times 10^6$.**

4.3 Summary

Demonstration cases are presented in this chapter for validation purposes on the manipulation of source terms resulting from temporal and spatial non-linearity. Two-scale RANS solutions in the turbulent channel and boundary layer flows are also demonstrated as the RANS implementations.

Note that, until this stage, the significant saving on computational costs has not yet been analysed, given that the RANS baseline cases in this chapter are requesting manageable computing resources. Nor is any turbulence physics

aforementioned in chapter 2 involved, here in the RANS cases. This chapter instead focuses on the manipulation of the source terms and elaborates the two-scale formulation (‘upscaling’) in specific cases. The following chapters will implement the two-scale method in scale-resolving (LES/DNS) cases.

5 TWO-SCALE SOLUTIONS FOR TURBULENT CHANNEL FLOWS

We have introduced in chapter 3 the two-scale methodology to couple a locally embedded near-wall fine-mesh DNS block with a global coarser mesh domain. The influence of the large-scale structures on the local fine-mesh block is captured by a scale-dependent coarse-fine domain interface treatment. The coarse-mesh resolved disturbances are directly exchanged across the interface, while only are the fine-mesh resolved fluctuations around the coarse-mesh resolved variables subject to periodic conditions in the streamwise and spanwise directions respectively. The global near-wall coarse-mesh region outside the local fine-mesh block is

governed by the augmented flow governing equations with forcing source terms generated by upscaling the space-time averaged fine-mesh solution. The validity and effectiveness of the method are examined in this chapter for canonical incompressible channel flows at several Reynolds numbers. The potential computational gain is first measured in terms of the mesh-count scaling with the Reynolds number.

5.1 Mesh-count Scaling with Reynolds Number

Given the focus on the near-wall region requiring the highest mesh resolution and the primary intent to facilitate localised fine mesh blocks, we shall first examine the overall cost implication in terms of the mesh-count scaling with Reynolds number. In this section, the mesh-count estimation will be carried out based on a canonical plane channel flow. As shown in Figure 3.1, a local near-wall fine-mesh block is embedded in a global coarse-mesh domain. The dimensions of the local embedded block are given by the streamwise length l_x, the corresponding spanwise width l_z and the wall normal height l_y, in the x, z, and y directions respectively. In the following, we will first discuss the choice of the embedded fine-mesh block size, and then examine the mesh count-Reynolds number scaling in the context of two-scale DNS and LES solutions respectively.

5.1.1 Sizing of Fine-mesh Block

The selection of the near-wall fine-mesh block size is based on examining the DNS data for an incompressible channel flow by Lee & Moser (2015) with a range of friction Reynolds numbers up to $Re_\tau = 5200$, where $Re_\tau = u_\tau \delta / \nu$ is

based on the wall friction velocity u_τ, the boundary layer thickness or the half channel height δ and the kinematic viscosity ν. This is the DNS data set with the highest Reynolds number accessible in the public domain to the authors' knowledge. The energy spectra are generated as shown in Figure 5.1 by accessing and processing the DNS database (https://turbulence.oden.utexas.edu/). The energy spectra present a clear picture of the two distinctive parts of interest: the 'universal' first energy peak near wall and the departing second peak in outer flow with increasing Reynolds numbers.

The 'universality' of the first peak manifests in terms of the core location at approximately $y^+ \sim 13.5$ independent of Reynolds number, where the superscript '$+$' indicates the normalisation by u_τ and ν referred to as the viscous wall unit. Due to the dominance of small-scale activities in this inner near-wall region, the energy spectra of the first peak can be covered by constant cut-off wavelengths independent of Reynolds numbers. Based on the desired attribute for the embedded block to capture and resolve the 'universal' turbulence behaviour associated with the first peak, we would thus take the block sizes to be constant in wall units in the streamwise and spanwise directions respectively, $l_x^+ \approx 3500$ and $l_z^+ \approx 350$. The corresponding physical lengths in terms of the overall domain size (δ) will be reduced with an increase in Reynolds number. The choice of the fine-mesh block sizes in the x and z directions to be constant in wall units is in line with those adopted for a near-wall DNS patch by Carney, et al. (2020). The much longer streamwise domain size reflects the near-wall elongated streaky structures in the streamwise direction, consistent with common observations.

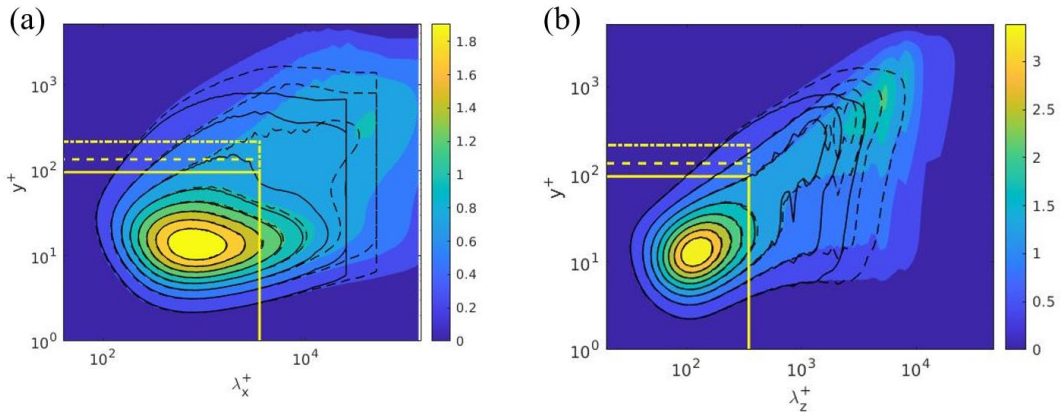


Figure 5.1. **One-dimensional pre-multiplied energy spectra reproduced from DNS data (Lee & Moser 2015) with respect to (a) streamwise and (b) spanwise wavelengths at Re_τ ≈1000 (solid lines '—'), 2000 (dash lines '— —') and 5200 (shaded contours). The yellow boxes mark the fine-mesh block sizes at Re_τ ≈1000 (solid lines '—'), 2000 (dash lines '— —') and 5200 (dash-dot lines '— · —') respectively.**

In the wall-normal direction, the starting location of the log-law region correlates directly to the Reynolds number: $y_s = C\delta^{+0.5}$, where δ is the boundary layer thickness or the channel half-height. In the present work, the coefficient C is taken after Marusic, et al. (2013), thus the wall-normal height of the fine-mesh block correlates with the Reynolds number as

$$l_y^+ = 3\sqrt{Re_\tau} \tag{5.1}$$

The choice of the embedded block size as described above should suffice in serving the present requirements for the near-wall region: to both resolve the 'universal' part of the near-wall turbulence and to capture the 'foot-printing' effects

of large coherent structures of the outer flow if appropriate interface conditions between the local fine-mesh block and the global coarse-mesh region can be established, as have been introduced in section 3.2.

5.1.2 Scaling mesh count with Reynolds number

For wall-bounded flows, a two-scale consideration leads to different mesh resolution requirements for the near-wall inner part and the outer flow region. We will now examine both DNS and wall-resolved LES. The DNS is considered first because the validations for the concept proof of the present two-scale method are conducted by comparing the present wall-embedded DNS with the well-established full DNS. Then, the LES is considered the primary motivation to develop an efficient alternative to the full wall-resolved LES for practical applications.

First, consider a near-wall region to compare LES with DNS. The local Kolmogorov micro-scales are naturally smaller than those usually set by typically modelled sub-grid scales in LES. The mesh resolution of a wall-resolved LES would approach that of a DNS in the near-wall region (Moin & Jimenez 1997; Jimenez & Moser 2000). As such, the mesh resolution required for the near-wall fine-mesh block can be taken to be the same for both DNS and LES in the present work.

For the outer flow region, large-scale flow structures can be captured by a coarser mesh. Given the importance of the history effect for any coherent structures, the mesh needs to cover a global domain of the whole channel. In addition, the mesh resolution required for resolving large turbulence structures should also be much less sensitive to the sub-grid models as well as to numerical dissipations. Hence, a mesh of LES for the bulk flow region can be much coarser than that of a DNS counterpart.

It then follows that the main difference in the mesh scaling between a wall-embedded DNS (denoted as 'WeDNS') and a wall-embedded LES (denoted as 'WeLES') will result from those for the global outer flow region.

i. Mesh scaling for Wall embedded DNS (WeDNS)

WeDNS scaling is introduced to keep grid spacings constant in wall units for both the outer global domain and inner near-wall embedded block at different Reynolds numbers, for consistency when compared with well-established DNS results. Following the procedure adopted by Jimenez (2003), we estimate the mesh count for a near-wall DNS block with its wall normal height bound by y_s marking the start of the log-law region:

$$NDNS_{fine\ inner} = NDNS_{embed\ block} \sim N_x N_z \int_0^{y_s^+} \frac{dy^+}{\Delta_y^+} \sim N_x N_z \left(\frac{y_s^+}{\Delta_y^+}\right) \sim {\delta^+}^{0.5} \tag{5.2}$$

where N_x and N_z are the mesh count of the fine mesh block in the x and z directions respectively and should be Reynolds-number-independent, given that the constant cut-off wavelengths in wall units l_x^+ and l_z^+ can be applied as discussed. Besides, in the wall-normal y direction, we have $y_s^+ = l_y^+ \sim O({\delta^+}^{0.5})$ given by equation (5.1) and $\Delta_y^+ \sim O(1)$.

For the outer region further away from the wall, the smallest scales to be resolved by DNS are of the order of the larger Kolmogorov scales correlated with the wall distance, $\Delta^+ \sim (y^+)^{0.25}$ (Tennekes & Lumley, 1972; Lee & Moser, 2019):

$$NDNS_{coarse\ outer} \sim \int_{y_s^+}^{\delta^+} (\delta^+/\Delta^+)^2 dy^+/\Delta^+ \sim {\delta^+}^2 \int_{y_s^+}^{\delta^+} {y^+}^{-3/4} dy^+ \sim {\delta^+}^{2.25}$$

(5.3)

The final part to be considered in the present two-scale strategy is the global near-wall region covered by a coarse mesh, apart from that of the fine mesh block ('Domain 3' as indicated in Figure 3.1b). It is assumed that the resolution of this near-wall coarse mesh is comparable to that of the outer coarse mesh at its low bound interfacing with the fine-mesh block. Thus, a largely constant mesh spacing in this region should be $\Delta^+ \sim (y_s^+)^{0.25}$. With the interface position y_s fixed by equation (5.1), we then have:

$$NDNS_{coarse\ inner} \sim {\delta^+}^2/(\Delta^+)^3 \cdot \int_0^{y_s^+} dy^+ \sim {\delta^+}^{2.125}$$

(5.4)

The overall mesh count of WeDNS is the sum of all three regions, equations (5.2), (5.3) and (5.4). The scaling with the Reynolds number is dictated by the highest power index. Thus, the overall mesh count scaling with Reynolds number for the wall-embedded DNS becomes:

$$N_{WeDNS} \sim {Re_\tau}^{2.25}$$

(5.5)

In contrast, following the same procedure, one should have a Reynolds number scaling of the mesh count for a full DNS as (Jimenez, 2003): $N_{DNS} \sim {Re_\tau}^3$.

ii. Mesh scaling for Wall embedded LES (WeLES)

As discussed, the mesh resolution for the near-wall fine-mesh block for WeLES should be identical to that for WeDNS. The mesh count for the near-wall embedded fine-mesh block will thus be:

$$NLES_{fine\ inner} = NDNS_{embed\ block} \sim {\delta^+}^{0.5} \tag{5.6}$$

For the LES outer region, the resolution is no longer set by the Kolmogorov scales as they are supposed to be filtered out and modelled while resolving the large energy-containing scales. Similarly, the outer region starts from the low bound of the log-region y_s and the integral length scales are proportional to wall distance (Townsend 1976; Jiménez 2003). With y_s again fixed by equation (5.1), we should have:

$$NLES_{coarse\ outer} \sim \int_{y_s}^{\delta} \delta^2 \,/\, y^3 \, dy \sim \delta^+ \tag{5.7}$$

For the large near-wall region covered by a coarse mesh, it is similarly assumed that the resolution of this near-wall coarse mesh is comparable to that of the outer coarse mesh at its low bound. Therefore, a constant mesh spacing in this region should be $\Delta^+ \sim y_s^+$. We thus have:

$$NLES_{coarse\ inner} \sim {\delta^+}^2/(\Delta^+)^3 \cdot \int_0^{y_s^+} dy^+ \sim \delta^+ \tag{5.8}$$

Summing up all three parts for the overall mesh count, the mesh count scaling with Reynolds number will now be dictated by that of the global coarse meshes for both the outer and inner portions, equations (5.7) and (5.8). Therefore, the mesh scaling for WeLES should be:

$$N_{WeLES} \sim Re_{\tau} \tag{5.9}$$

This scaling can also be usefully contrasted to that for a full wall resolved LES (Jiménez 2003; Mizuno & Jiménez 2013): $N_{WRLES} \sim {Re_{\tau}}^{2}$.

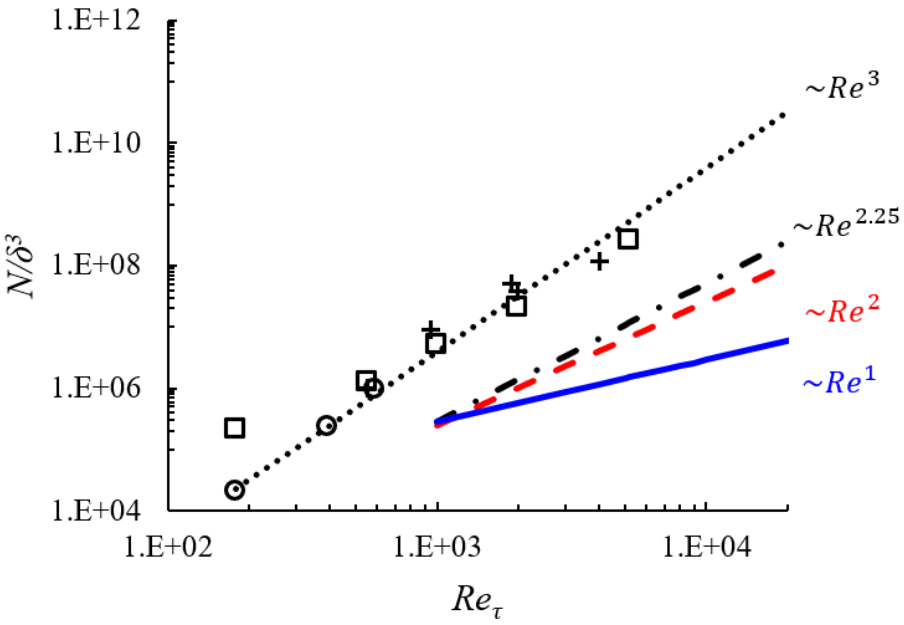


Figure 5.2. **Comparison of mesh count scaling with Reynolds number: full DNS (shown in black dots '▪▪▪'), full wall-resolved LES (shown in red dash lines '— —'), the present wall-embedded DNS, *'WeDNS'* (shown in black dashed dot lines '— ▪ —') and wall-embedded LES, '*WeLES*' (shown in blue solid lines '—'). Symbols are for published DNS, '□': Lee & Moser (2015); '+': Lozano-Duran & Jimenez (2014); '○': Moser, et al. (1999).**

Figure 5.2 presents the comparison in the mesh count scaling with Reynolds number among several well-established full DNS solutions (Lee & Moser 2015; Hoyas & Jimenez 2006; Lozano-Duran & Jimenez 2014; Moser, et al. 1999), full wall-resolved LES (WRLES) and the present two-scale approach for either a wall-embedded DNS (WeDNS) or a wall-embedded LES (WeLES). The mesh count – Re scaling results indicate that if a DNS calculation, for instance, is carried out at $Re_\tau \approx 1000$ requesting computing cost at approximately 10^{12} Mflops (Jimenez 2003), it only requires 10^7 Mflops for the two-scale method.

5.2 Implementation for channel flow case study

In this section, the baseline flow solution system will be briefly introduced first. The parameters for both DNS and LES channel flow case studies will then be defined.

5.2.1 Baseline flow solution method

For concept proof and general application purposes, the two-scale method is implemented in the open-source CFD solver OpenFOAM. The present work is focused on concept proof through case studies for canonical channel flows with the basic numerical set-ups being the same as the baseline LES case previously introduced in section 4.1.1. The baseline unsteady incompressible flow equations in a channel flow domain $\Omega = [0, L_x] \times [0, 2\delta] \times [0, L_z]$ are equations (4.2). The corresponding boundary conditions for the domain are provided in equation (4.3).

The flow equations are discretised in a finite volume scheme, with a second-order central difference scheme in space. The time advancement is achieved by a second-order Crank Nicolson scheme. A constant time-step is taken in keeping the maximum Courant numbers below 0.5. The pressure-implicit splitting operators (PISO) algorithm is used for solving the incompressible flow field.

5.2.2 Parameters for DNS and LES case studies

The implemented two-scale method is applied to a canonical turbulent plane channel flow at $Re_\tau \approx 550$, 1000, 2000, 4100 and 5200. The full computational domain sizes are $L_x = 2\pi\delta$ and $L_z = \pi\delta$, where δ is the half height of the channel

(Figure 3.1). The size of the computational domain corresponds to the minimum one used for full DNS simulations (Moser, et al. 1999; Lozano-Duran & Jimenez 2014). Thorough discussions on the effect of the domain size are made by Lozano-Duran & Jimenez (2014), where the same domain size as that used in the present work is proven to be adequate for reproducing one-point statistics of those larger ones. The global domain size is also the same as that adopted in Tang & Akhavan (2016).

The fully developed channel flow is driven by a set mass flow. Given a bulk mean velocity $U_b = \frac{1}{2\delta}\int_0^{2\delta} \bar{u}(y)\, dy$ in the streamwise direction, the present simulations are carried out at bulk Reynolds numbers in line with those of the published DNS data (Lee & Moser 2015; Hoyas & Jimenez 2006; Bernardini, et al. 2013). The simulations are initialised with a laminar parabolic Poiseuille profile (de Villiers 2006) and run for a sufficiently long time to reach a statistically steady state with mean statistics to differ less than 1%. The turbulence statistics to be reported are obtained by ensemble-averaging the flow quantities spatially in the two homogeneous directions and in time over at least ten eddy turnover times δ/u_τ.

Uniform grids are implemented in streamwise and spanwise directions. In the wall-normal direction (y), grids are allocated with a geometric stretching ratio of around 1.05. Within the local embedded DNS region, the mesh grid spacings Δx, Δy and Δz follow the DNS requirement (Bernardini, et al. 2013). Given the Kolmogorov scale at the wall $\eta_w^+ \sim 1.5$, the grid spacing in wall-parallel directions is $\Delta x \,/\, \eta < 7$ and $\Delta z \,/\, \eta < 5$. In the wall-normal direction, the largest grid spacing relative to the local Kolmogorov scale is at the interface between the embedded block and the global coarse-mesh region, where $(\Delta y \,/\, \eta)_{\max}$ is kept below 1.9.

DNS simulations are run for three Reynolds numbers: $Re_\tau \approx 550$, 1000 and 2000, with the details of the simulation parameters given in Table 5.1. Solutions for different mesh densities are also run to examine the mesh sensitivity at $Re_\tau \approx 550$, and the result for a refined mesh (denoted as '550-f') is also presented. The DNS results for validations will be presented and discussed in section 5.3.

Given the interest in developing an efficient method for applications at a moderate to high Re_τ in the order of at least $O(10^3)$ (Smits & Marusic 2013), the capability of the two-scale wall-embedded LES (WeLES) is also examined and demonstrated for higher Reynolds number cases, $Re_\tau \approx 2000$, 4100 and 5200. For the LES global coarse grids to resolve the energy-containing large scales as intended, the grid spacing follows that of Georgiadis, et al. (2010) and the scaling estimated in part ii of section 5.1.2. Details of the WeLES simulation parameters are given in Table 5.2. In the present calculations, the explicit sub-grid model is not included, the solutions can thus be regarded as implicit LES where the sub-grid scales are dampened by numerical dissipations. The results of the WeLES simulations will be presented and discussed in section 5.4.

Table 5.1 WeDNS simulation parameters within global (G) and local-embedded (L) domains

Re_τ	Domain	G: $L_x/\delta, L_z/\delta$ L: l_x^+, l_z^+	N_y	$\Delta_{y,w}^+, \Delta_{y,max}^+$	y_s/δ	Δ_x^+, Δ_z^+
550	G	$2\pi, \pi$	146	0.55, 16	0.13	40, 12
	L	3140, 432	35	0.55, 4		10, 6
550-f (finer mesh)	G	$2\pi, \pi$	172	0.55, 10	0.13	20, 12
	L	3140, 432	35	0.55, 4		10, 6
1000	G	$2\pi, \pi$	216	0.55, 18	0.1	43, 11
	L	3140, 393	48	0.55, 5		11, 5.5
2000	G	$2\pi, \pi$	282	0.55, 22	0.06	43, 11
	L	3140, 393	51	0.55, 6		11, 5.5

Table 5.2 WeLES parameters for global (G) and local-embedded (L) domains

Re_τ	Domain	G: $L_x/\delta, L_z/\delta$ L: l_x^+, l_z^+	N_y	$\Delta_{y,w}^+, \Delta_{y,max}^+$	y_s/δ	Δ_x^+, Δ_z^+
2000	G	$2\pi, \pi$	226	0.55, 41	0.06	55, 13
	L	3140, 393	51	0.55, 5		11, 6.3
4100	G	$2\pi, \pi$	264	0.55, 79	0.05	88, 21
	L	3140, 393	62	0.55, 7		11, 5.2
5200	G	$2\pi, \pi$	290	0.55, 100	0.04	110, 28
	L	3140, 393	64	0.55, 7		11, 4.7

5.3 Wall-embedded DNS

In this section, the results of the wall-embedded DNS will be presented for $Re_\tau \approx 550$, 1000 and 2000 in comparison with the DNS results of Lee & Moser (2015) and the 2-D spectral results from the DNS calculations of del Alamo, et al. (2004). The emphasis is placed on examining the validity of the present locally embedded two-scale methodology. In particular, attention is paid to the capability of the method in terms of the two major intended attributes: to adequately resolve the 'universal' near-wall small-scale turbulence dynamics and interactions within the

embedded block and to capture the 'foot-printing' of the large-scale structures of the outer flow on the near-wall region.

5.3.1 Mean Statistics

Figure 5.3 shows the mean velocity profiles in good agreement with the full DNS results. Table 5.3 presents the predicted wall shear stresses compared with the values of the published DNS as the target. All the present calculations are set to match the bulk flow Reynolds numbers Re_b of the DNS results. The comparisons between $Re_{\tau,computed}$ and $Re_{\tau,target}$ indicate the accuracy of the wall shear stress prediction. The errors are all within 2%.

Also shown in Figure 5.3 are the predicted turbulence intensities and the Reynolds stresses ${u^+_{rms}}^2$, ${v^+_{rms}}^2$, ${w^+_{rms}}^2$ and $\overline{u'v'}^+$ where the subscript 'rms' denotes the root mean squared values. In general, the local DNS solutions (denoted as '*Local-fine*') within the local embedded fine-mesh block match up with the full DNS. The coarse mesh solutions behave differently in the two global regions. In the outer region (denoted as '*Coarse-outer*'), the coarse mesh solutions agree well with the corresponding full DNS both in terms of the mean flow velocities and the turbulence statistics. The results of '*550-f*' (Table 5.1) with a finer mesh are also presented, which are in good agreement with the standard mesh resolution ('*550*' in Table 5.1). The two solutions from the two meshes of different resolutions are almost indistinguishable in the outer region. The large-scale structures are resolved on the global coarse grids regarding both the mean and the fluctuations. The outer 'energy plateau' of the turbulence fluctuations in the streamwise direction is captured by the global coarse mesh, most clearly at the highest Reynolds number.

Table 5.3 Wall shear-stress prediction of the two-scale WeDNS approach

$Re_{\tau,target}$	Re_b	$Re_{\tau,computed}$	Error in τ_w (%)
544	10000	548	+1.5
1001	20000	995	-1.2
1994	43650	1989	-0.5

For the near-wall region of the global coarse-mesh ('Domain 3' as shown in Figure 3.1, named as '*Coarse-inner*'), the agreement between the present solution and the reference DNS can only be observed for the time-mean velocities Figure 5.3(a), (c) and (e). It is noted however that the magnitude of turbulence fluctuations in the global near-wall inner region tends to be over-predicted, most noticeably for the streamwise components in Figure 5.3(b), (d) and (f). It should be remarked that the overriding factor in the global near-wall inner region is the under-resolution of the local coarse mesh. The lack of sufficiently resolved small scales locally should correspond to a lack of dissipation, and thus the over-estimation of the local turbulence fluctuations is expected. Nevertheless, the under-resolved global inner region still serves in receiving the 'foot-printing' of the large-scale structures from the outer-flow region, which in turn will feed into the embedded fine-mesh block through the direct interfacing treatment at the coarse mesh resolved level as discussed in section 3.2. The source-term correction of the upscaled flow equations (3.12) is effective only in driving the time-averaged coarse-mesh flow field towards the *space-time averaged* target solution of the embedded fine-mesh block. This

primary objective of the present work seems to be met adequately as demonstrated by the comparisons in the mean flow velocity profiles as shown in Figure 5.3(a), (c) and (e).

For consistency of the two-scale methodology in the context of the global and local domain partitioning (Figure 3.1b), the correction source terms activated in the global inner domain ('Domain 3') arisen from the upscaling should approach zero smoothly when approaching from the inner region to the inner-outer interface in the wall-normal direction. Figure 5.4 presents the distributions of the source terms in the wall-normal direction, for the total source terms $\boldsymbol{ST}_{st}$ consisting of the fine-mesh space-time averaging term $(\boldsymbol{ST}_{st})_f$ and the coarse-mesh time-averaging term $(\boldsymbol{ST}_t)_C$ in equation (3.13). As can be observed from Figure 5.4, these terms are all decreasing asymptotically to become negligible when approaching the inner-outer interface. This indicates that the global coarse-mesh resolution at the interface is sufficiently fine to resolve the local flow directly. Thus, no corrections should be arisen through the upscaling around the interface. The diminishing source terms approaching the interface also are in line with the assumption that the feedback from the inner region 'modulation' on those large structures in the outer flow region should be negligibly small, as discussed in section 5.2.1 and further considered in Appendix. It should be mentioned that the source terms in the spanwise direction, including $(\boldsymbol{ST}_{st})_{f,z}$, $(\boldsymbol{ST}_t)_{C,z}$ and $\boldsymbol{ST}_{st,z}$, are much smaller than those in the streamwise and wall-normal directions, thus are not shown here.

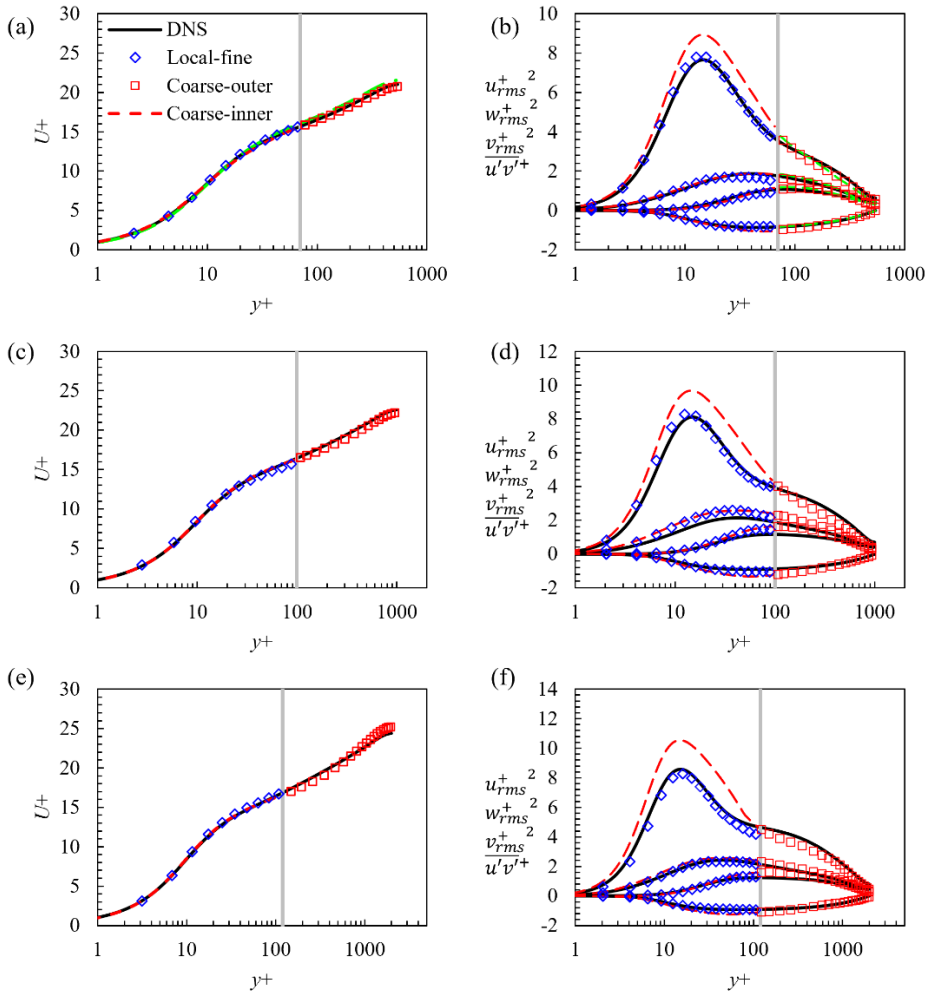


Figure 5.3. **Mean velocity profiles in (a, c, e) and turbulence fluctuations in (b, d, f) compared with the DNS (Lee & Moser 2015) in black solid lines '—'. The results are at: (a, b) $Re_\tau \approx 550$; (c, d) $Re_\tau \approx 1000$; (e, f) $Re_\tau \approx 2000$. The blue diamonds '◊' indicate results within the local fine-mesh block. The red symbols '□' and dashed lines '- -' indicate results in the global coarse outer and inner region. The green dashed lines '— —' in (a, b) are the results of a finer mesh '550-f' in the global region. The vertical grey solid lines '—' mark the interface location y_s. Not all data points are included for readability.**

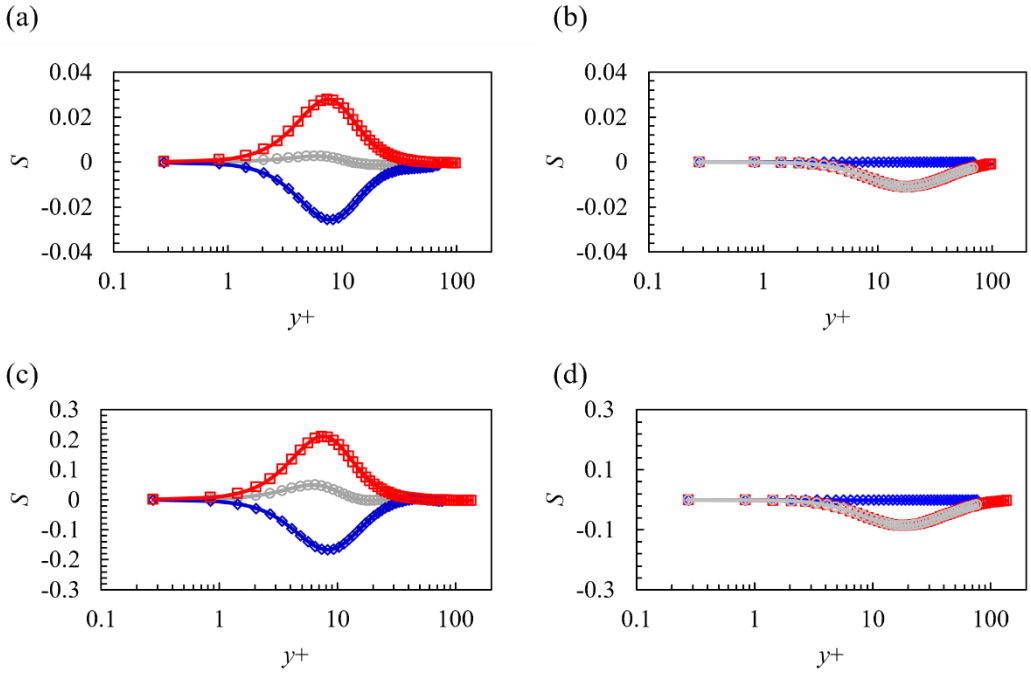


Figure 5.4. **Source term profiles in relation to wall distance y^+ at two Reynolds numbers: (a, b): $Re_\tau \approx 1000$; (c, d) for $Re_\tau \approx 2000$. $(ST_{st})_f$ are shown in blue diamonds '◊'. $(ST_t)_C$ are shown in red squares '□'. ST_{st} are shown in grey circles '○'. (a, c): Source terms in the streamwise direction. (b, d): Source terms in the wall-normal direction.**

5.3.2 Spectral Analysis

A key aspect pertinent to the validity and effectiveness of the locally embedded methodology is its ability in capturing and resolving a range of turbulence scales. To examine this, spatial spectral analyses on a near-wall plane are carried out. The wall-normal location commonly taken for such analyses is that around the 'universal' first peak of turbulence fluctuations at $y^+ = 13.5$. Figure 5.5(a) shows the velocity field snapshot on this plane, on which the embedded block is also

marked. Two points are worth noting here. Firstly, the large meandering streaky structures are clearly captured by the global near-wall coarse mesh, which in turn feed into the embedded fine-mesh block through the direct interfacing treatment at the coarse-mesh resolved level, as discussed in section 3.2. Thus, the local fine-mesh block will be influenced directly by the large structures captured in the global coarse-mesh domain through both the top interface and the side interfaces (Figure 3.1). Secondly, the fine mesh of the embedded block is enabled to provide a local high resolution effectively thanks to the fine-scale fluctuation-based periodic condition. The two scale characteristics in the fine-mesh block and the surrounding coarse-mesh regions are clearly seen in Figure 5.5(b) showing vortical structures and Figure 5.6 showing the near-wall vorticity fields on an x-y plane.

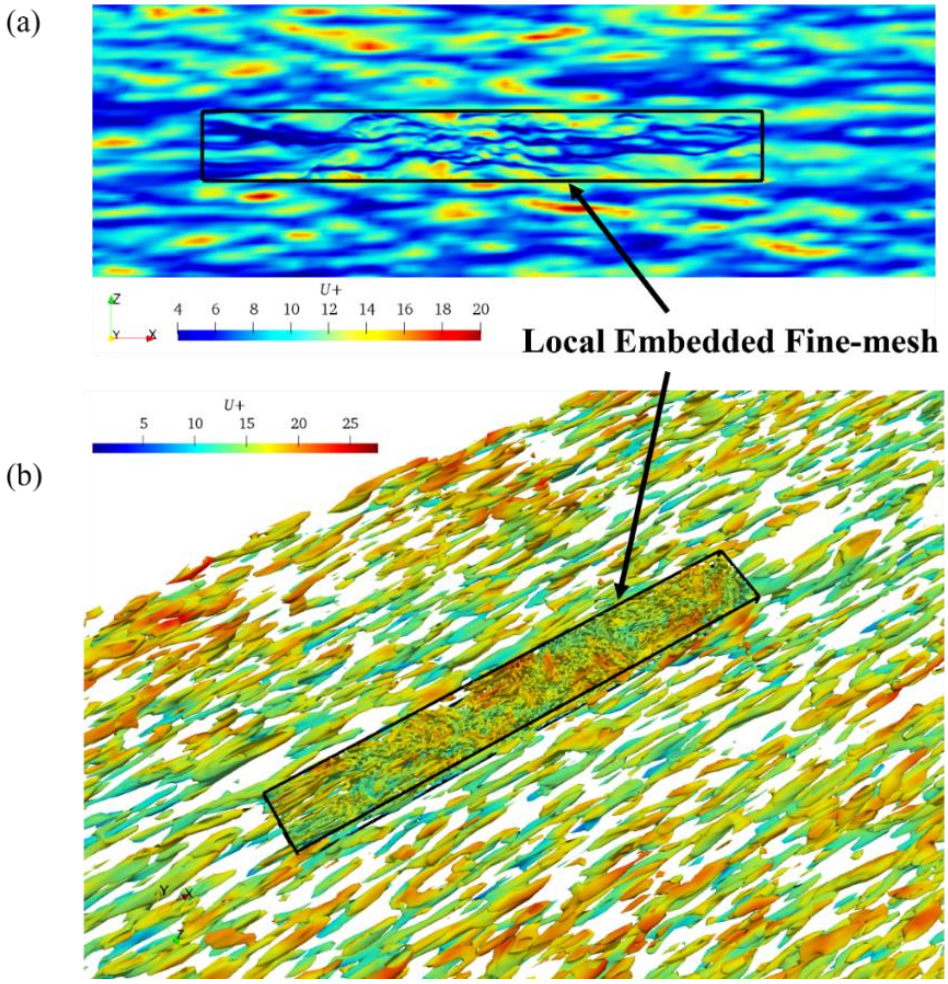


Figure 5.5. **(a) The $x-z$ plane snapshot of the instantaneous velocity field around the embedded block at the inner location $y^+ = 13.5$. (b) iso-contours of the second invariant of the velocity gradient tensor (Jeong & Hussain, 1995), coloured with the instantaneous velocity. The solid black boxes mark the embedded fine-mesh block.**

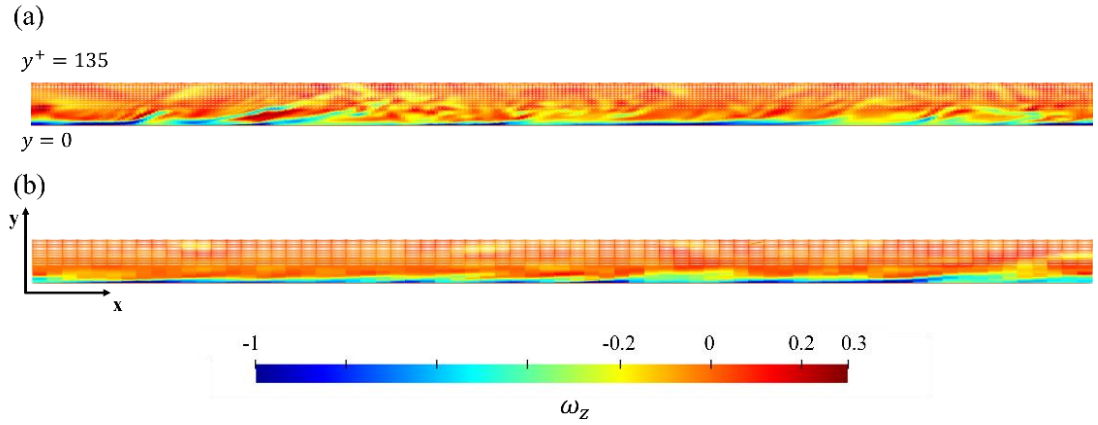


Figure 5.6. **The x-y snapshot of the spanwise vorticity ω_z field near wall: (a) the local embedded DNS region (b) the global coarse-mesh region. Contour values are normalized by the maximum magnitude.**

Figure 5.7 shows the one-dimensional streamwise energy spectra. The global-coarse mesh covers adequately the large scales. However, it is clearly under-resolved at higher wave numbers. The profiles of the coarse-mesh spectra deviate from the full DNS, being over-predicted first at intermediate wave numbers, e.g., around $k_x \approx 40$ (Figure 5.7a), and then underpredicted at higher wavenumbers for small scales of the dissipation range. The resolution dependency is more strongly manifested in the energy spectra as a function of the streamwise wavenumbers k_x (Figure 5.7a) than those of the spanwise wavenumbers k_z (Figure 5.7b). For the high wave-number part in the spectra, the numerical dissipation caused by the under-resolution of the coarse grids results in a much more abrupt drop of energy (Figure 5.7a). On the other hand, the embedded block is sufficiently fine to resolve small scales down to the Kolmogorov ones in the near-wall region, reflected by the predicted spectra at higher wavenumbers. As discussed earlier, the embedded fine-

mesh block is able to receive the disturbances of the long wavelength dictated by the global domain size adopted.

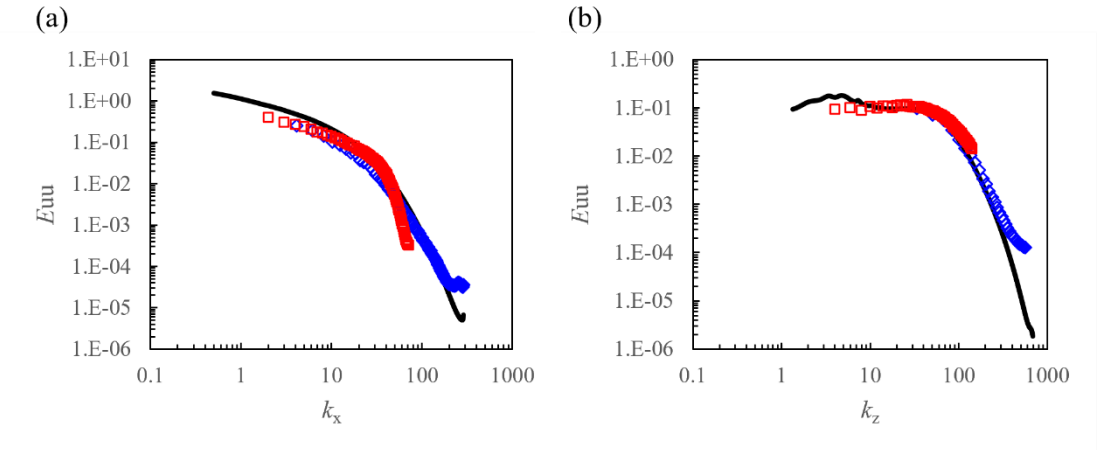


Figure 5.7. **One-dimensional energy spectra at $y^+ = 13.5$ at $Re_\tau \approx 1000$ as functions of (a) streamwise wavenumbers k_x and (b) spanwise wavenumbers k_z compared with DNS results (Lee & Moser 2015) in black solid lines '—'. The blue diamond symbols '◊' and red symbols '□' indicate the results within the local fine-mesh block and in the global coarse-mesh region, respectively.**

It is emphasised that although the present method is phenomenologically based on a two-scale framework, there is no spectral gap between the two scales assumed, nor is such spectral gap or separation observed in either the spatial spectra from the two domains (Figure 5.7) or the temporal counterparts (Figure 5.8).

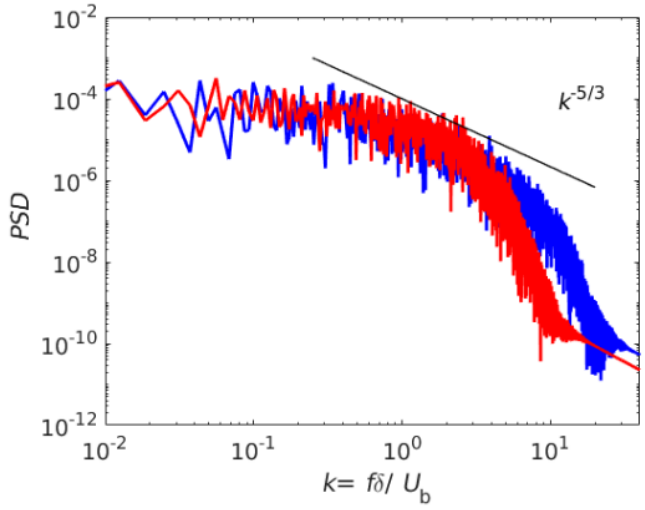


Figure 5.8. **Turbulence power spectra density (PSD) as functions of the non-dimensional frequency at $Re_\tau \approx 1000$ at two locations of the same wall normal distance $y^+ = 13.5$: at the middle of the embedded fine-mesh block (in blue lines '—') and at a coarse-mesh point outside the embedded block (in red lines '—').**

The most noteworthy feature of the results shown in Figure 5.8 is the overlapping of the two spectra from the fine- and coarse-mesh domains respectively. The smooth overlapping of the two spectra in good agreement with the full DNS indicates that the fine-mesh block is subject to turbulence disturbances of a full spectra range. In contrast, if a global domain solution is indirectly coupled with a small fine-mesh domain with a direct periodic condition (as in commonly adopted MFU), discontinuous spectra from the two domains may occur (Tang & Akhavan 2016). A more direct illustration of the length scale range captured by the fine-mesh solution of the embedded block is provided by a local frequency power spectral density (PSD) as shown in Figure 5.8, where the dimensionless frequency is taken based on the half channel height and bulk flow velocity: $k = f\delta/U_b$. It is worth

noting that the PSD taken from the middle of the embedded block confirms a full coverage of the spectra range in the locally fine-mesh block. On the other hand, the global coarse-mesh region is clearly subject to an under-prediction for the small-scale high-frequency part as expected.

Figure 5.9(a) and (c) show the one-dimensional pre-multiplied energy spectra $k_z\Phi_{uu}{}^{+}$ of the inner embedded DNS region compared with the full DNS results. The counterpart spectra processed from the global coarse-mesh results are shown in Figure 5.9(b) and (d) indicating a notable discrepancy in the near wall for the dominant shorter-wavelength part. The overprediction of the streamwise velocity fluctuations due to the local under-resolution in the global inner near-wall region is consistent with the mean statistics as shown in Figure 5.3. The boxes with the vertical black lines indicate the embedded fine-mesh block size in the spanwise direction. It is clear that the inner ‘universal’ energy peak is sufficiently covered in the embedded block, in line with that illustrated in Figure 5.1. The longer-wavelength disturbances are well captured in the global coarse-mesh domain as shown in Figure 5.9(b) and (d).

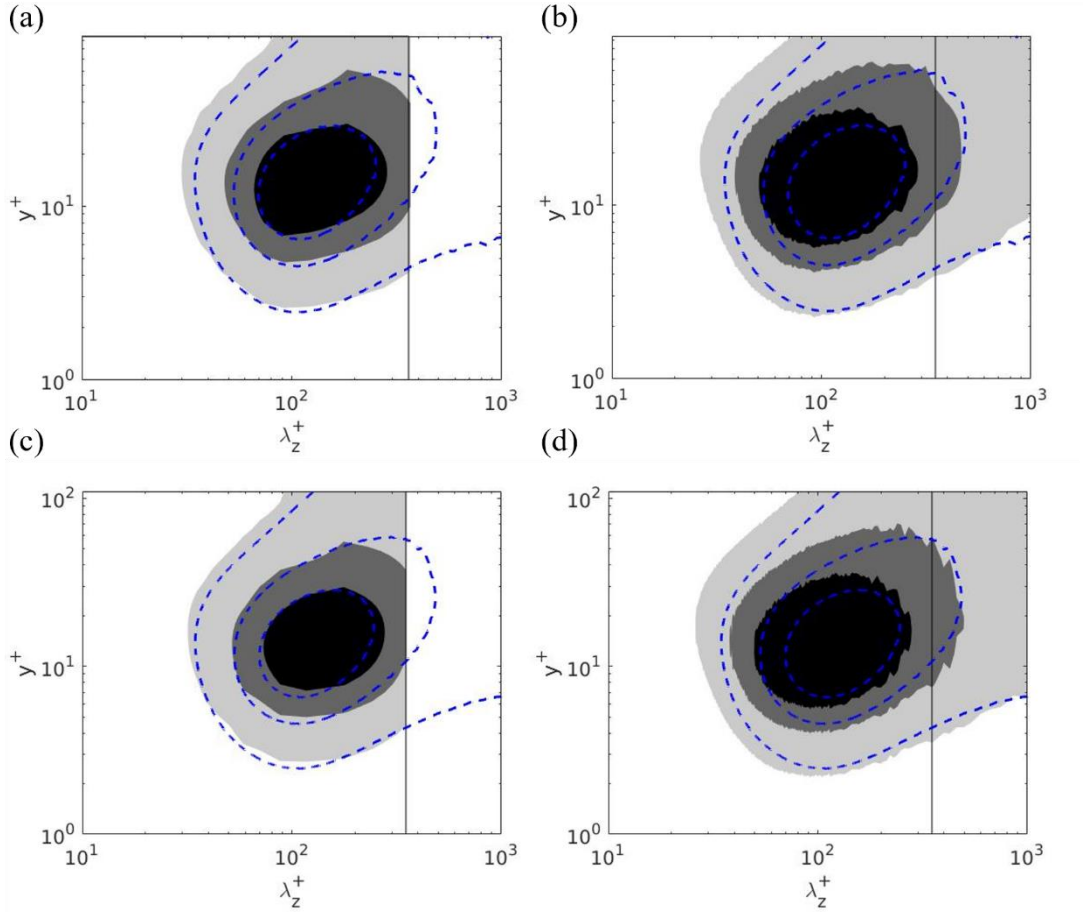


Figure 5.9. **One-dimensional pre-multiplied enegy spectra $k_z\Phi_{uu}{}^+$ (a, c) the present results within the embedded block with the blue-dashed lines showing the results from the full DNS database (Lee & Moser 2015); (b, d) the present results of the global coarse region compared with the same full DNS results. The countour levels are 0.5/1.5/2.5. Results in (a, b) are at $Re_\tau \approx 1000$. Results in (c, d) are at $Re_\tau \approx 2000$. Black solid lines indicate the size of the embedded block.**

After examining the inner region and the local embedded block, we now evaluate the resolutions in the outer-flow region. Attention is paid to a plane at the outer location $y_{out}^+ \approx 3.9\sqrt{Re_\tau}$, within the log-law region, which is taken by Marusic, et al. (2010) as the location where the 'outer signals' can be extracted as

input for their two-scale model. The grid resolution of the global coarse mesh is examined to see if the local small scales of the large energy-containing structures can be sufficiently resolved. Figure 5.10 shows the two-dimensional pre-multiplied energy spectra $k_x k_z \Phi_{uu}$ in relation with streamwise wavelengths and spanwise wavelengths. As can be seen, the coarse mesh resolves outer large scales down to $\lambda^+ \approx 10^2$ well in comparison with the full DNS data (del Alamo, et al. 2004).

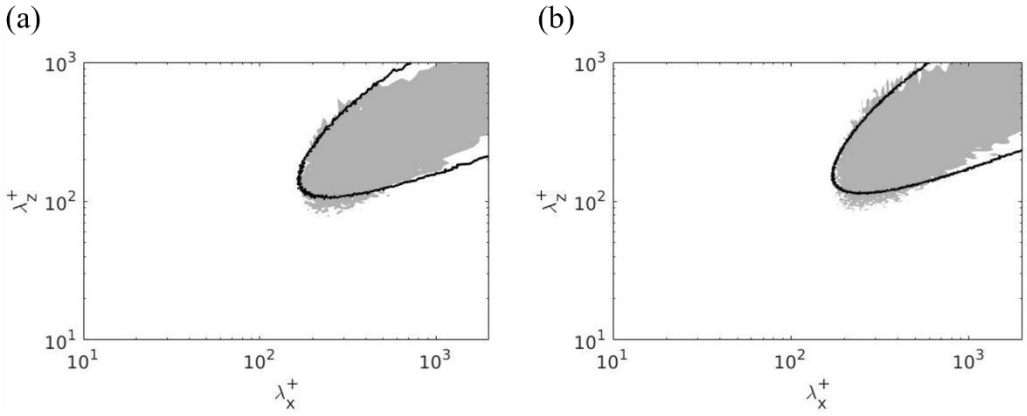


Figure 5.10. **Two-dimensional pre-multiplied energy spectrum $k_x k_z \Phi_{uu}$. The present results are (in shade) compared with the DNS (solid lines) (del Alamo, et al. 2004) at the outer location $y_{out}^+ \approx 3.9\sqrt{Re_\tau}$ at two Reynolds numbers: (a) $Re_\tau \approx 1000$ (b) $Re_\tau \approx 2000$. The contour levels are (a) 0.035 (b) 0.025 of the local streamwise intensity.**

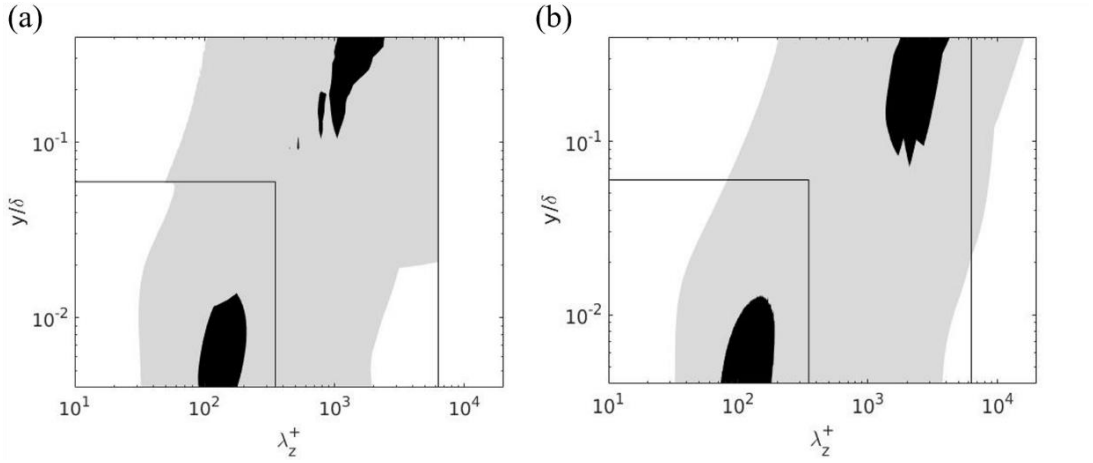


Figure 5.11. **One-dimensional pre-multiplied energy spectra $k_z\Phi_{uu}$ at $Re_\tau \approx 2000$. Present results in (a) are compared with the DNS (Lee & Moser 2015) in (b). The contour levels are 0.05/0.35 of the local intensity. The inner smaller box marks the local embedded block, while the larger box marks the global full domain used.**

Figure 5.11 shows the one-dimensional pre-multiplied energy spectra $k_z\Phi_{uu}$ as functions of spanwise wavelengths λ_z^+ and wall distances y^+. These results underscore the existence of two energy peaks predicted by the present WeDNS in comparison with the full DNS (Lee & Moser 2015): the first inner one located at $y^+ \approx 13.5$ and the second outer one located in the log-law region, stretching from $y^+ \approx 3\sqrt{Re_\tau}$ to $y/\delta \approx 0.3$. The inner and outer energy peaks both can be observed in the present results (Figure 5.11a). The inner region within the local embedded fine-mesh block is marked by the smaller black box. The first energy peak is with the dominant spanwise wavelength of around $\lambda_z^+ \approx 10^2$. The task to capture and resolve the first energy peak and near wall small-scale dynamics is carried out in the fine-mesh embedded DNS block where the local solutions agree very well with the full DNS, as shown previously in Figure 5.9(a) and (c). The second peak in the outer

flow region contributed by the energetic large scales reaches a maximum beyond $y_s^+ = 3\sqrt{Re_\tau}$ that extends to the middle of the channel with the dominant spanwise wavelength of $\lambda_z^+ \approx O(10^3)$ (Agostini & Leschziner 2014) in wall unit or $\lambda_z \approx \delta$ in the outer dimension. Note that the largest scales approaching the middle of the channel are cut off by the limited global domain size adopted in the present study. The influence of even larger scales is discussed by Lozano-Duran & Jimenez (2014), which is beyond the scope of the thesis.

5.3.3 'Foot-printing' and 'Modulation' in Near-wall Region

In this section, we will examine the instantaneous flow field in the near-wall region with an emphasis on scale interdependence and interactions. The 'foot-printing' effect of the outer flow large structures on the near-wall flow motions will be examined by correlating the inner flow large scales to those of the outer flow. Furthermore, we will also analyse the interaction between the large coherent scales and small scales in a form of corresponding intermediate scales ('modulation') in the near wall region.

The Huang-Hilbert EMD method (Huang, et al. 1998) method is applied to the instantaneous raw field of the present WeDNS at $Re_\tau \approx 2000$. The algorithm splits the original signals into a set of Intrinsic Mode Functions (IMFs) based on local characteristic scales without introducing any cut-off wavelengths. This EMD method of a two-dimensional version is applied to decompose small- and large-scale components in DNS channel flows notably by Agostini & Leschziner (2014, 2016, 2019). In the present work, with the implementation of the EMD code originally developed by Bhuiyan, et al. (2008), the last three of eight IMFs are retained as the

long-pass filtered large-scale flow field. The raw data of instantaneous streamwise velocity fluctuations at an inner and outer location are shown in Figure 5.12(a) and (b) respectively. The filtered large-scale structures of the inner field (Figure 5.12c) show a clear resemblance to those of the outer flow when the local fine scales are filtered out (Figure 5.12e). These filtered inner and outer fields are further compared by matching the zero-value contour lines of the outer flow contours (Figure 5.12e) and the positive-value contours of the inner flow (Figure 5.12c), leading to the composite contour plot in Figure 5.12(d). Note closely that the near-wall large scales travel continuously across the coarse-fine interface (Figure 5.12c and d), similarly to the contour lines cut across the interfaces smoothly seen previously in Figure 5.5.

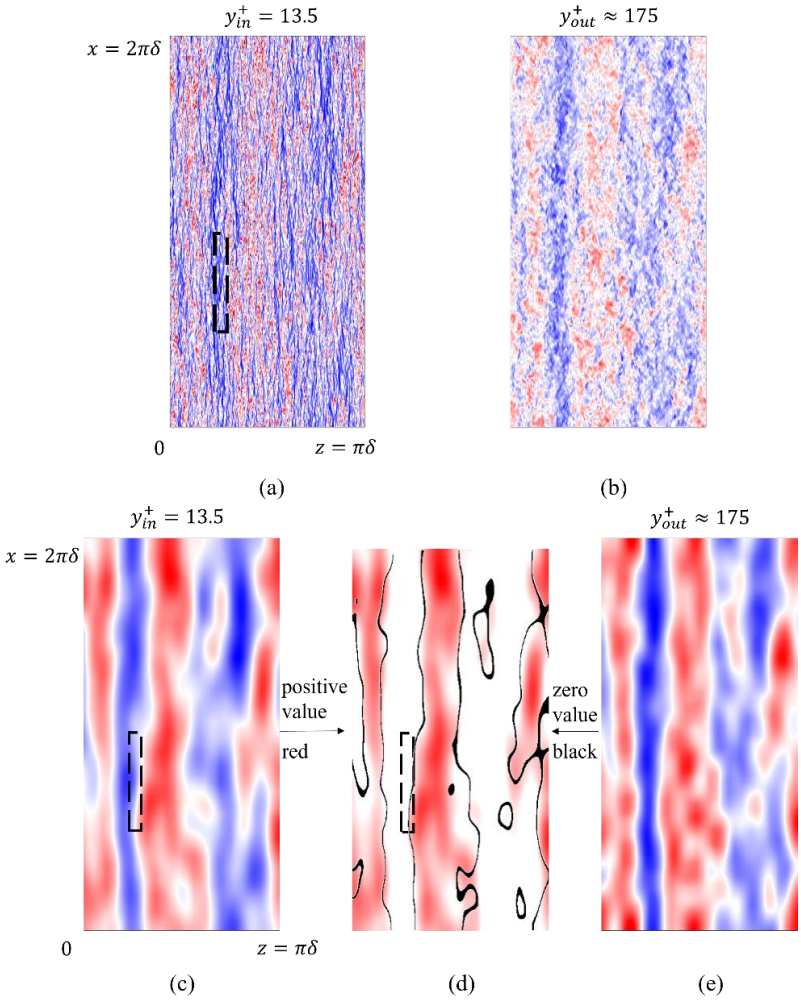


Figure 5.12. **Illustration of the 'foot-printing' effect. (a) original inner instantaneous velocity field at the location $y_{in}^+ = 13.5$; (b) original instantaneous velocity field at $y_{out}^+ \approx 3.9\sqrt{Re_\tau} \approx 175$; (c) long-wavelength pass filtered field of (a); (d) red contours for the positive value of (c) while black lines sketch the zero envelop of (e); (e) long-wavelength pass filtered field of (b). In (d), the outer field snapshot is adjusted as per the inclination angle in y to be compared with the inner. All contours range from -3 (blue) to +3 (red) standard deviations of each field. Black dashed boxes indicate the embedded fine-mesh block.**

Recognising that the global coarse mesh for the whole domain under-resolves the disturbances when approaching the wall, we nevertheless can still observe clear correlations between inner and outer large-scale coherent structures. This is taken as the evidence of the ‘foot-printing’ of the outer scales on the inner region, providing the signatures of the large scales of the global outer field on the locally embedded fine-mesh block.

Figure 5.13 is generated to illustrate the scale interactions between the large ‘foot-prints’ and the small local scales in the form of ‘modulation’ (Mathis, et al. 2009), manifested in the presence of some intermediate structures enveloped (conditioned) by the large structures of the outer flow. The inner small-scale fluctuations are retained in Figure 5.13(b) by simply removing the large scales. This is enabled by subtracting the long-wavelength-pass filtered field shown in Figure 5.12(c) from the near-wall raw field in Figure 5.13(a), similarly to Marusic, et al. (2017). We then apply the long-wavelength-pass filter to the small-scale fluctuations and retain only the ‘positive’ islands shown in Figure 5.13(c). The ‘foot-printing’ as demonstrated in Figure 5.12(d) is duplicated in Figure 5.13(d). The presence of intermediate scales is clearly seen in Figure 5.13(c).

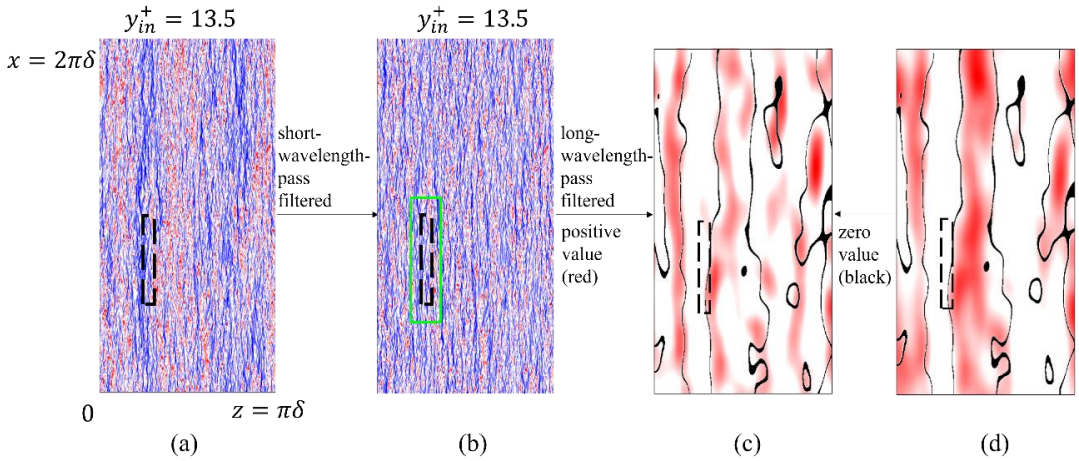


Figure 5.13. **Illustration of the 'modulation'. (a) the original instantaneous velocity field at the inner location $y_{in}^+ = 13.5$, i.e., duplication of Figure 5.12(a); (b) equivalent short-wavelength pass filtered field of (a), i.e., the raw field minus the filtered flow field in Figure 5.12(c); (c) long-wavelength pass filtered field of (b) with only contours of positive values retained, to be compared with the zero envelops of (d); (d) duplication of Figure 5.12(d) showing the large-scale 'foot-prints'. All contours range from -3 (blue) to +3 (red) standard deviations of each field. Black dashed boxes indicate the local embedded fine-mesh domain.**

The near-wall incoherent scales are the local 'universal' small scales modulated by the large-scale movement. We compare Figure 5.13(c) and (d) more closely in a closeup of the embedded fine mesh region in Figure 5.14. The 'modulation' being the small-scales response to the large-scales is seen to correlate to the near-wall large-scale structures, therefore is fused with the 'foot-prints'. If we inspect the length-scale discrepancy of the near-wall coherent large scales (Figure 5.13d) and the near-wall incoherent scales (Figure 5.14a), we can easily observe that the former naturally is much larger than the size of the embedded block, while the latter is much smaller and well resolved by the local fine-mesh DNS. The

'modulation' due to the inter-scale interaction appears at the intermediate scales (Figure 5.14b).

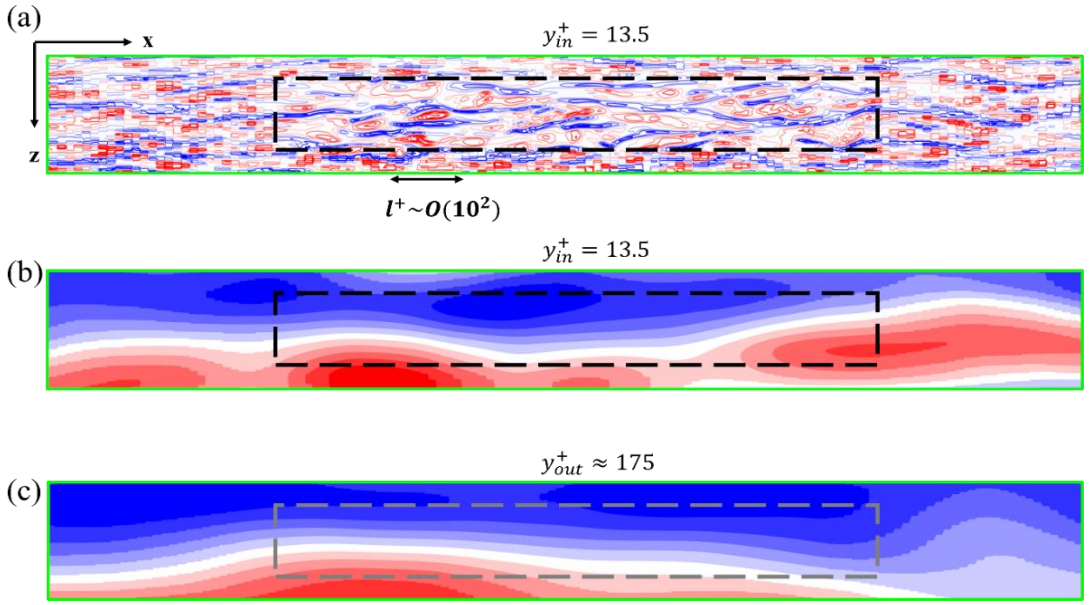


Figure 5.14. **The instantaneous velocity fields at the vicinity of the embedded region as the green box in Figure 5.13(b) enlarged. (a) local small-scale-pass filtered field near wall; (b) intermediate scales indicative of the 'modulation' (close-up view of Figure 5.13c with negative values added as shown in blue); (c) outer large-scale-pass filtered field (close-up view of Figure 5.12e). The black dashed boxes in (a) and (b) mark the local embedded block. The grey dashed box in (c) indicates the corresponding location of the embedded block underneath.**

5.4 Wall-embedded LES

In this section, the potential applications of the two-scale approach are illustrated for WeLES cases at Reynolds numbers $Re_\tau \approx 2000$, 4100 and 5200. The results are compared with the existing DNS database (Lee & Moser 2015;

Bernardini, et al. 2013). Once again, a given mass flow rate is targeted to match the same Re_b as that of a full DNS. The mean velocity profiles predicted by the present WeLES are shown in Figure 5.15(a), (b) and (c), in good agreement with the corresponding DNS data for the three Reynolds numbers, respectively.

The comparisons between the computed Reynolds number based on the friction velocity $Re_{\tau,computed}$ and those targeted $Re_{\tau,target}$ are presented in Table 5.4 indicating the accuracy of the wall shear stress prediction. The cases computed by using the present two-scale method are labelled as '*Two-scale2000', 'Two-scale4100'* and *'Two-scale5200'* for the three nominal Reynolds numbers respectively. Also included in the table are the two high Reynolds number (4100, 5200) cases computed without the source term coupling in the global inner region. These two computed cases without the source-term coupling are effectively single-scale direct solutions, thus are labelled as *'One-scale4100'* and *'One-scale5200'* for the two Reynolds numbers respectively. The errors of the two-scale method solutions are all well within 1% for these two high-Reynolds-number cases. In contrast, a much larger error (~15%) results from the near-wall coarse-mesh under-resolution when no source term corrections are applied as in the direct one-scale solutions. The mean velocity profile in a closeup in the near-wall region predicted by the one-scale solution is compared to the two-scale and the DNS results as shown in Figure 5.15(d), in which the impact of the source term correction is clearly highlighted.

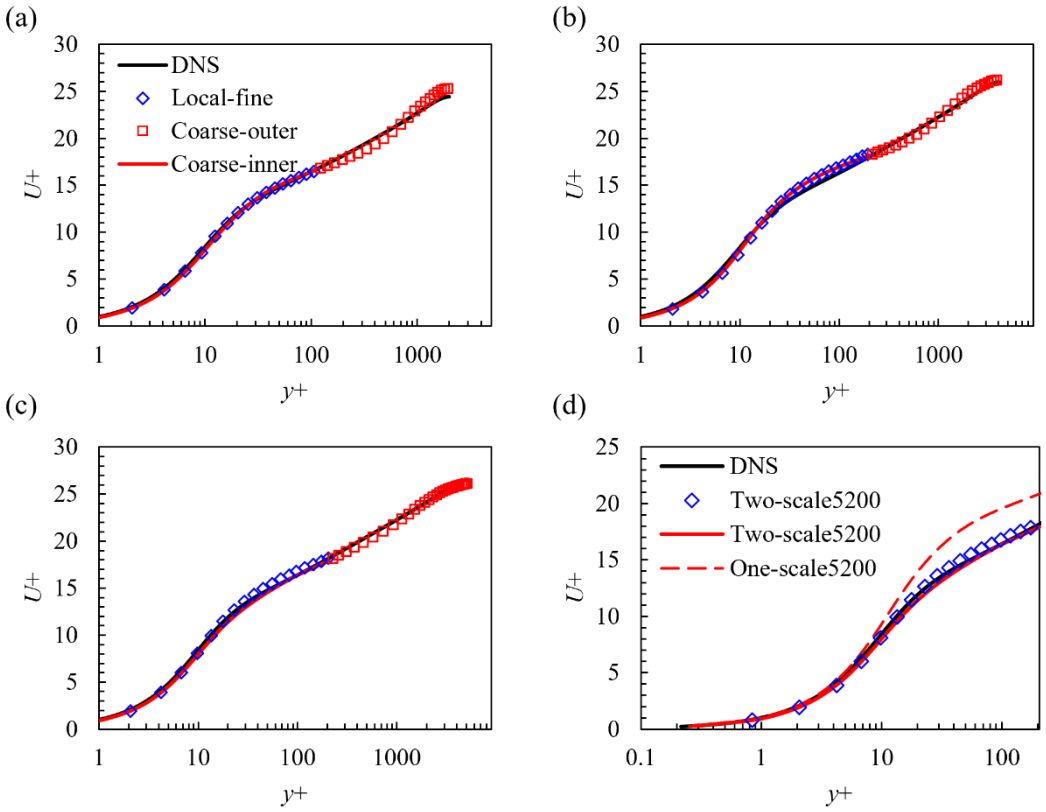


Figure 5.15. **Mean velocity profiles at high Reynolds numbers: (a) $Re_\tau \approx 2000$; (b) $Re_\tau \approx 4100$; (c) $Re_\tau \approx 5200$. The blue diamond symbols '◊' indicate results within the local fine-mesh block. The red symbols '□' and red solid lines '▬' indicate results in the global coarse outer and inner region respectively. (d): Comparison in the mean velocity between the one-scale direct solution ('*One-scale5200*' shown in the dashed red line '- -') and the present solutions ('*Two-scale5200*') with the source-term coupling on the same mesh grids at $Re_\tau \approx 5200$. Note that not all data points are included to increase readability.**

Table 5.4 Wall-shear-stress prediction of the two-scale WeLES approach

Cases	$Re_{\tau,target}$	Re_b	$Re_{\tau,real}$	Error in τ_w (%)
Two-scale2000	1994	43650	1991	-0.3
Two-scale4100	4079	95667	4062	-0.8
One-scale4100			3764	-14.9
Two-scale5200	5186	125000	5172	-0.5
One-scale5200			4764	-15.6

Extra attention is paid to the local fine-mesh block of the WeLES. Although this is an LES case, the local embedded block is assumed to be able to capture the inner energy peak as well as in a full DNS. The energy spectrum of the inner embedded block solution is shown in Figure 5.16, which agrees well with the DNS.

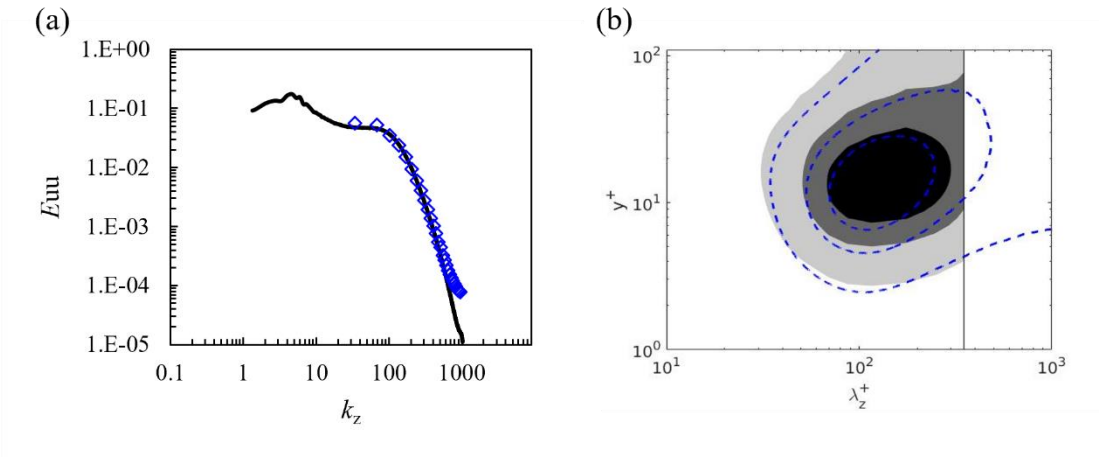


Figure 5.16. **Inner energy spectra. (a) The one-dimensional energy spectrum at $y^+ = 13.5$ in relation to spanwise wavenumbers within the local fine-mesh block (blue diamonds '◊') compared with the DNS results (Lee & Moser 2015) at $Re_\tau \approx 2000$. (b) One-dimensional premultiplied enegy spectrum $k_z \Phi_{uu}^+$ in relation to wavelengths and wall distance in the inner region within the embedded block compared with the dashed contour lines for the DNS results from the database (Lee & Moser 2015) at $Re_\tau \approx 2000$. The contour levels are 0.5/1.5/2.5.**

Finally, Figure 5.17 presents the estimated mesh-count scaling with Reynolds number compared with the actual mesh count values adopted for the present WeLES computations. The two-scale approach with the locally embedded fine-mesh solution presents a remarkable potential for computational efficiency gains.

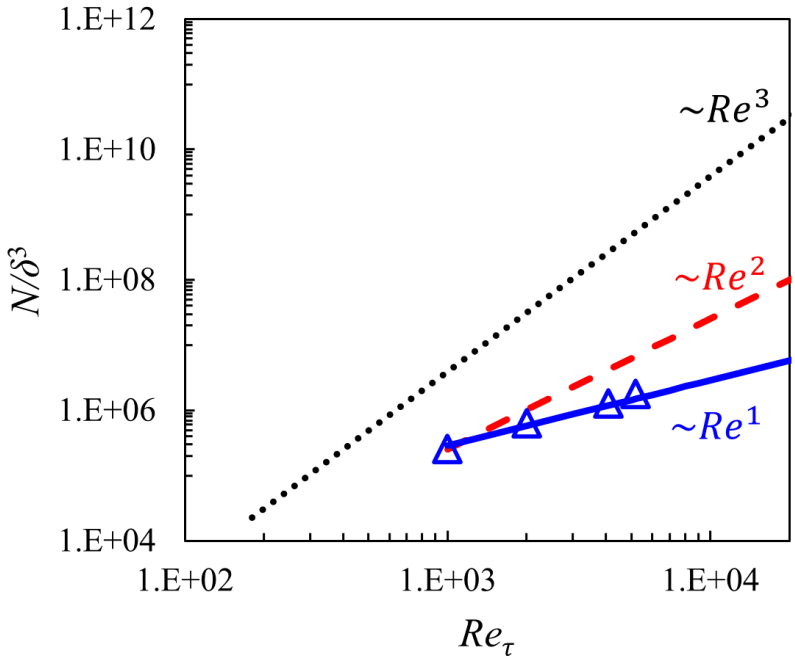


Figure 5.17. **Comparison in mesh count scaling with Reynolds number: the full WRLES (shown in red dash lines '— —') and the present two-scale WeLES (shown in blue solid lines '—') underlined by the actual mesh counts of the present WeLES cases (shown in blue triangles 'Δ'). The full DNS scaling (shown in black dots '▪▪▪') is also included.**

5.5 Summary

When seeking an efficient and accurate solution for wall-bounded turbulent flows by coupling a local near-wall fine-mesh block with a global coarse-mesh domain, we face two challenging issues: firstly how to capture and resolve the distinctive influence of large-scale turbulences of the outer flow region on the near-wall turbulence as clearly established and consistently substantiated in recent

research findings, and secondly how to correct the under-resolved global coarse-mesh near-wall region outside the local fine-mesh block.

We develop a two-scale method with a locally embedded fine-mesh block generated by sub-dividing the base coarse mesh cells in the near-wall region. The wall-normal height of the fine-mesh block is taken at the low bound of the log-law region (Marusic, et al. 2013) and the streamwise and spanwise sizes are taken based on the spatial spectra of the full DNS data (Lee & Moser 2015) to ensure sufficient coverage of the resolved 'universal' small-scale dynamics and the associated turbulence peak region for a wide range of Reynolds numbers. Correspondingly, the base coarse-mesh resolution in both the global outer flow and global near-wall regions is assumed to be sufficiently fine to capture and resolve all large-scale turbulence structures.

The influence of the large-scale structures on the locally embedded fine-mesh block is captured by a novel scale-dependent interface treatment with the distinctive and closely relevant capability, compared to previously commonly adopted minimum flow unit (MFU) based methods. The coarse-mesh scale resolved disturbances can now be directly exchanged across a coarse-fine mesh domain interface, whilst only are the fine-mesh resolved fluctuations around the coarse-mesh variables subject to the periodic condition at the pairing boundaries of the fine-mesh block in the two wall parallel directions respectively. The results through scale filtering re-composition clearly indicate the 'foot-prints' of the outer flow large structures on the local embedded block, as well as the intermediate scales expected from the large-small scale interactions ('modulation'). In this two-scale framework, we make no assumptions in relation to the need for presence of a scale separation or

spectral gap between the disturbances of the global coarse-mesh domain and those of the local fine-mesh one. The spatial energy spectra predicted by the present two-scale method exhibit a substantial range where the two spectra obtained from the two domains overlap smoothly. The smooth overlapping of the spectra is a manifestation of the wide and continuous range of the length scales of disturbances captured by the present two-scale coupled system. More importantly, as confirmed by a single-point temporal spectrum, the local fine mesh domain is shown to be subject to a full range of length scales from the smallest scales resolved locally to the largest one dictated by the global domain size.

The global coarse-mesh in the near-wall region is under-resolved as expected. We resort to upscaling the time-averaged and locally volume-averaged fine-mesh solution for each coarse-mesh cell to set a target solution for the coarse-mesh region outside the embedded fine-mesh block. The corresponding forcing source terms generated from the target solution of the fine-mesh block, are directly mapped to the corresponding coarse-mesh cells in the global inner domain, given the homogeneity of the time-averaged field in the streamwise and spanwise directions. With the pointwise source terms-based corrections, the coupling between the two domains directly reflects the physical interaction: the global domain provides improved conditioning for the local embedded fine-mesh block whilst the local fine-mesh block provides a means to lead to an effectively improved resolution for the global domain. It follows that the improved near-wall solutions of both the embedded fine-mesh block and the coarse-mesh inner region in turn lead to improved conditioning for the global outer flow region.

The two-scale method is examined for an incompressible channel flow. Validation case studies are carried out for $Re_\tau \approx 550$, 1000 and 2000, with the mean statistics and energy spectra being compared with the corresponding full DNS data (Lee & Moser 2015; del Alamo, et al. 2004). Analyses using the Huang-Hilbert EMD method for scale decomposition and re-composition in a similar way to that of Marusic, et al. (2017), illustrate the 'foot-printing' and the 'modulation' effects in the local fine-mesh block. It is shown that the mesh-count scaling with Reynolds number can be potentially reduced from $O(Re^2)$ for conventional wall-resolved Large Eddy Simulations (LES) to $O(Re)$ for the present local wall-embedded LES. Further LES tests are conducted for $Re_\tau \approx 2000$, 4100 and 5200, demonstrating the projected mesh count gains and improved accuracy of the present method over a direct coarse-mesh solution without the two-scale source-term coupling.

Finally, some further comments should be made regarding the prospect of applying the present two-scale methodology as described to more practical applications. The seemingly restrictive feature of a channel flow is the homogeneity of the time-averaged flow in the two wall parallel directions. We intentionally make use of the simple canonical configuration to highlight the most relevant while generally applicable key difference between an unsteady field and its time-averaged counterpart. The latter is much smoother than the former, thus a source term correction based on a time-invariant averaged (instead of an instantaneous) flow would be far more readily amenable to spectral mapping efficiently and accurately in the two wall-parallel directions for wall-bounded turbulence. This should be the case for many practical wall-bounded turbulence flows where a time-averaged flow is smooth while being inhomogeneous in two wall-parallel directions. As indicated in

the introduction, the present work stems from a two-scale block-spectral method development aimed at more specific practical problems, such as surface micro-structures, micro/effusion-cooling (He, 2018; Kapsis, et al., 2020) and aerothermal analyses of multiple blade passages and rows (He, 2021), commonly subject to nonuniform flow conditions and geometries. The work presented in this chapter should provide a more fundamental while generalisable underpinning of the two-scale methodology, as motivated.

6 TRIPPING OF TURBULENT BOUNDARY LAYERS

A two-scale framework is implemented and demonstrated in the previous chapter for a canonical turbulent channel flow. The following chapters will extend the two-scale method to turbulent boundary layers. As a prerequisite to studying a TBL, it first has to be properly initiated with related issues to be studied in this chapter. In order to initiate a TBL with clearly and consistently applied inflow conditions, a physical 2-D roughness element will be numerically resolved to trip boundary layer transition.

We would like to, first of all, examine how fine the local mesh should be to properly resolve a tripping element, particularly in comparison to a typical mesh required for a scale-resolving turbulent boundary layer solution at a similar Reynolds number. Thereafter, we will investigate how those tripping-induced large-scale

disturbances behave physically compared to those large-scale coherent structures in a well-developed TBL, and more specifically, whether or not there will be any similar 'foot-printing' effect.

In this chapter, fully wall-resolved LES (WRLES) calculations on the physically tripped TBL are studied. The numerical method and case set-ups are first introduced, followed by the full LES validation against existing DNS databases (Wu & Moin 2009; Schlatter & Orlu 2010; Schlatter & Orlu 2012) and the well-established experimental correlations (Smits, et al. 1983; Chauhan et al. 2009; Monkewitz et al. 2007) and the investigation on the local resolution requirement for tripping. Thereafter, the streamwise development of TBL towards an equilibrium state and the impact of residual large-scale disturbances of the tripping are studied.

6.1 Baseline Method and Case Set-ups

A nominally canonical zero pressure gradient (ZPG) TBL flow is simulated by using the open-source CFD solver OpenFOAM. The unsteady incompressible flow equations in a flow domain $\Omega = [0, L_x] \times [0, L_y] \times [0, L_z]$ are

$$\nabla \cdot \boldsymbol{u} = 0$$

$$\frac{\partial \boldsymbol{u}}{\partial t} + (\boldsymbol{u} \cdot \nabla)\boldsymbol{u} + \frac{1}{\rho}\nabla p - \nu \nabla^2 \boldsymbol{u} = 0 \tag{6.1}$$

where $\boldsymbol{u}$ is the velocity vector, ρ is the constant density in the incompressible flow and ν is the kinematic viscosity. The pressure gradient ∇p should be nominally zero

both in the laminar and turbulent regimes. The domain lengths L_x, L_z and L_y are those in streamwise x, spanwise z and wall-normal y directions, respectively.

The fluid domain is demonstrated in Figure 6.1. The corresponding boundary conditions are as follows. The inlet velocity profile is set as constant with freestream velocity U_∞. The pressure gradient is set as zero at the outlet. The periodic boundary conditions are applied to the spanwise directions. The upper boundary is a slip wall mimicking the ideally infinite wall-normal height. The lower boundary is the no-slip wall exerting wall shear stress on the flow. The domain length L_x is designed to reach the targeted highest Reynolds number $Re_\theta \approx 1000$, where Re_θ is the Reynolds number based on the freestream velocity U_∞, the kinematic viscosity ν and the momentum thickness θ. The domain height is ensured to contain approximately 7 boundary layer thicknesses δ at the outlet. The spanwise domain size $L_z \sim 0.5L_y$ should be large enough to contain the largest scale spanwise structures. A preliminary sensitivity study with doubled L_z has been carried out and shows negligible differences. The overall domain covers Re_x from 0 to 7×10^5, which is based on the freestream velocity U_∞, the kinematic viscosity ν and the streamwise location x.

The flow equations are discretised in a finite volume scheme, with a second-order central difference scheme in space. The time advancement is achieved by a second-order Crank Nicolson scheme. A constant time-step is taken in keeping the maximum Courant numbers below 0.5. The pressure-implicit splitting operators (PISO) algorithm is used for solving the incompressible flow field. In the present calculations, no explicit sub-grid model is involved. All scales are directly resolved without any turbulence models. The simulations are therefore effectively implicit

LES where the sub-grid scales are dampened only by numerical dissipations. The simulations are run for a sufficiently long time to reach a statistically steady state when the mean statistics differences are confined within 1%. All the statistics to be reported are time-averaged for at least ten eddy turnover times δ/u_τ, where δ here is the boundary layer thickness at the exit and u_τ is the wall shear velocity there. The reported statistics are also spatially averaged along the homogeneous spanwise direction.

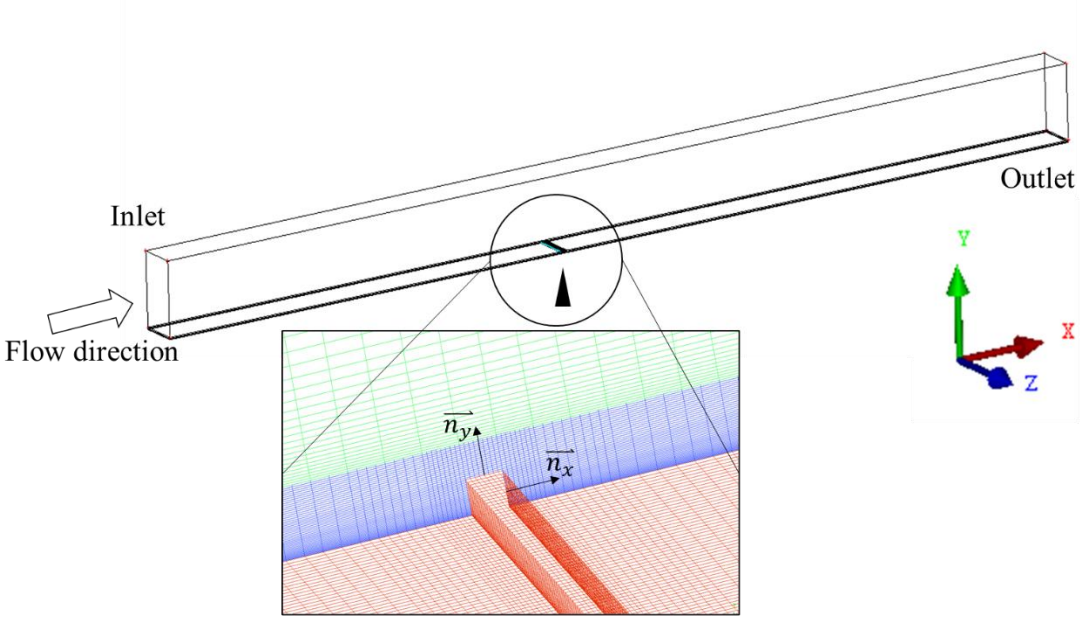


Figure 6.1. **Schematic of the computational domain. The black cone indicates the trip location, with a close-up view of the local mesh.**

The tripping element covers the entire span (L_z). The element height is set to be $\sim 0.78\delta^*$ suggested in the experimental study by Dyden (1959), where δ^* is the displacement thickness at the tripping location based on the Blasius laminar boundary layer solution. The streamwise length of the tripping element is the size of outer mesh spacing and roughly equals the element height. The element length thus

is effectively less than 0.3% of the distance from the inlet to the trip and roughly 0.2% of the distance from the trip to the outlet.

The inner (coloured blue in Figure 6.1) and outer (coloured green in Figure 6.1) meshes are connected by a wall-parallel interface at a wall-normal distance y_s. For simplicity, the superscript '+' denotes values normalised by shear velocity u_τ and viscosity ν. The inner-outer mesh interface is located at roughly the beginning of the log region in the y direction, which is around $y_s^+ \approx 70$ at $Re_\theta \approx 1000$. Given that the inner and outer mesh have different node distributions, there should be hanging nodes at the mesh interface. The interface is treated as the non-conforming arbitrary mesh interface (AMI) patches based on the Galerkin projection (Farrell & Maddison 2011) for conservation and instantaneous flow field interpolation.

The mesh resolutions of different cases are shown in Table 6.1. Note that the wall-normal mesh resolution is kept the same in all cases, gradually stretching from $\Delta y_w^+ \sim 0.5$ at the lower solid wall to the upper boundary. There are approximately 10 mesh points below $y^+ = 5$, 55 points below y_s^+ and 80 points located within the boundary layer at $Re_\theta \approx 1000$. Following Moin & Jimenez (1997) and Jimenez & Moser (2000), the near-wall mesh of WRLES should be as fine as that of DNS. Uniformly distributed mesh is used in both spanwise and streamwise directions as the baseline mesh.

Three cases, namely '*Base-x40z30*', '*Base-x20z15*' and '*Base-x10z7*', are set up with quadrupole refinement in both x and z directions. Note that resolutions in wall units (inner and outer mesh resolution in Table 6.1) are calculated based on wall shear velocity u_τ at $Re_\theta \approx 1000$. Thereafter, the investigation on the sensitivity of local mesh refinement around the trip is carried out with the three cases with locally

refined mesh around the trip: '*RFtrip-x40z30*', '*RFtrip-x20z15*' and '*RFtrip-x10z7*'. The trip is refined as indicated in Figure 6.1 with the mesh grids clustered around the trip for *RFtrip-x20z15* as an example. The resolutions at the trip itself are calculated using local time-averaged u_τ at each corresponding trip surface based on the first mesh cell size in the wall normal directions $\boldsymbol{n}_x$ and $\boldsymbol{n}_y$ (Figure 6.1).

Table 6.1 Details of mesh resolution of the cases simulated

Case name	Inner mesh resolution	Outer mesh resolution	Resolution at trip	Descriptions
Base-x10z7	Δx^+~10, Δz^+~7	Δx^+~40, Δz^+~30	$\Delta n_x{}^+$~2, $\Delta n_y{}^+$~1.4	Base mesh, no trip-mesh refinement
Base-x20z15	Δx^+~20, Δz^+~15		$\Delta n_x{}^+$~5.2, $\Delta n_y{}^+$~2.3	
Base-x40z30	Δx^+~40, Δz^+~30		$\Delta n_x{}^+$~17.3, $\Delta n_y{}^+$~4.3	
RFtrip-x10z7	Δx^+~10, Δz^+~7		$\Delta n_x{}^+$~1.7, $\Delta n_y{}^+$~1.3	Refined mesh at trip
RFtrip-x20z15	Δx^+~20, Δz^+~15		$\Delta n_x{}^+$~1.7, $\Delta n_y{}^+$~1.3	
RFtrip-x40z30	Δx^+~40, Δz^+~30		$\Delta n_x{}^+$~1.7, $\Delta n_y{}^+$~1.3	

6.2 LES Validation and Resolution Requirement for Tripping

For the cases considered, the streamwise pressure gradient should be nominally zero in a zero-pressure-gradient (ZPG) TBL flow, but this is practically almost impossible to achieve either experimentally or numerically as discussed in Wu & Moin (2009). The indicators of the pressure gradient magnitude in Wu & Moin (2009) are used here to evaluate the credibility of the simulated ZPG TBL: $\beta = (\delta^*/\tau_w)(\partial\overline{p}/\partial x)$; $-20P^+ = -20(\nu/\rho u_\tau^3)(\partial\overline{p}/\partial x)$, where $\overline{p}$ is the time-averaged pressure, τ_w denotes the wall shear stress and ρ is the constant fluid density in the incompressible flow. The averaged values in the fully turbulent regime are compared in Table 6.2. The results are in the same order of magnitude as that in Wu & Moin (2009) and an order of magnitude lower than that in Spalart & Watmuff (1993) for assurance.

Table 6.2 Averaged pressure gradient at approximately $y \sim L_y/8$

	$\|\boldsymbol{\beta}\|$	-20$\boldsymbol{P^+}$
RFtrip-x10z7	~0.03	~0.01
Wu & Moin (2009)	~0.02	~0.01
Spalart & Watmuff (1993)	~0.4	~0.1

The calculated time-averaged skin friction coefficients C_f as the function of Reynolds number based on momentum thickness Re_θ is shown in Figure 6.2. All cases overlap in the laminar regime. In the turbulent regime, as the inner mesh is quadropoly refined in streamwise and spanwise directions, a clear mesh-convergence

can be observed. It can also be observed that the transition begins at $Re_\theta \approx 250$ - 300 and the flow becomes turbulent at $Re_\theta \approx 450$ after the trip. The local refinement at the trip slightly improves the results downstream close to the trip, shown by the comparison between *Base-x20z15* (Figure 6.2a) and *RFTrip-x20z15* (Figure 6.2b). As also demonstrated in Figure 6.2(a), the calculation *Base-x10z7* without any local refinement resolves the trip reasonably well by the fine inner DNS mesh on its own. The results match up well with the fitted curve based on experimental data by Smits, et al. (1983). Note that the results in the transition regions (covering the tripping and downstream recirculation regions) are not shown in this section as the calculated Re_θ for this region with reverse flows would be hardly meaningful.

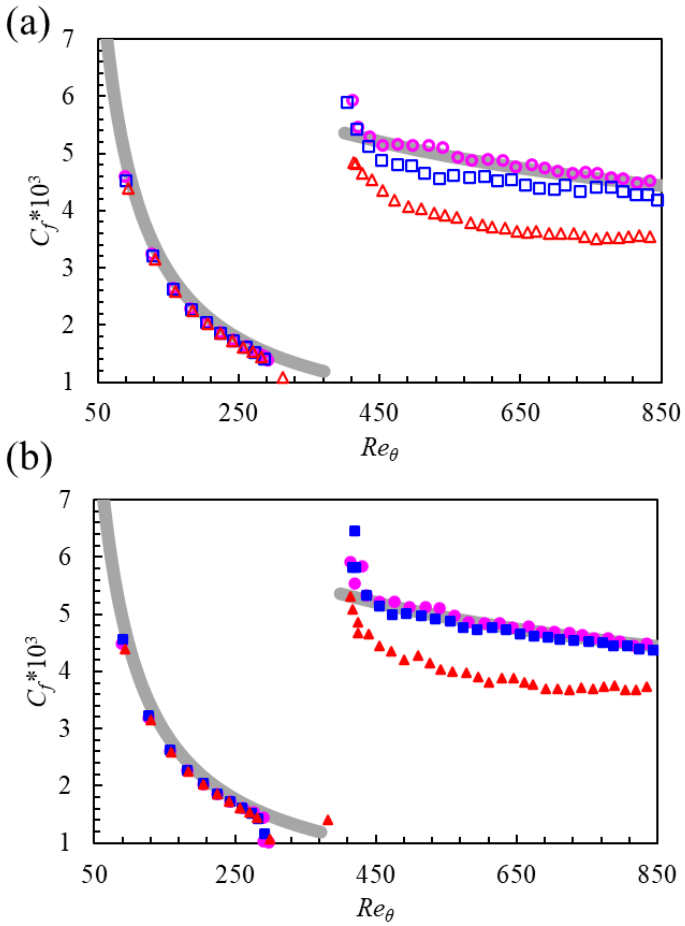


Figure 6.2. **Friction coefficients C_f as functions of Re_θ along the streamwise direction compared with Blasius laminar profile and the correlated curve for the turbulent regime (solid grey lines '—') by Smits, et al. (1983). (a) for the base meshes: *Base-x10z7*: open magenta circles ○; *Base-x20z15*: open blue squares □; *Base-x40z30*: open red triangles Δ. (b) for the trip-refined meshes: *RFTrip-x10z7*: solid magenta circles ●; *RFtrip-x20z15*: solid blue squares ■; *RFtrip-x40z30*: solid red triangles ▲. Note that not all data are shown for clarity.**

More sensitive indicators, the ratio between the boundary layer thickness and the displacement or momentum thickness, δ/δ^* and δ/θ, as introduced

(Schlatter & Orlu 2010) are also presented for a closer examination of the local trip mesh refinement. For the two cases *Base-x20z15* and *RFtrip-x20z15*, the indicators converge at approximately $Re_\theta \approx 700$, as shown in Figure 6.3. There is little difference at a higher Reynolds number further downstream and both cases asymptotically converge to the correlated experimental data by Chauhan, et al. (2009).

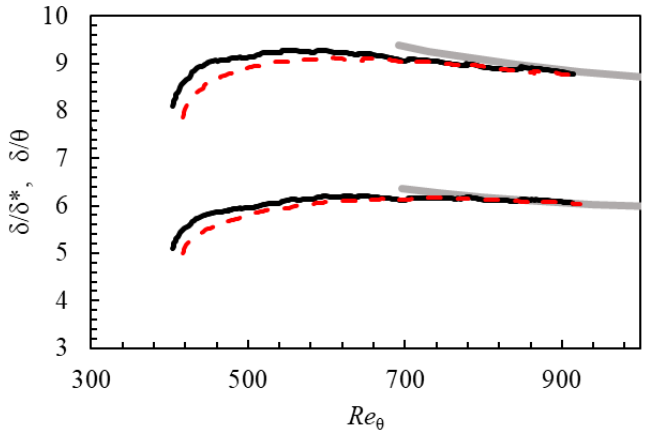


Figure 6.3. **Indicators δ/δ^* and δ/θ compared with the correlated curves by Chauhan et al. (2009) shown in solid grey lines '—'. The present results are shown as *RFTrip-x20z7* (solid black lines '—') and *Base-x20z7* (red dash lines '— —').**

The streamwise and spanwise grid spacings of *Base-x10z7* seems to be the upper limits of the mesh coarseness capable of properly resolving the roughness element with local Δn_x^+ lying within the viscous sublayer (see Table 6.1). Thus, DNS base meshes as fine as *Base-x10z7* should be sufficient on its own without further local refinement in resolving the trip. On the other hand, if introducing a local refinement, the extra mesh count also tends to be marginally small if the base mesh is reasonably fine. In the case of *Base-x20z15*, the local refinement around the trip

(*RFtrip-x20z15*) corresponds to only about 2% extra mesh count required for a much-improved solution of the tripping. Thus, the present approach to directly resolving the physical trip element does not appear to request a significant amount of additional mesh count, and the simple trip device seems to be capable of generating fully TBL effectively in a relatively short distance downstream.

Figure 6.4 shows the shape factor, $H_{12} = \delta^*/\theta$ as the function of Re_θ for the boundary layer development. The results from the case *RFtrip-x10z7* match up with the fitted curve of TBL development by Monkewitz et al. (2007) in the turbulent regime with the shape factor H_{12} asymptotically approaching $H_{12} \approx 1.4$. Figure 6.5 shows that the equivalent shear Reynolds number (δ^+) based on local boundary layer thickness and shear velocity for case *RFTrip-x10z7*, matching up well in the turbulent regime with the fitted curve on TBL development (Schlatter & Orlu, 2010).

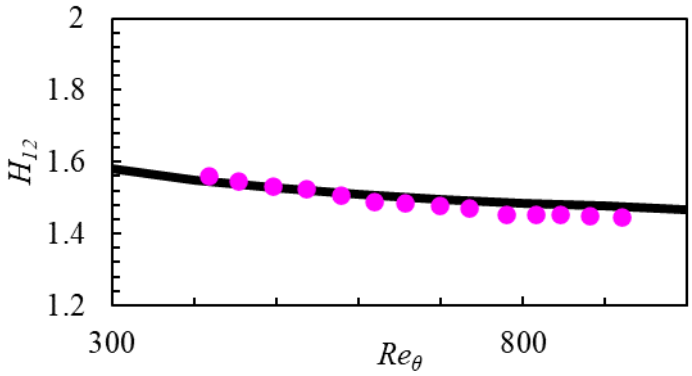


Figure 6.4. **The shape factor H_{12} as functions of Re_θ compared with fitted curve in the black solid line '—' from Monkewitz et al. (2007). *RFTrip-x10z7*: solid magenta circles ●. Note that not all data are shown for clarity.**

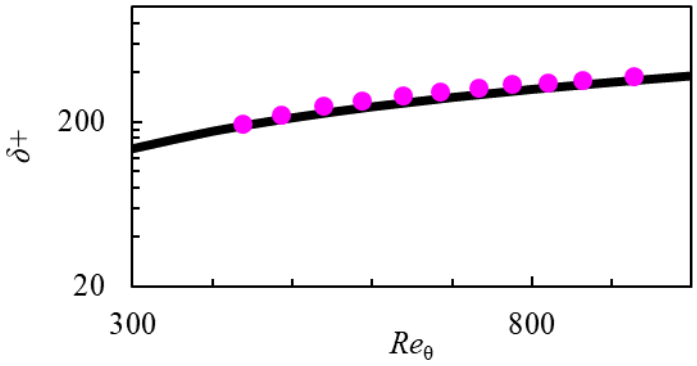


Figure 6.5. **The development of boundary layer thickness δ^+ as functions of Re_θ compared with the fitted curve in the black solid line '—' by Schlatter and Orlu (2010). *RFTrip-x10z7*: solid magenta circles ●. Note that not all data are shown for clarity.**

Figure 6.6 presents the time mean velocity profiles, the root mean squared ('*rms*') velocity fluctuations and the Reynolds stresses (ensemble averaged values are denoted as '$<\cdot>$') as a function of wall-normal distances y^+. Results at two Reynolds numbers are compared with the published DNS results. The present results of *RFtrip-x10z7* match up with the DNS data well at $Re_\theta \approx 1000$, better than that at $Re_\theta \approx 670$ where the flow could presumably be fully turbulent but not yet fully developed. Interestingly, the difference between the two DNS data sets at $Re_\theta \approx 670$ is also nontrivial, probably due to different ways of initiating TBL. In addition, we see that outer flows are quiet well resolved by the coarser mesh (Table 6.1) with the Reynolds stresses matching up with the DNS data at $Re_\theta \approx 1000$.

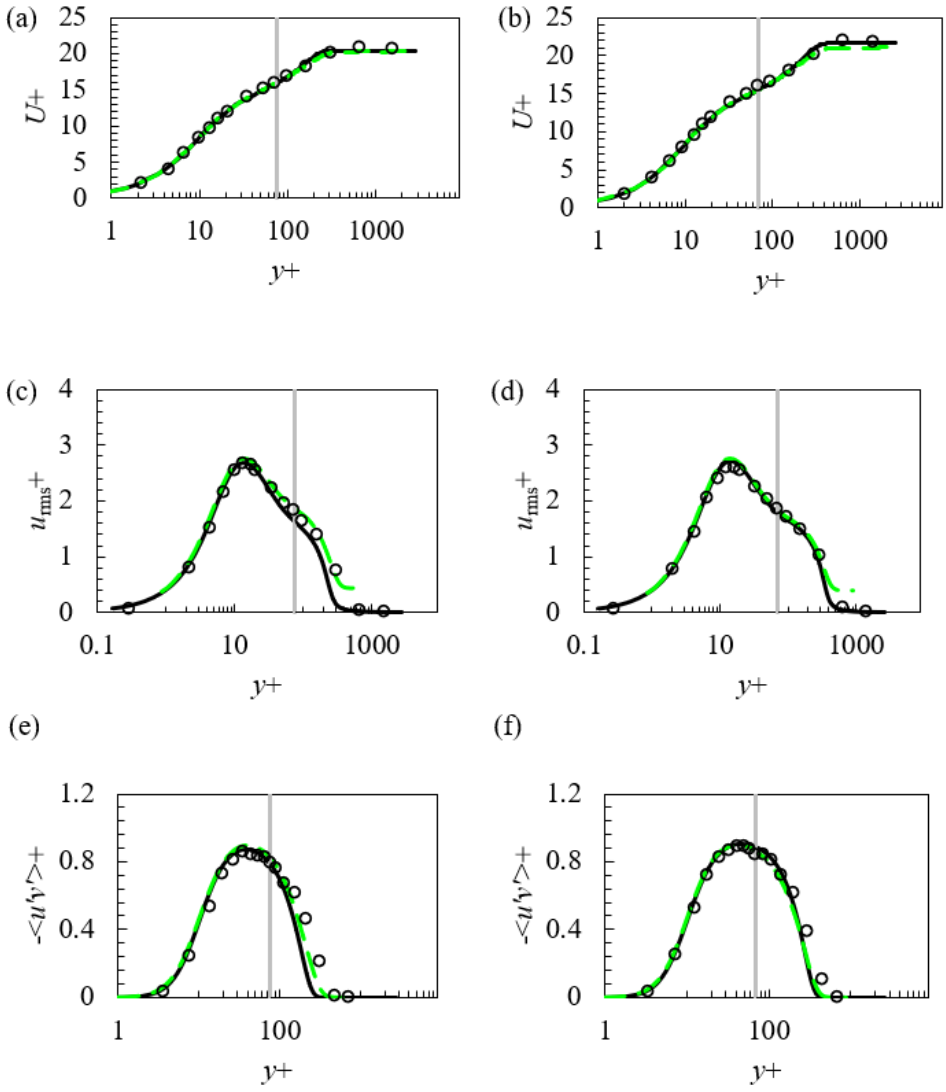


Figure 6.6. **Mean statistics with respect to wall-normal distances y^+. (a, b) Mean velocity profiles. (c, d) Streamwise velocity fluctuations. (e, f) Reynolds shear stresses. Results are at two Reynolds numbers: (a, c, e) $Re_\theta \approx 670$ and (b, d, f) $Re_\theta \approx 960$. The DNS data are shown at the corresponding Re_θ: Schlatter and Orlu (2012) in solid black lines '—'; Wu & Moin (2009) in green dash lines '— —'. The present results are in open black circles ○. The grey lines '—' mark the inner-outer mesh interfaces. Note that not all data are shown for clarity.**

6.3 Evolution towards Equilibrium State

An instantaneous view of vortical flow structures from the trip to the fully turbulent boundary layer downstream is illustrated in Figure 6.7. The structures are visualised in terms of the Q-criteria (Hunt, et al. 1988; Jeong & Hussain 1995) for case *RFtrip-x10z7*. The laminar boundary layer is buffeted by the 2-D step with vortices shed downstream from the top surface, similar to the roughness-induced bypass transition in Rao, et al. (2014). The roll-up of vortices becomes spanwise non-uniform and breaks down very soon downstream similar to that observed by Brinkerhoff & Yaras (2011). The instability develops downstream as the breakdown of spanwise vortices into 3-dimensional turbulent structures. From $Re_\theta \approx 350$ to $Re_\theta \approx 420$, when the new boundary layer is formed after the reattachment, the hairpin vortices (Adrian, et al. 2000) start to emerge. Note that a natural transition triggered by Tollmien-Schlichting (TS) waves follows the classical route from initial linear primary disturbances to secondary instabilities (Sayadi, et al. 2013), where the formation of linear Λ-shape vortices should be spatially long. These features are obviously bypassed in the present situation.

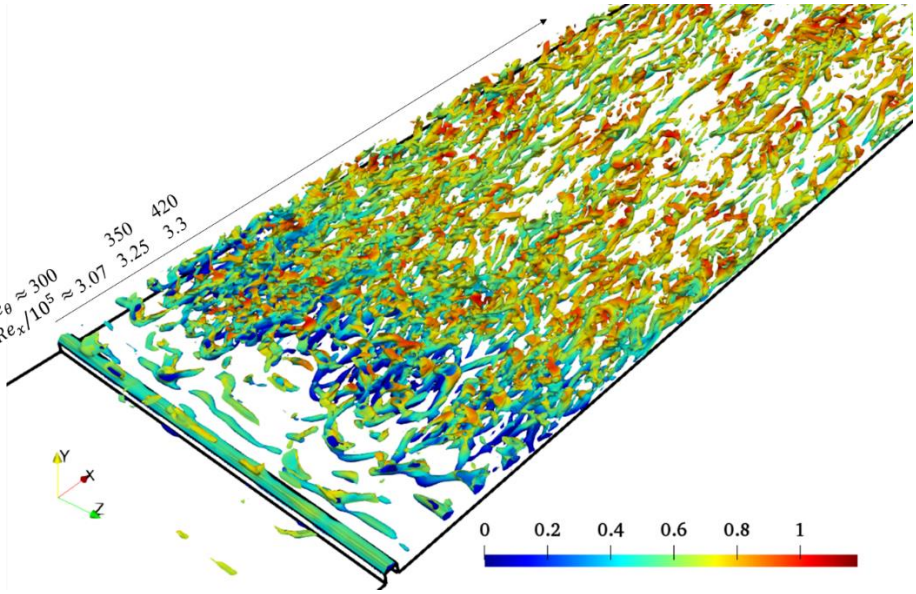


Figure 6.7. **Iso-surfaces of the Q-criterion in the inner region with refined mesh. The coloured contour levels demonstrate the scaled velocity U/U_∞.**

Figure 6.8 shows the comparison between the present calculation (*RFtrip-x10z7*), the T-S wave associated natural transition (*TS*), and the artificial-trip-induced transition (*OP-KTH*) in terms of the indicators δ/δ^* and δ/θ. An obviously shorter development length of the present calculation can be observed compared with the natural transition (*TS*). The synthetic volume force tripping with 'optimally' tuned parameters (*OP-KTH*) enforces a fully developed turbulent regime right at tripping resulting in nearly straight lines which are distinctively different from the others.

It may be more informative that the results as shown in Figure 6.8 are categorised into two groups in terms of how each solution approaches asymptotically to eventually almost constant values (indicative of an equilibrium state), approximately 8.5 for δ/θ and 5.8 for δ/δ^*respectively. The first group consists of those physical transition routes: the natural transition (*TS*), the trip experimentally

implemented (Chaunhan et al. 2009) or numerically simulated (*RFtrip-x10z7*). The results of this group first overshoot and then decrease gradually to approach equilibrium. The initial overshoot indicates a relatively thicker boundary thickness due to the outflow region being disturbed by large-scale disturbances, which have relatively a small influence on the inner part of the large velocity deficit more responsible for contributing to the two integral parameters, δ^* and θ. However, in the second group, the optimally triggered one (*OP-KTH)*, the two parameters δ/δ^* and δ/θ approach the final state rather differently, both increasing with Re_θ monotonically. The similarity among those physically tripped turbulent flows in approaching the final equilibrium state draws further attention to the characteristics of a post-transition non-equilibrium TBL and their influence, more specifically, on the near-wall part.

Now, we use first the present results to elaborate on the overall tripping process from the viewpoint of energy production and dissipation. Then we will examine the characteristics and influence of those large-scale tripping-induced large-scale disturbances through modal analyses.

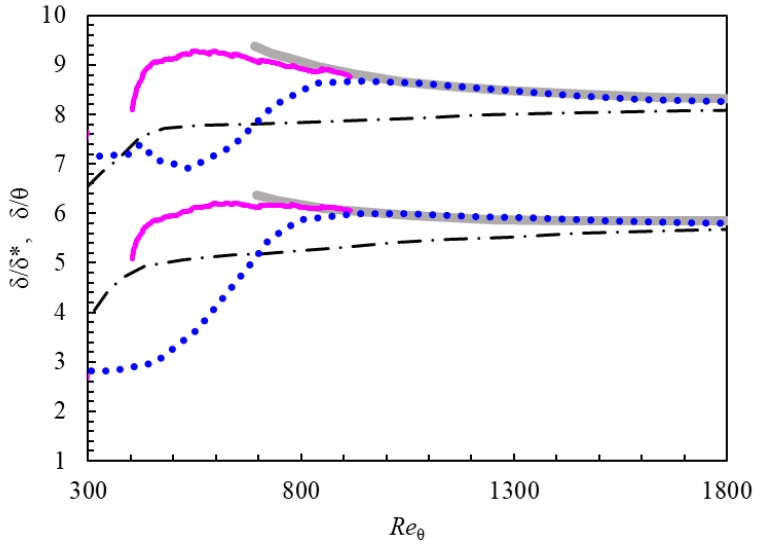


Figure 6.8. **Indicators δ/δ^* and δ/θ compared with the experimentally correlated curves by Chauhan et al. (2009) shown in solid grey lines '—'. Results of the tuned 'optimal' tripping in Schlatter and Orlu (2012) are shown as '*OP-KTH*' (dash-dot black lines '— · —') together with the natural TS-wave transition, marked as '*TS*' (blue dots '▪'). The results of the present calculations (*RFTrip-x10z7*) are shown in solid magenta lines '—'.**

We introduce the dissipation coefficient C_d for time-averaged incompressible flow (e.g., Wheeler et al. 2018) as

$$C_d = \epsilon + Pr = \frac{1}{U_\infty^3}\int_0^\delta \nu\left(\frac{\partial U_i}{\partial x_i}\right)^2 dy + \left(-\frac{1}{U_\infty^3}\int_0^\delta \overline{u_i u_j}\frac{\partial U_i}{\partial x_j} dy\right) \tag{6.2}$$

where the dissipation coefficient C_d represents the loss of mean kinetic energy as a combination of the viscous dissipation of the mean flow (ϵ) and the production of turbulence kinetic energy (Pr) in the spatially evolving boundary layer flow.

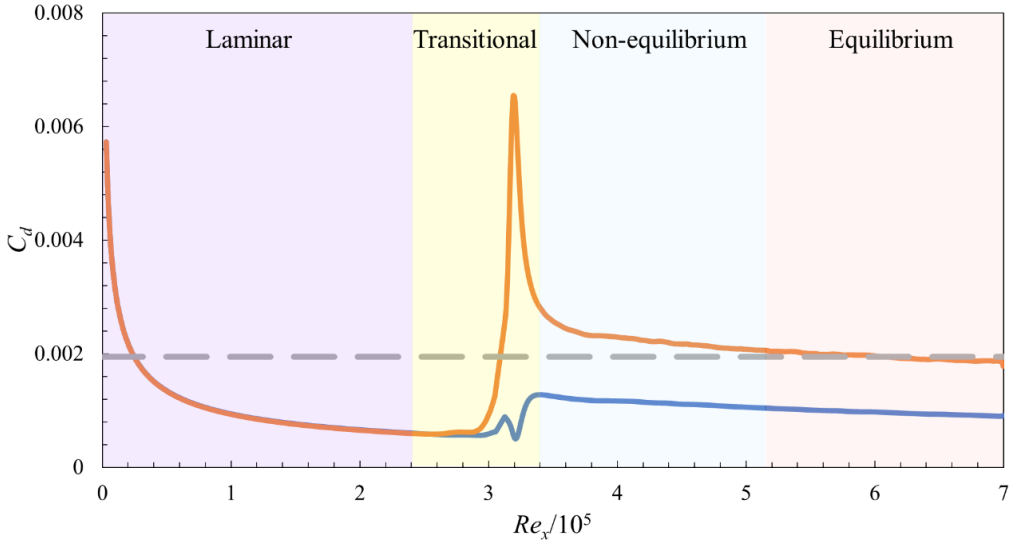


Figure 6.9. **The dissipation coefficient C_d as functions of Re_x, categorised as four stages: laminar, transitional, non-equilibrium and equilibrium. The blue solid line '—' depicts the local dissipation ϵ, while the orange solid line '—' depicts the dissipation coefficient $C_d = \epsilon + Pr$. The grey dashed line '— —' indicates $C_d \approx 0.002$.**

The full wall-resolved LES solutions ('*RFTrip-x10z7*' in section 6.2) are processed based on equation (6.2), as shown in Figure 6.9. The entire route of the boundary layer development could be categorised into four stages: laminar, transitional, non-equilibrium and equilibrium. Wheeler, et al. (2018) show that C_d which is initially very high at the transitional stage, plunges to the normal level for turbulent boundary layers, and approaches asymptotically to a value of 0.002. A similar process can be observed in Figure 6.9. Initially, in the laminar regime, there is zero turbulence energy production. Then it takes a journey into a non-equilibrium stage where the transition completes, and the boundary layer becomes fully turbulent yet not fully developed. The non-equilibrium status is attributed to the fact that the turbulence production rate reacts much faster in transition than the dissipation rate,

resulting in an imbalance (Wheeler, et al. 2018). The turbulent boundary layer gradually develops toward an equilibrium state where $Re_\theta \approx 800$ ($Re_x/10^5 \approx 6$) with $C_d \approx 0.002$ ($\epsilon \approx 0.001$ and $Pr \approx 0.001$).

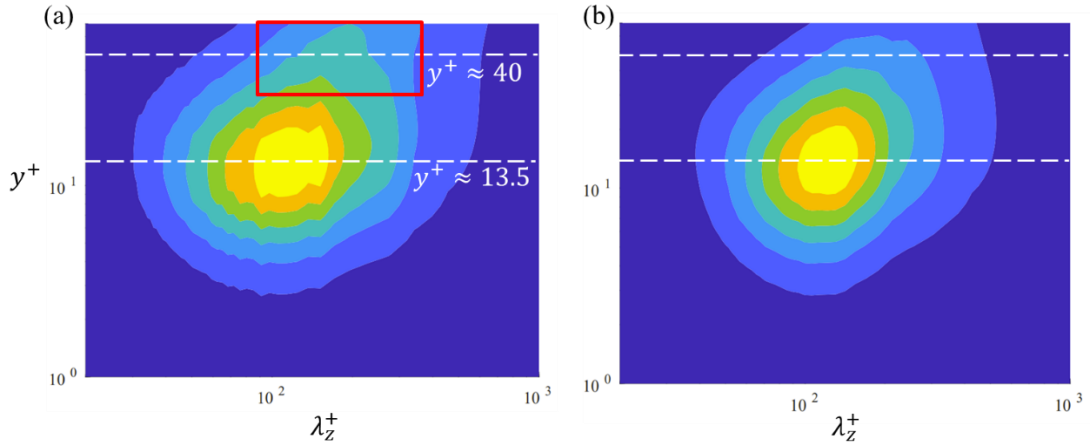


Figure 6.10. **One-dimensional pre-multiplied energy spectra generated from (a) present calculation in the non-equilibrium TBL, and (b) DNS channel flow data at approximately the same $Re_\tau \approx 190$ (Lee & Moser 2015). The contour levels are from 1.5 to 4 with an interval of 0.5. The white dashed lines mark the two wall-normal locations: $y^+ \approx 40$ (roughly $y \approx \Delta_{y,trip}$ locally) and $y^+ \approx 13.5$. The solid red box highlights the tripping-induced excessive energy.**

Looking at the post-trip non-equilibrium turbulent region (from $Re_x/10^5 \approx 3.4 - 3.8$) more closely, we apply the Fast Fourier Transfer to obtain the one-dimensional pre-multiplied energy spectra for this region as shown in Figure 6.10(a). Notice that the wall shear Reynolds number Re_τ in the middle of the region is approximately 190. The present results are compared with the DNS data at $Re_\tau \approx 192$ for the canonical channel flow (Lee & Moser 2015) as shown in Figure 6.10(b). An energy overshoot of the present results (Figure 10a) can be clearly seen at $y = \Delta_{y,trip}$ ($y^+ \approx 40$). This location is in the log-region, so we label it as an outer flow

region in contrast to the near-wall region below the buffer layer. Large-scale disturbances in the outer flow region of a tripped turbulent boundary layer are similarly observed by Marusic, et al. (2015).

Given the presence of large-scale disturbances in the outer flow region, we now would like to know how persistent downstream they are and whether they have a significant influence on the near-wall region. We will first look at the power spectra density (PSD) at different wall-normal locations in different streamwise stations. The PSD of the flow velocity component is calculated using Welch's method with the Hann window (Welch 1967) to reduce finite sampling effects. The dimensionless frequencies are in the form of Strouhal number $St = fL/U$, where the characteristic length and velocity are the trip height $\Delta_{y,trip}$ and the freestream velocity, respectively.

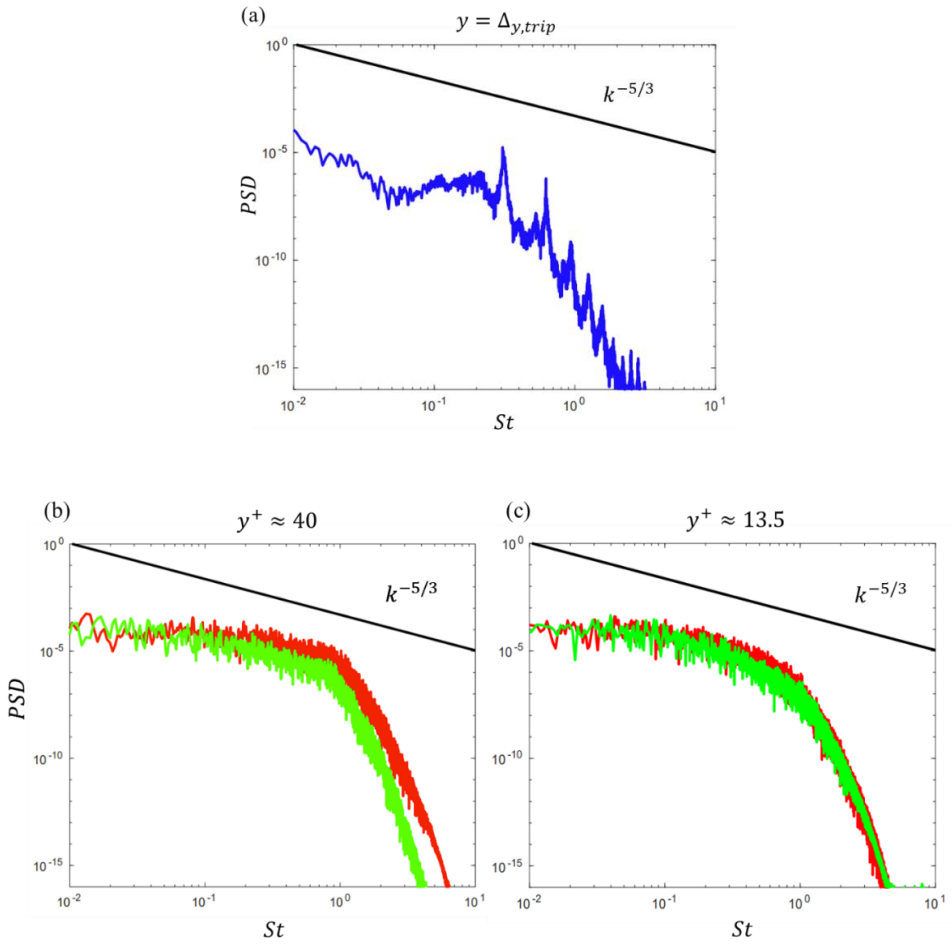


Figure 6.11. **The power spectral density (PSD) in relation to the non-dimensional frequencies at different streamwise stations: right after the trip '—'; $Re_x/10^5 \approx 3.6$ '—'; and $Re_x/10^5 \approx 7$ '—'. The spectra are plotted at different wall-normal locations: (a) $y = \Delta_{y,trip}$; (b) $y = \Delta_{y,trip}$ ($y^+ \approx 40$ at $Re_x/10^5 \approx 3.6$); and (c) $y^+ \approx 13.5$.**

Figure 6.11 shows the PSD at different streamwise and wall-normal locations. For the outer flow location taken at the trip height, clear vortex shedding features can be observed in Figure 6.11(a) right after the trip ($Re_x/10^5 \approx 3.1$, see Figure 6.9 for the physical view). The outer flow spectra become more comparable to a conventional turbulent one further downstream (Figure 6.11b), but still, the residual

large-scale disturbances are detectable, e.g., from the non-smoothness of spectrum around $St \approx 1$ even at $Re_x/10^5 \approx 7$. The outer spectrum in Figure 6.11(b) at $Re_x/10^5 \approx 3.6$ at the non-equilibrium stage experiences an overshot in energy at $St \approx 1$. In contrast, at the inner location $y^+ \approx 13.5$, shown in Figure 6.11(c), the flow has developed into a typical turbulent spectrum shortly after the trip, even at $Re_x/10^5 \approx 3.6$. The excessive energy generated at the trip height seemingly affects the outer flow region more significantly than the inner near-wall region. This is in line with the prevalent observation that the outer region requires a longer evolution distance than the inner one to reach a full equilibrium state (Devenport & Lowe 2022).

6.4 Evolution and Impact of Large-scale Disturbances

To further examine the streamwise evolution of large-scale trip-induced disturbances and their potential risk in influencing near-wall turbulence, we carry out modal analyses. Firstly, the empirical mode decomposition (EMD) method (Huang et al. 1998) is implemented to identify if large-scale structures would correlate between the outer and inner regions. The same procedure of the EMD method as in chapter 5 (section 5.3.3) is applied to the snapshot plane cuts of the instantaneous flow field, as shown in Figure 6.12, Figure 6.13 and Figure 6.14.

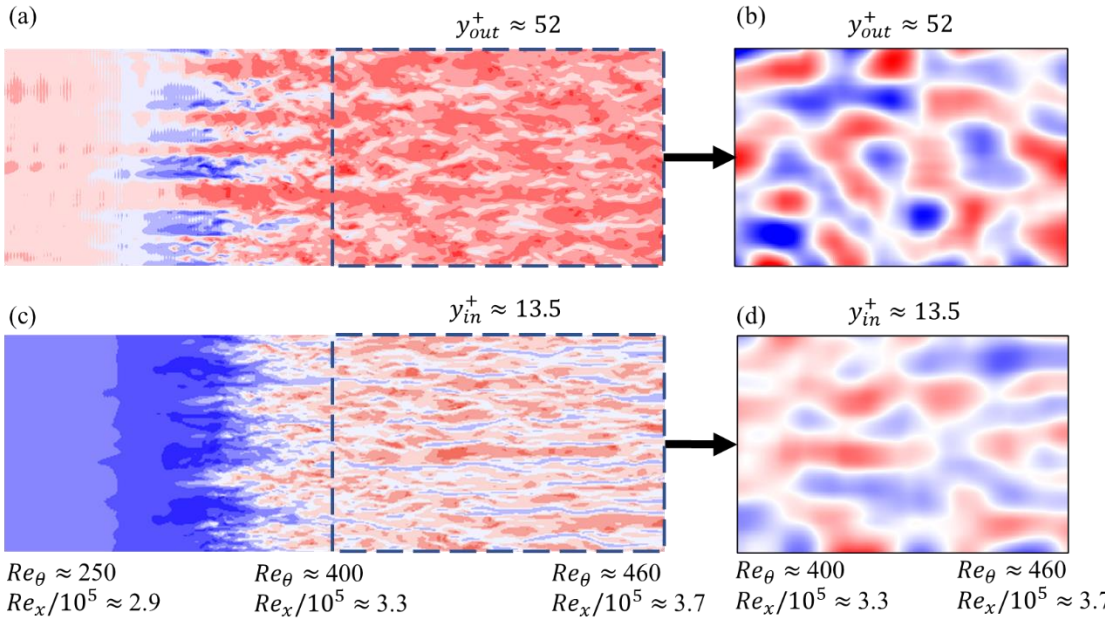


Figure 6.12. **The original and filtered field around the tripping region. (a, c) The instantaneous velocities on cut planes at two wall-normal locations: $y^+_{out} \approx 52$ and $y^+_{in} \approx 13.5$, respectively. (b, d) The corresponding large-scale structures retained from the regions marked by black dash boxes in (a) and (c) respectively. The contour maximum values in (b, d) are set as $\pm 2.74 u_\tau$.**

As seen in Figure 6.12, there is little correlation between the outer and inner large-scale structures filtered from the instantaneous velocity flow fields from the transitional region to $Re_\theta \approx 460$ with the Pearson correlation coefficient being about 0.21. Reaching the end of the domain at a relatively higher Re (Figure 6.13), we can observe that large scales start to show up more clearly in the near-wall region (Figure 6.13d), the correlation between the non-streaky large scales is still quite low. The correlation coefficient is calculated to be approximately 0.33 between Figure 6.13(b) and (d).

For a direct contrast to Figure 6.12 and Figure 6.13, Figure 6.14 illustrates strong 'foot-prints' as seen in the canonical channel flow at a high Re. With the periodic boundary conditions applied in the streamwise direction, the flow is regarded as fully developed reaching an equilibrium state. The outer and inner large scales appear not only as long streaky structures but also highly correlated in both shapes and magnitudes of those large-scale disturbances, especially when comparing Figure 6.14(b) with Figure 6.14(d) where the correlation coefficient is calculated to be approximately 0.82.

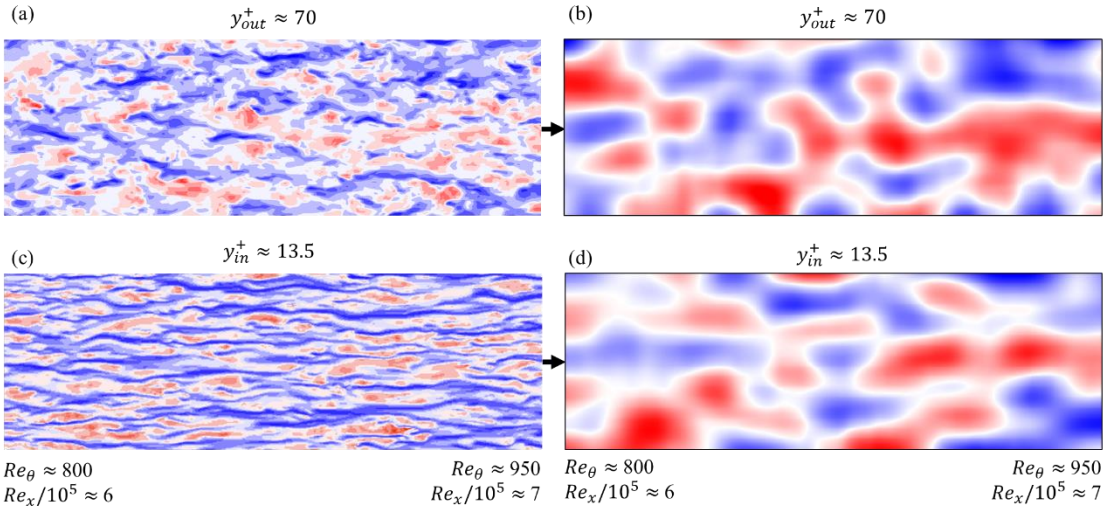


Figure 6.13. **The original and filtered field from $Re_\theta \approx 800$ to 950. (a, c) The instantaneous velocity field from $Re_\theta \approx 800$ to 950 at two wall-normal locations: $y^+_{out} \approx 70$ and $y^+_{in} \approx 13.5$, respectively. (b, d) The large-scale structures retained from (a) and (c) respectively. The contour maximum values in (b, d) are set as $\pm 2.4u_\tau$.**

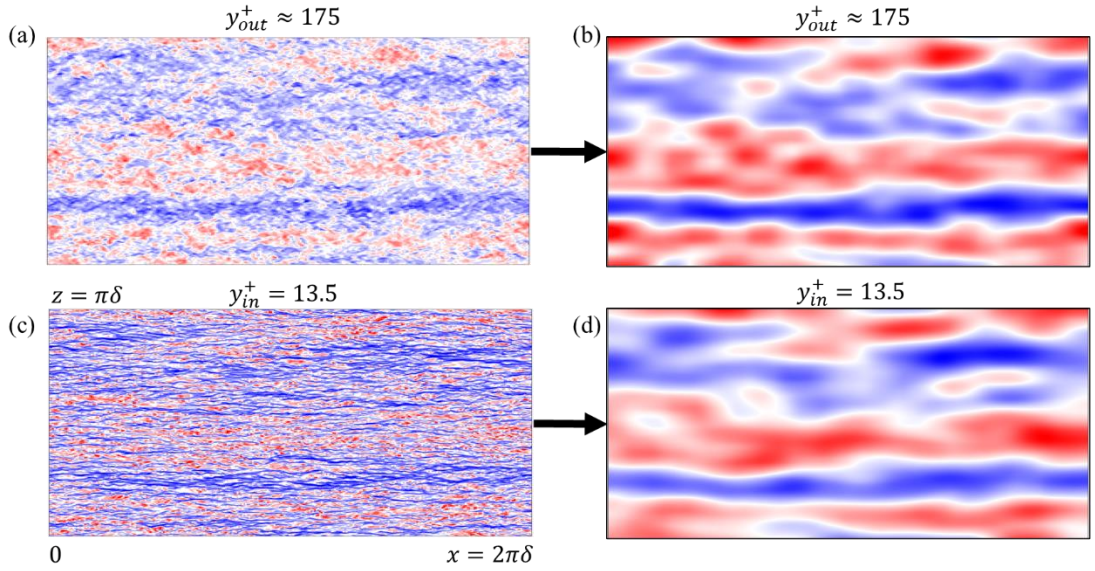


Figure 6.14. **Proper 'foot-printing' evidence at high Re in the fully developed channel flow. (a, c) The instantaneous velocity field from $Re_\tau \approx 2000$ at two wall-normal locations: $y^+_{out} \approx 3.9\sqrt{Re_\tau} \approx 175$ and $y^+_{in} \approx 13.5$, respectively. (b, d) the large-scale structures retained from (a) and (c) respectively. The inner and outer plane locations share the same y^+ values with Marusic, Mathis & Hutchins (2010).**

The EMD analysis above provides a relatively straightforward way to identify and correlate distinctive large scales between two snapshots. To gain more systematic insights into those dynamically active temporal and spatial flow structures, we also carry out some analyses using the Dynamic Mode Decomposition (DMD) method (Schmid, 2010).

A snapshot matrix is constructed first when applying the DMD method as

$$\boldsymbol{X}_0^{n-1} = [x_0, x_1, \dots, x_{n-1}] \in R^{m\times(n-1)}, \boldsymbol{X}_1^{n} = [x_1, x_2, \dots, x_n] \in R^{m\times(n-1)} \tag{6.3}$$

where in the present case, x_i represents the instantaneous streamwise velocity field, consisting of m data points at time $t = i\Delta t$, supposing each sampling interval is set to be Δt. The matrix $\boldsymbol{X}_0^{n-1}$ effectively contains snapshots from $i = 0$ to $n-1$. Imagine there is a linear operator between two consecutive snapshots:

$$\boldsymbol{X}_1^n = \boldsymbol{A}\boldsymbol{X}_0^{n-1} \tag{6.4}$$

where $\boldsymbol{A}$ is the dynamics matrix and can be obtained by $\boldsymbol{A} = \boldsymbol{X}_1^n(\boldsymbol{X}_0^{n-1})^{-1}$, where $[\cdot]^{-1}$ denotes the pseudo-inverse operator. Given that the size of $\boldsymbol{X}$ is usually tremendously huge, the singular value decomposition is introduced (Taira, et al. 2017) to reduce the rank of $\boldsymbol{A}$ to be r. The j-th eigenvalue and eigenvector of $\boldsymbol{A}$ are λ_j and $\boldsymbol{\Phi}_j$, respectively. The dominant modes as the eigenvector and the corresponding frequency calculated by the eigenvalue can thereafter be picked up as the representatives of the raw field to reveal the dominant flow features of the original flow field.

To reconstruct the field, the amplitude of each mode should be first determined as $\boldsymbol{b} = [b_1, b_2, \dots, b_r]$. The i-th snapshot at time t is then given by

$$\bar{\bar{x}}_i = \sum_{j=0}^{r} \lambda_j^i b_j \boldsymbol{\Phi}_j, i = t/\Delta t \tag{6.5}$$

The loss function is introduced for comparison as the difference between the reconstructed field $(\overline{\overline{\boldsymbol{X}_0^{n-1}}})_{DMD}$ and the original field $\boldsymbol{X}_0^{n-1}$ accumulated from $t = 0$ to $T = (n-1)\Delta t$.

$$loss = \left\| \boldsymbol{X}_0^{n-1} - (\overline{\overline{\boldsymbol{X}_0^{n-1}}})_{DMD} \right\|^2 / \|\boldsymbol{X}_0^{n-1}\|^2 \tag{6.6}$$

For verification purposes, the DMD method is first applied to the present full WRLES case. The aforementioned procedure is applied to $n = 201$ snapshots extracted from the $x - y$ plane in the middle of the domain. The streamwise range is chosen to be right downstream of the trip ($Re_x = 3.1 - 3.6 \times 10^5$). The convergence on reconstruction is shown in Figure 6.15 via the loss of accuracy as a function of the number of modes *N* retained. The loss could be less than 5% when *N* is larger than 120.

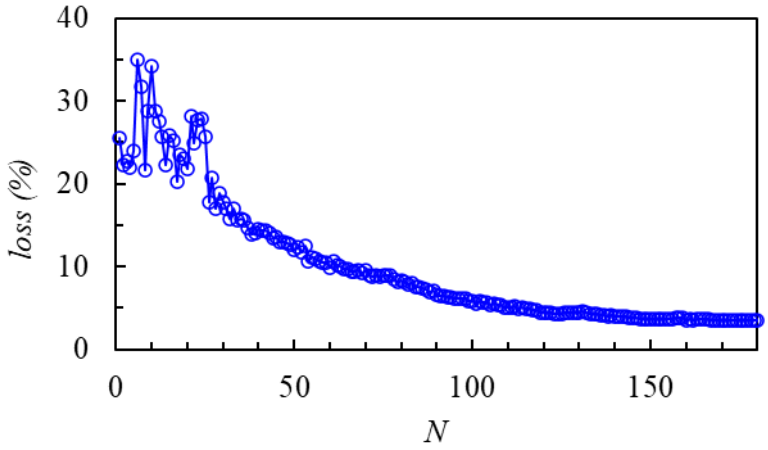


Figure 6.15. **The loss function in relation to the number of modes involved for field reconstruction *N*.**

Furthermore, the reconstructed fields using 5, 25 and 50 modes and the original field are shown in Figure 6.16. The time trace is chosen to be at $t = 0.5T$, i.e. $t = 0.5(n-1)\Delta t$. The reconstructed field using 50 modes and the original field are in fairly good agreement.

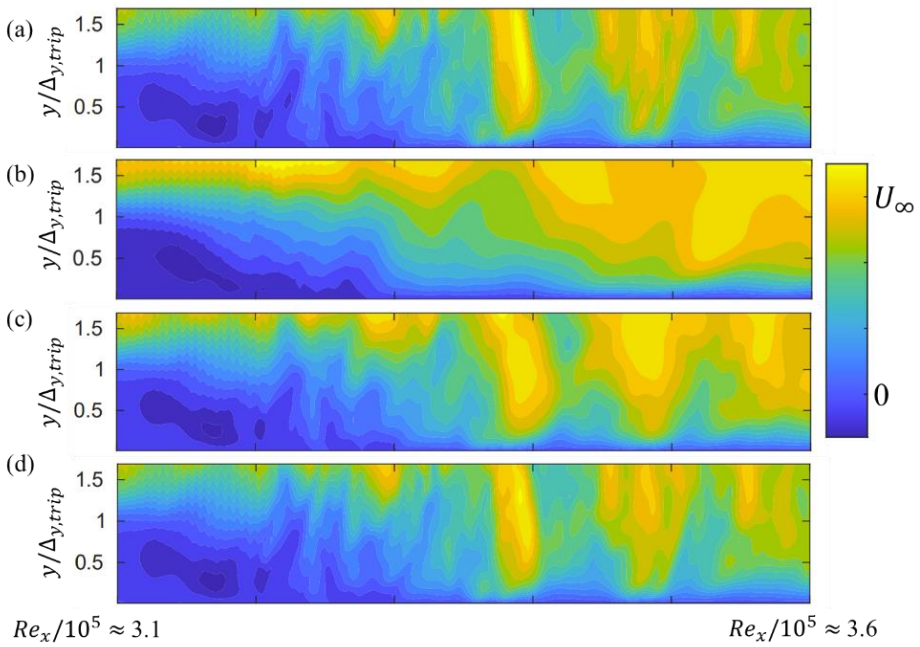


Figure 6.16. **The reconstructed field compared with the original. (a) The original simulated flow in the full-LES case (*RFTrip-x10z7*), (b, c, d) The reconstructed field using 5, 25 and 50 modes respectively.**

There are various selection criteria to identify the dominant modes (Jovanovic, et al. 2014; Tissot, et al. 2014). The corresponding mode frequency is non-dimensionalised in the form of Strouhal number $St = \frac{fL}{U}$, where the frequency f is calculated from the imaginary part of the eigenvalue λ_j, together with the trip height as the characteristic length and the freestream velocity. In the present study, the most dominant mode amplitude is selected at the primary vortex shedding frequency $St \approx 0.3$ (Figure 6.11) as the first mode. The dominant modes are shown in Figure 6.17, with the second and third modes chosen at the 2nd and 3rd harmonics of the primary shedding frequency.

The alternating velocity components in the top left corner in the first mode right after the tripping element ($Re_x/10^5 \approx 3.1$) appear as the key feature of vortex shedding in the streamwise velocity flow field (Figure 6.17a). These features begin to break down at the streamwise location range of $Re_x/10^5 \approx 3.2$ to 3.3. Interestingly, the vortical signatures are seemingly dissected from $y/\Delta_{y,trip} \approx 1$, either keeping being convected downstream or propagated towards the near-wall region. There is a clear difference in magnitude between the downstream convected and the near-wall propagated. Thus, the outer-flow structures do not seem to be able to penetrate the inner layer with a significant effect. Note that in Agostini & Leschziner (2016), the magnitudes of the outer coherent large scales are identified to be similar to those of their 'foot-prints' on the near wall region. In the present work, we see no evidence of such 'foot-prints' from the outer flow region.

In relation to the streamwise evolution, we can also see that the large-scale trip-associated disturbances start to decay soon after generation. The largest scales in the most dominant mode (Figure 6.17a) decay the fastest. The shorter scales are generated later, but also seem to decay at a slower pace, as shown in Figure 6.17(b) and (c). This is in clear contrast to the 'foot-printing' features in a well-developed turbulent flow where large coherent streaky structures persist with a long lifetime.

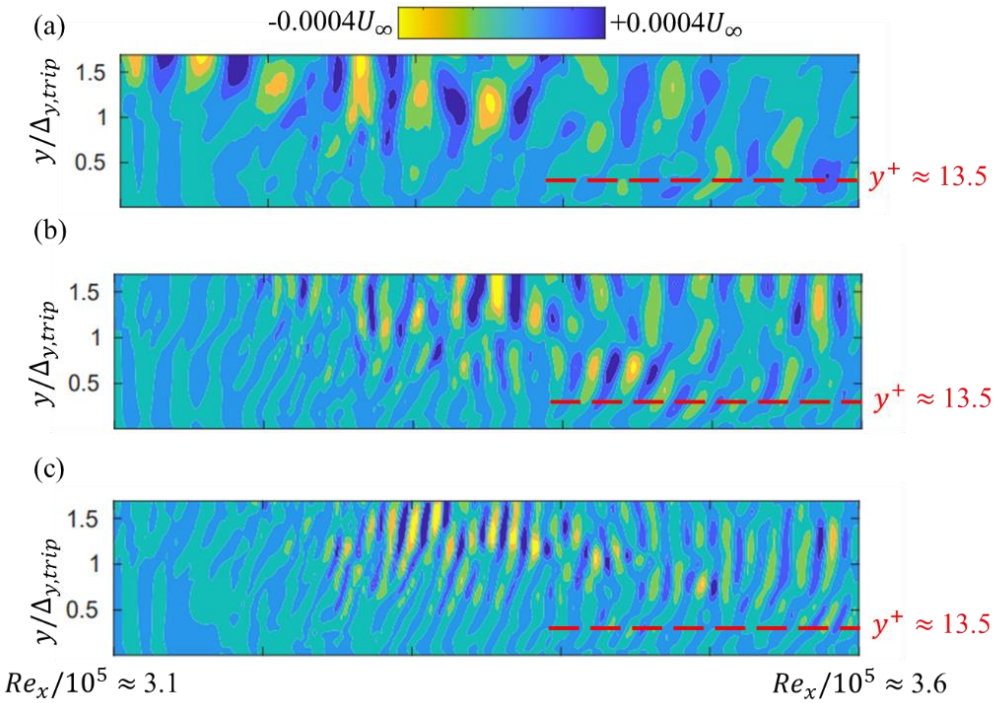


Figure 6.17. **The dominant modes extracted from the mid $x-y$ plane from full WRLES with frequency around (a) $St \approx 0.3$ (b) $St \approx 0.6$ and (c) $St \approx 0.9$. The blue contour corresponds to a negative value, while the yellow indicates a positive. The red line indicates the location of $y^+ \approx 13.5$, calculated by local shear velocity.**

Overall, the excessive energy observed in the outer flow region (Figure 6.10) is associated with the shed vortices over the tripping element. These vortical flow structures residing in the log region make the outer flow take longer to settle down to a complete equilibrium state. However, these tripping-induced large-scale residual disturbances share little similarity to the coherent large structures of long meandering streamwise streaks in fully developed turbulent flows. The tripping-induced large-scale disturbances decay in the streamwise direction, seemingly at a faster rate. These large scales also do not show any clearly discernible 'foot-prints'

on the near wall region. The characteristics observed may to some extent explain why the near-wall region is usually observed to experience a shorter development distance than the outer flow region before reaching an equilibrium state (Devenport & Lowe 2022).

6.5 Summary

We resort to a physical tripping method as widely adopted experimentally to initiate a TBL. For a simple 2-D step element to trip the TBL, extensive computational analyses are carried out, firstly to identify the adequate mesh refinement around the trip, and secondly to examine the evolution and impact of the large-scale disturbances associated with the tripping. We validate the full LES with Re_θ being approximately 1000 at the exit, of which the results match up well with well-established DNS results (Wu & Moin 2009; Schlatter & Orlu 2010; Schlatter & Orlu 2012) and the experimental correlation (Smits, et al. 1983; Chauhan et al. 2009; Monkewitz et al. 2007). It is found that a fine DNS mesh ($\Delta x^+ \approx 10, \Delta z^+ \approx 7$) should be sufficiently fine for resolving the trip without any local mesh refinement. A coarser mesh ($\Delta x^+ \approx 20, \Delta z^+ \approx 15$) would require local refinement for an adequate resolution, corresponding to a minimal 2% extra mesh count. The mesh sensitivities with and without local refinement indicate that a local wall-normal mesh spacing in wall-unit based on local shear stress should be kept smaller than 2 ($\Delta n^+ < 2$).

The development of the trip-induced bypass transition to TBL consists of four different stages: laminar, transitional, non-equilibrium and equilibrium. Excessive large-scale disturbances residing in the lower log region are associated

with the tripping, clearly and easily observable from spectral and modal representations. The outer portion of a tripped TBL with excessive energy is consistently and clearly shown to survive a longer distance downstream compared with the inner near-wall counterpart. Both modal analyses of EMD (Huang et al. 1998) and DMD (Schmid 2010) indicate that initial tripping-indicated large-scale disturbances do not have noticeable ‘foot-prints’ on the near wall. Moreover, the DMD modal analyses reveal that the streamwise decay of the trip-induced disturbances is scale-dependent, with larger scale disturbances decaying faster than shorter ones. Overall, not only do these large scales have no marked ‘foot-printing’ on the near wall, but they also seem to be more difficult to survive along the streamwise direction than those with shorter-length scales. This is in clear contrast to well-established wall-bounded turbulence at high Re where long coherent streaks appear persistently in the outer flow region with a marked ‘foot-printing’ on the near-wall part (Marusic et al. 2010).

7 TWO-SCALE SOLUTIONS FOR TURBULENT BOUNDARY LAYERS

Having initiated a TBL with the physical tripping as described in the last chapter, we now turn to solve the tripped TBL efficiently and accurately. In this chapter, for the tripped TBL, a Chebyshev BS mapping is adopted to propagate source terms from the local fine-mesh blocks to the global coarse-mesh domain, driving the upscaled equations to a target solution. The validity and effectiveness of the two-scale BS method are examined in this chapter for turbulent boundary layer flows.

The required capability to locally resolve a physical trip aligns closely with the basic attributes of the local embedded fine-mesh blocks as adopted in the two-scale method. A local fine-mesh block can be conveniently embedded around the tripping element to cover the transitional part, while the bulk flow can be efficiently resolved on a coarser base mesh. For a 2D-tripping element, the embedded fine-mesh block may be truncated in the spanwise direction. The sensitivity of the predicted tripping to the span size of the fine-mesh block will be also examined with the present two-scale method.

7.1 Sizing Locally Embedded Fine-mesh Block for Tripping

In Chapter 5, the sizing of the embedded block is discussed for a fully turbulent channel regime, chiefly based on the energy spectra generated from the DNS database (Lee & Moser 2015) with the analysis of the length scales of the near-wall 'universal' portion as well as in relation to the inner region in terms of the wall-normal distance based on Marusic et al. (2013). The streamwise and spanwise block lengths (Figure 3.4a) should accordingly be $l_x^+ \approx 3500$ and $l_z^+ \approx 350$ respectively, where '+' denotes the wall units based on the local shear velocity u_τ and viscosity ν. The height of the blocks are chosen to be $l_y^+ \approx 75$ in the turbulent region, consistent with the baseline WRLES study presented in chapter 5 and 6.

For the embedded fine-mesh block for the tripping, there should be a required development distance in the streamwise direction with a spatial coverage of essential features of the breakdown process of the initially shed vortices. The streamwise coverage of the first fine-mesh block l_{x1} should at least be long enough to cover the transition process. Given the observation made in chapter 6 on how far

downstream the laminar-to-turbulent transition would be largely complete, the streamwise length is chosen to reach $Re_\theta \approx 650$.

The sensitivity of the spanwise length of the fine mesh tripping block l_{z1} is studied through a set of cases shown in Table 7.1. The *Full-Span* case basically has the frontal block span l_{z1} covering the full spanwise width L_z. The *Half-Span* case reduces the frontal local DNS block span by half to be $L_z/2$. The minimum width of l_{z1} (*Mini-Span*) here is chosen to be the same size as that of the second fine-mesh block in the tripped TBL l_{z2}. The height of the frontal block l_{y1} is chosen to be unchanged in all these cases as approximately twice the trip height $\Delta_{y,trip}$, which corresponds to $y_s^+ \approx 75$ at the rear part of the first block in the turbulent region.

Table 7.1 Frontal block widths of the cases simulated

Case name	Full LES (chapter 6)	*Full-Span*	*Half-Span*	*Mini-Span*
block width $\boldsymbol{l_{z1}}$	L_z	L_z	$L_z/2$	$L_z/3$

The spectra generated from the numerical velocity probe placed at a location just downstream of the trip height show clearly stand-out peaks (Figure 7.1). These peaks correspond to the dominant shedding frequency and its 2nd and 3rd harmonics at the corresponding Strouhal number St, approximately 0.3, 0.6, and 0.9. At the most dominant shedding frequency ($St = 0.3$), the energy peak is well captured in all three cases. At higher frequencies with much less energy (less than 1% of the dominant peak), the *Half-Span* and *Mini-Span* are seemingly subject to more broadband disturbances.

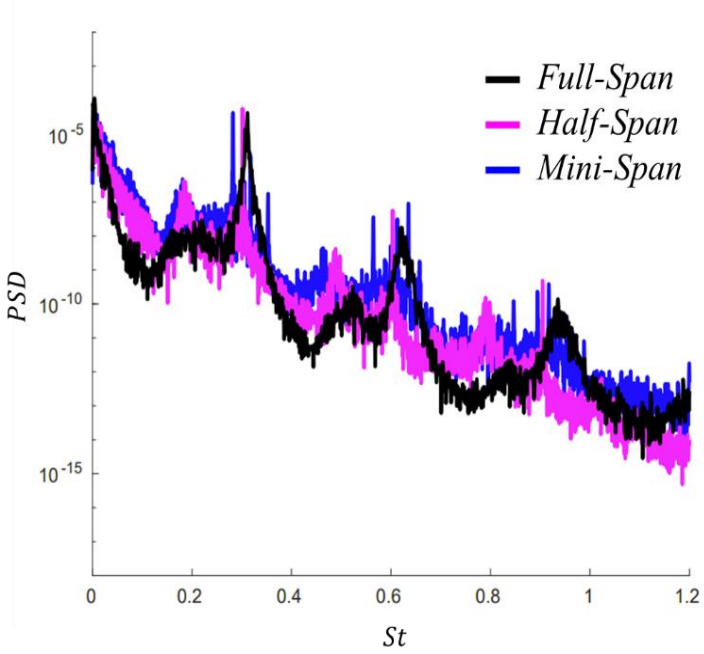


Figure 7.1. **Turbulence power spectra density (PSD) with respect to the non-dimensional frequency, Strouhal number St. The black, magenta and blue lines are for the *Full-Span*, the *Half-Span* and the *Mini-Span* results, respectively.**

It is worth investigating how these detailed differences at the trip between different spanwise block sizes may affect the downstream flow. Flow statistics including the mean velocity profiles and the fluctuations are extracted at two locations, as shown in Figure 7.2. The first is in the rear part of the frontal embedded block at $Re_\theta \approx 600$ and the second is in the rear part of the embedded block in the fully turbulent region at $Re_\theta \approx 800$. Also shown (Figure 7.3) are the energy spectra at these two locations. We see good agreement among the results of *Full-Span*, *Half-Span*, and *Mini-Span* in both locations, in the mean statistics and the energy spectra. It indicates that the downstream flow field is not sensitive to the spanwise size of the frontal block l_{z1}, as long as it covers at least one-third of full span.

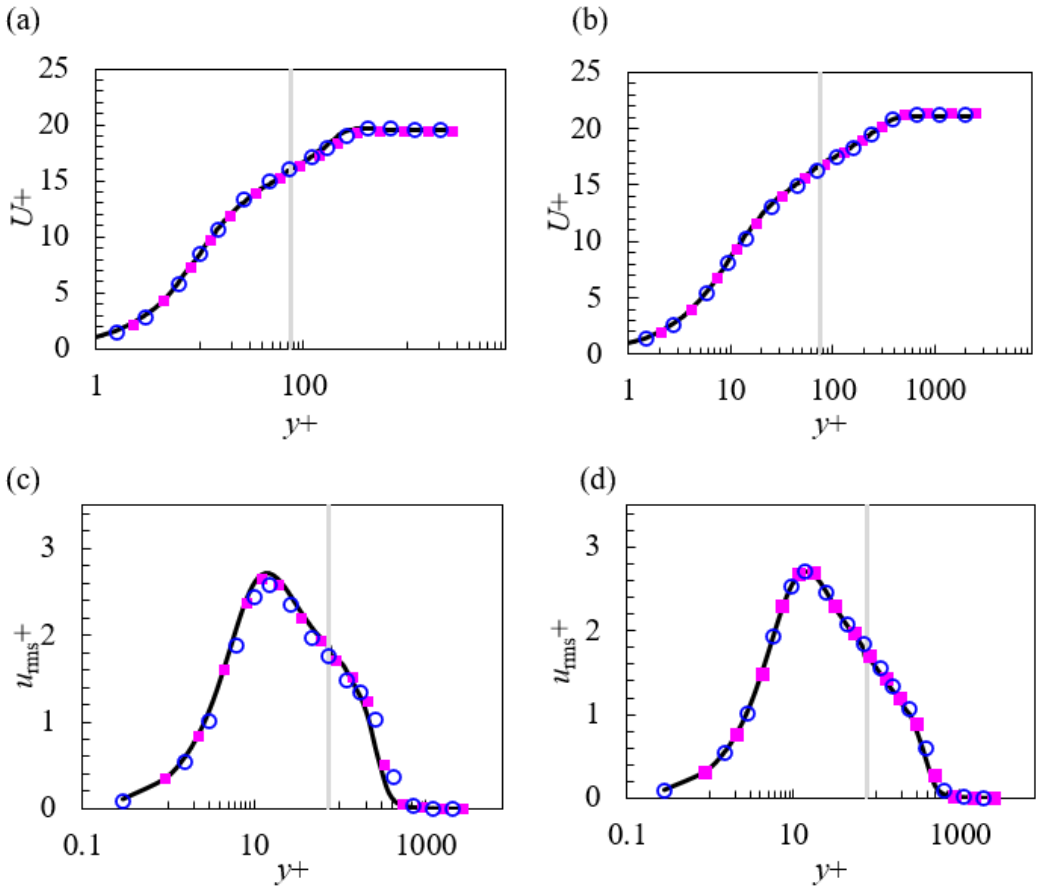


Figure 7.2. **Mean velocity profiles as functions of wall-normal distance y^+ at (a) $Re_\theta \approx 600$ and (b) $Re_\theta \approx 800$. Profiles of streamwise velocity fluctuations as functions of y^+ at (c) $Re_\theta \approx 600$ and (d) $Re_\theta \approx 800$. *Full-Span*: solid black lines '—'; *Half-Span*: solid magenta squares ■; *Mini-Span*: open blue circles ○. The grey lines '—' mark the inner-outer mesh interfaces. Note that not all data are shown for clarity.**

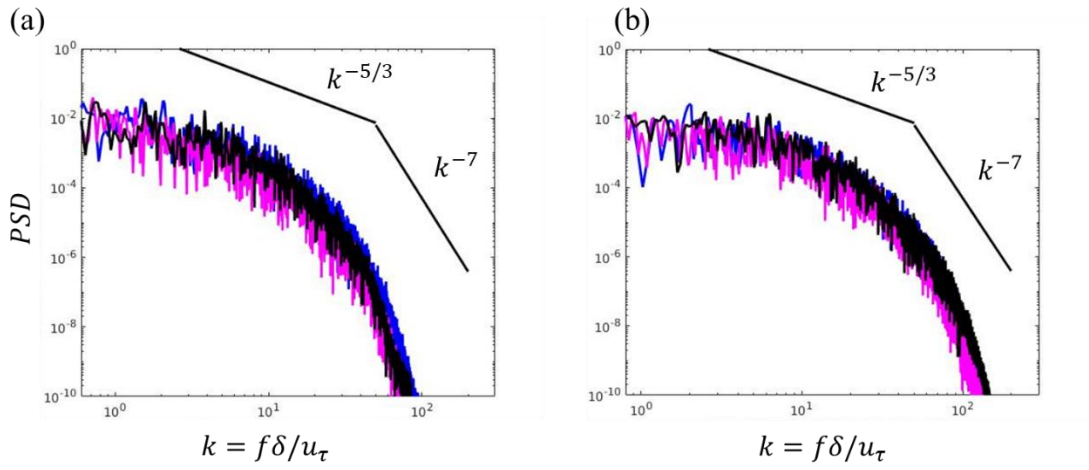


Figure 7.3. **PSD as functions of non-dimensional frequencies based on boundary layer thickness δ and wall shear velocity u_τ at (a) $Re_\theta \approx 600$ and (b) $Re_\theta \approx 800$. *Full-Span*: black lines '—'; *Half-Span*: magenta lines '—'; *Mini-Span*: blue lines '—'. The energy spectra are taken at $y^+ \sim 13.5$ as the peak energy location in Figure 7.2(c) and (d).**

To see more closely how the large-scale disturbances are triggered and evolve downstream in the embedded block, we now apply the DMD method here, in the same procedure as in section 6.4. We compare the mid-plane of the local fine-mesh block with a reduced span to that of the full LES solutions. The streamwise coverage starts from the trip ($x = 0.1l_{x1}$) towards the end of the frontal block ($x = l_{x1}$). The comparison between the two cases is shown in Figure 7.4. The transition process from shed vortical disturbances to the breakdown and formation of a new TBL is well captured in the embedded block, shown in Figure 7.4(b). The detailed features in the vicinity of the trip are slightly different, e.g., a slightly later breakdown process for the full LES (Figure 7.4a) compared to that for the locally embedded block (Figure 7.4b). Downstream, however, the difference between the two seems rather insignificant with the rapid decay of the large-scale disturbances

towards the end of the block. The overall picture of the streamwise evolution for the trip-induced large scales is in line with the observed insensitivities in the mean statics and energy spectra at $Re_\theta \approx 600$, indicating the adequate length scales of the locally embedded fine-mesh block for the tripping.

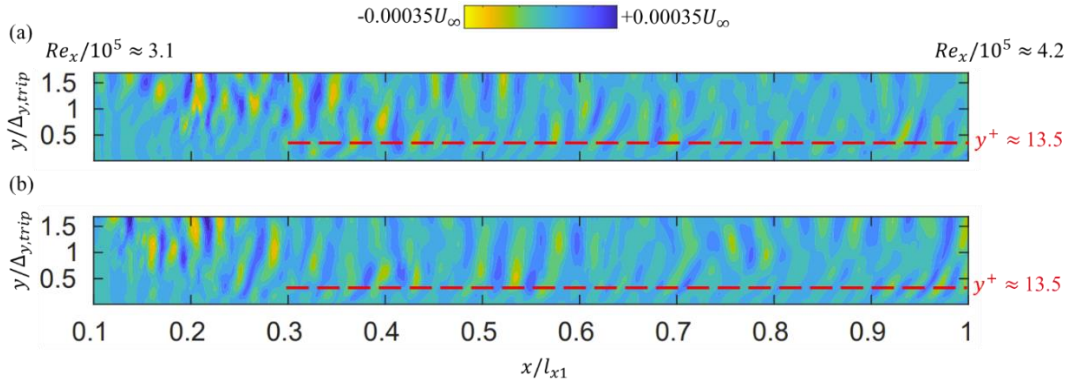


Figure 7.4. **Comparison of large-scale disturbances ($St \approx 0.3$) on the mid $x-y$ plane from (a) full LES and (b) the local DNS block.**

7.2 Two-scale Solution for Tripped TBL

7.2.1 Validation against Baseline Full LES

One key variable sensitive to the near-wall mesh resolution is the wall shear stress as shown in the mesh-dependency study in section 6.2. The accurate calculation of the wall shear stress is of great importance in many spatially developing flows (Launder & Spalding 1974). The computed friction coefficient C_f as the indicator of the wall shear stress prediction is shown in Figure 7.5 as the function of the local Reynolds number. The full LES result is shown as the baseline reference which has been validated against well-established experimental results and

DNS databases, as shown in section 6.2. The direct solution with locally embedded blocks but without the source-term correction labelled as 'one-scale', is seen with a significant discrepancy, because of the under-resolution of the near-wall coarse mesh. In the present two-scale approach, the mean flow is corrected through the block-spectral (BS) method, where the error is significantly reduced. The rest of the present two-scale results in this subsection are thus all taken with the *Mini-Span* for the embedded fine mesh tripping block.

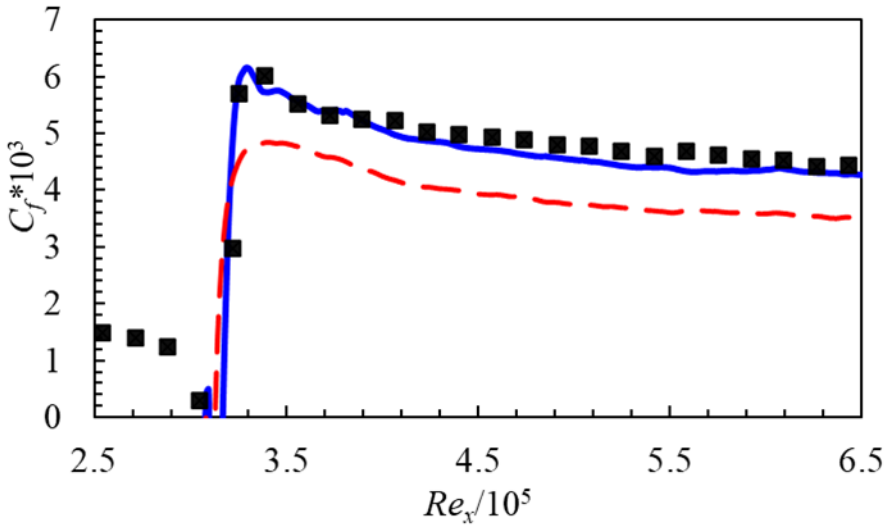


Figure 7.5. **The friction coefficient C_f as the function of Reynolds number Re_x. The blue solid line '—' is for the present two-scale block-spectral solution in the global coarse region. The solid black squares '■' indicate the full LES results. The red dash line '— —' shows the one-scale solution in the global coarse region without any source-term correction.**

The mean velocity profiles on the global coarse mesh at the exit of the domain where $Re_\theta \approx 1000$ are compared as shown in Figure 7.6. The under-resolved one-scale solution with no source-term correction gives poor results with large errors

(~19 %). The impact of the source term correction is clearly highlighted by the two-scale BS solution agreeing well with the DNS results (Schlatter & Orlu 2012).

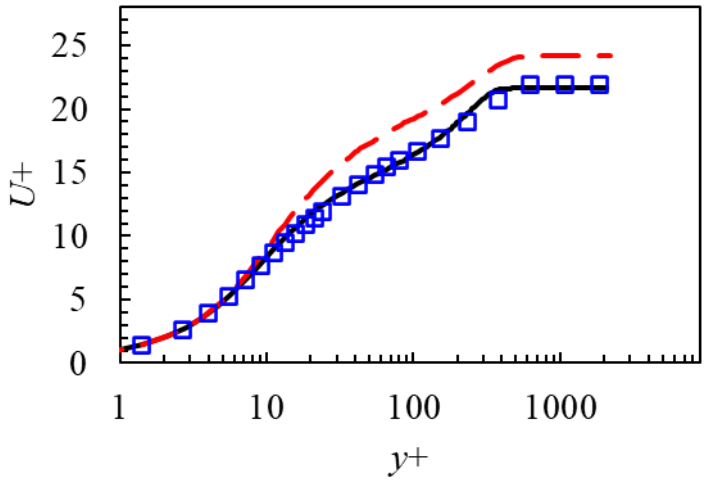


Figure 7.6. **The mean velocity profile in relation to wall normal distance y^+ in the global coarse-mesh region. The present two-scale BS solutions (blue squares □) is compared with the DNS results from Schlatter & Orlu (2012) (black solid lines '—') at the Reynolds numbers $Re_\theta \approx 1000$. The red dash line '— —' is for the one-scale solution without the source-term correction.**

It should be pointed out that the source term mapping for the tripping region covered by the first embedded fine mesh block is different from that for the rest of the TBL. As shown previously in chapter 6, the trip-induced transition process is subject to large-scale disturbances of large amplitudes highly interactive particularly shortly downstream of the trip element. As a result, the region from $Re_x/10^5 \approx 3$ to 4 (Figure 7.5) experiences a much higher gradient in the streamwise direction than the rest of the TBL. Consequently, for the frontal tripping region, the source terms generated in the first fine-mesh block are only propagated in the spanwise direction. They are directly mapped to the full span coarse-mesh region. The source term

components in the x, y and z directions, ST_x, ST_y and ST_z, are shown in Figure 7.7, where dash lines indicate those source terms generated from the frontal fine-mesh tripping block to be mapped directly to the full span of the corresponding coarse-mesh region.

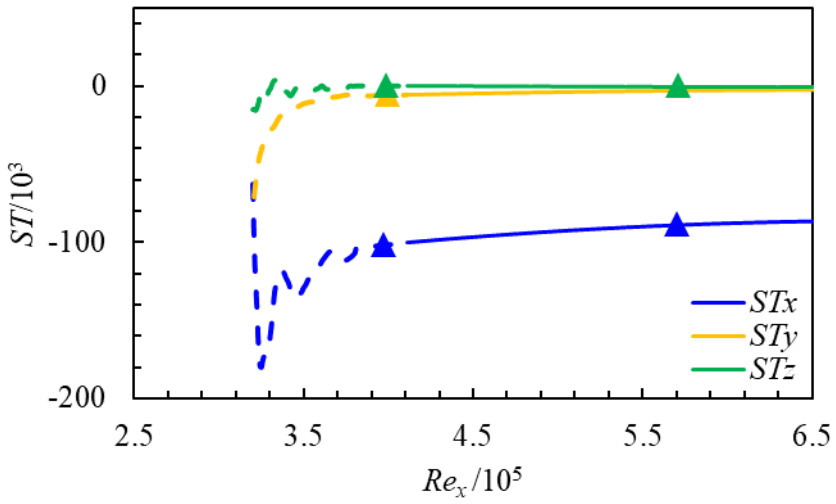


Figure 7.7. **Distribution of source term vectors $\boldsymbol{ST} = (\boldsymbol{ST_x}, \boldsymbol{ST_y}, \boldsymbol{ST_z})$ along the streamwise direction as functions of Reynolds numbers $\boldsymbol{Re_x}$ in the viscous sublayer ($\boldsymbol{y^+ \approx 6}$). The blue dash lines '– –' indicate $\boldsymbol{ST_x}$ for the frontal trpping block with spanwise mapping only. The solid blue lines '—' indicate the spectrally mapped results from the Chebyshev method for the rest of TBL. The solid blue triangles ▲ mark the sample points. The other two scalar components $\boldsymbol{ST_y}$ and $\boldsymbol{ST_z}$ are shown in yellow and green, respectively.**

From $Re_x/10^5 \approx 4$ onwards, the streamwise change of the flow development and the wall shear stress is much more gradual as it enters a fully turbulent region. The source term distribution along the streamwise direction also becomes much smoother. The Chebyshev spectral method introduced in section 3.4 is applied here for the source-term propagation. Two sample points for constructing

the streamwise Chebyshev spectrum, in this case, are marked by triangle symbols in Figure 7.7. One is at the rear portion of the frontal fine mesh block, and the other is at the rear of the second fine mesh block embedded in the fully turbulent region.

The mean velocity and the fluctuations in '*rms*' in the near-wall fine-mesh blocks and adjacent coarse-mesh region are compared with the full LES results at two locations in Figure 7.8, showing good agreement. Figure 7.8(a, b) show the results at the rear part of the frontal block at $Re_x/10^5 \approx 4$ with the corresponding $Re_\theta \approx 600$. Figure 7.8(c, d) are for the results at the rear part of the second block at $Re_x/10^5 \approx 5.7$ with the corresponding $Re_\theta \approx 800$.

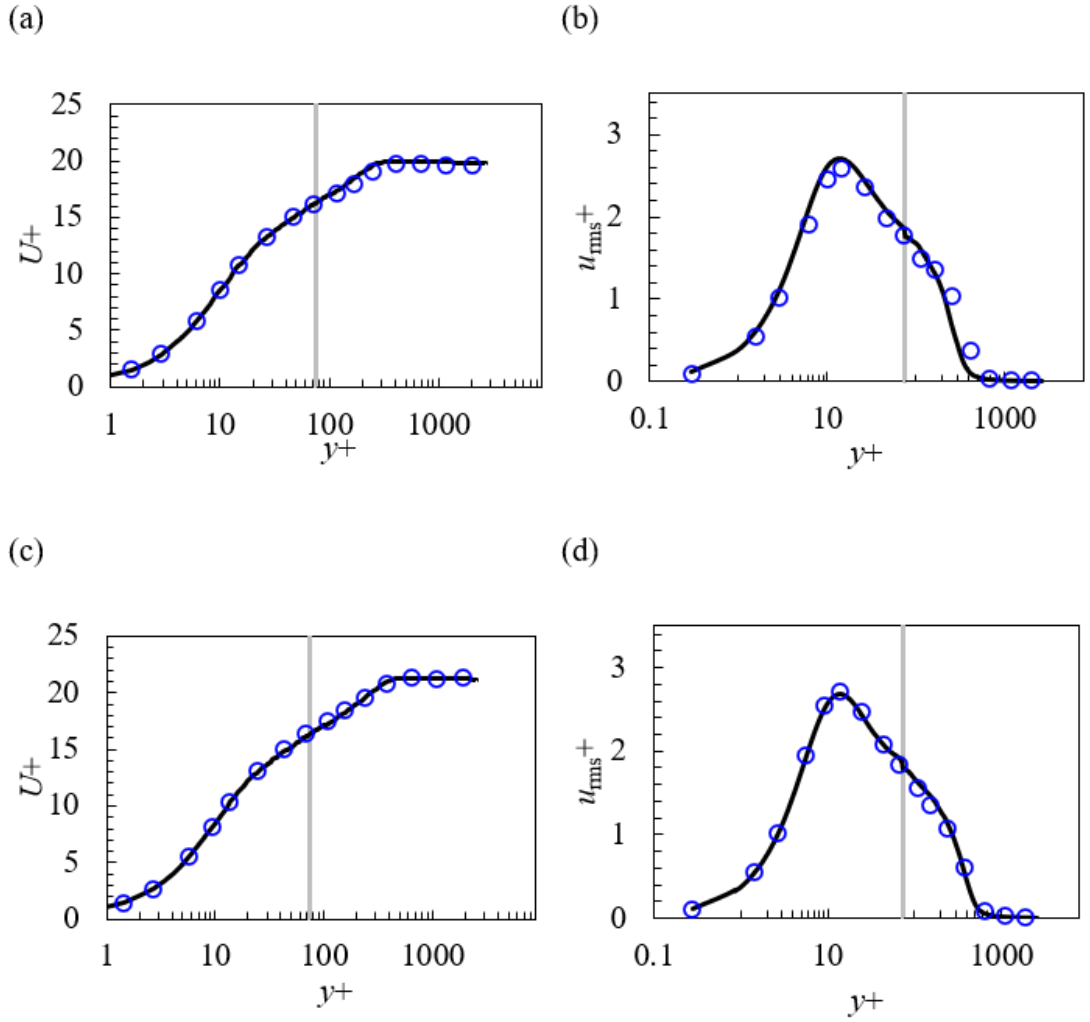


Figure 7.8. **Mean statistics. (a, c) the mean velocity profiles and (b, d) streamwise velocity fluctuations with respect to the wall-normal distance. The present two-scale BS solutions (blue circles ○) are compared with the full LES solutions (black solid lines '—') at two Reynolds numbers: (a, b) $Re_\theta \approx 600$ and (c, d) $Re_\theta \approx 800$. The grey lines '—' mark the inner-outer mesh interfaces. Note that not all data are shown for clarity.**

Shown in Figure 7.9 are the energy spectra at these two Reynolds numbers in the fully turbulent regime. The spectra are taken at the near-wall region at $y^+ \approx 13.5$. The dimensionless frequency is again calculated based on the boundary layer

thickness and wall shear velocity: $k = f\delta/u_\tau$. Firstly, note that the results from the present two-scale method overlap with the full-LES spectra. Secondly, the fine-mesh DNS block is shown to be able to resolve the full range of turbulent scales. The PSD taken from the embedded region confirms a full coverage of the spectral range in the local fine-mesh block. More remarkably, the fine mesh spectrum overlaps smoothly with the coarse-mesh PSD at lower frequencies without any spectral gap. This is attributed to the embedded block receiving low-frequency large-scale signals directly from the global coarse mesh domain, thanks to the scale-dependent interface method. The global coarse mesh is capable of resolving the large scales, but experiences high numerical dissipations at shorter wavelengths for the higher frequency range, as expected. The corresponding under-resolution is corrected by the source terms to drive towards the target time-mean flow. The present observations for the fully turbulent region at local Reynolds numbers $Re_\theta \approx 600$ and 800 are consistent with the findings for a canonical channel flow by Chen & He (2022), highlighting the advantage of the scale-dependent interface treatment over the direct periodic condition, a common limit in previous MFU-based solution methods.

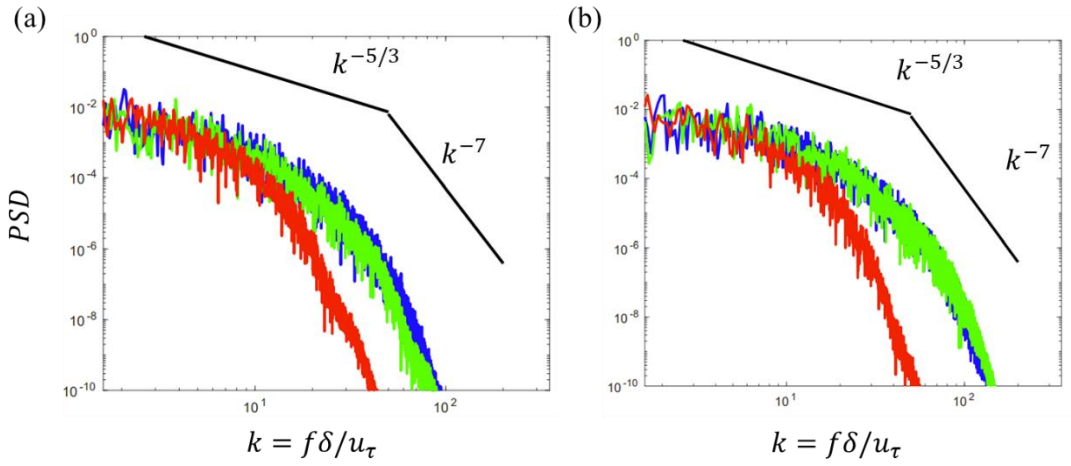


Figure 7.9. **PSD with respect to the dimensionless frequencies. The present two-scale BS solutions (blue lines '—') are compared with the full LES solutions (green lines '—') at two Reynolds numbers: (a) $Re_\theta \approx 600$ and (b) $Re_\theta \approx 800$. Red lines '—' are for the results in the global coarse region. The energy spectra are taken at $y^+ \sim 13.5$.**

7.2.2 Cases with Higher Reynolds Numbers

For validation, other than the calculations in section 7.2.1, we have another two cases simulated for higher Reynolds numbers ($Re_\theta \approx$ 1500 and 2600) at the exit, essentially with mesh resolution following the scaling guideline, having $N_s = 2$ in Figure 7.12. The simulation parameters are shown in Table 7.2. Both of the cases have the frontal block embedded identically as that in section 7.2.1 and the second block embedded close to the exit. All configurations in wall units are normalised by the local shear velocity u_τ at the specific Reynolds numbers Re_θ. The fluid domain

simulated are $\Omega = [0, L_x] \times [0, L_y] \times [0, L_z]$, with the domain used in section 7.2.1 denoted as $\Omega' = [0, L_x'] \times [0, L_y'] \times [0, L_z']$ for comparison purposes.

Table 7.2 Simulation parameters of calculations with higher Re

$\boldsymbol{Re_\theta}$	Domain	$\boldsymbol{G}$: $\boldsymbol{L_x, L_z}$ $\boldsymbol{L}$: $\boldsymbol{l_x^+, l_z^+}$	$\boldsymbol{G}$: $\boldsymbol{L_y}$ $\boldsymbol{L}$: $\boldsymbol{y_s^+}$	$\boldsymbol{\Delta_x^+, \Delta_z^+}$	$\boldsymbol{N_y}$	$\boldsymbol{\Delta_{y,w}^+}$
1500	G	$1.53L_x', L_z'$	~6δ at exit	38, 28	104	0.5
	L	~3000, ~400	75	9.5, 7	52	
2600	G	$4L_x', L_z'$	~6δ at exit	44, 30	132	
	L	~3000, ~370	90	11, 7.5	67	

Validations of the solution accuracy are shown in Figure 7.10 and Figure 7.11. Figure 7.10 demonstrates the friction coefficient C_f as the function with respect to the Reynolds number Re_θ. Figure 7.11 shows the mean statistics at the two Reynolds number with the local DNS block embedded. All two-scale solutions match up quite well with the correlated curves (Smits, et al. 1983) and the DNS database (Schlatter & Orlu 2010).

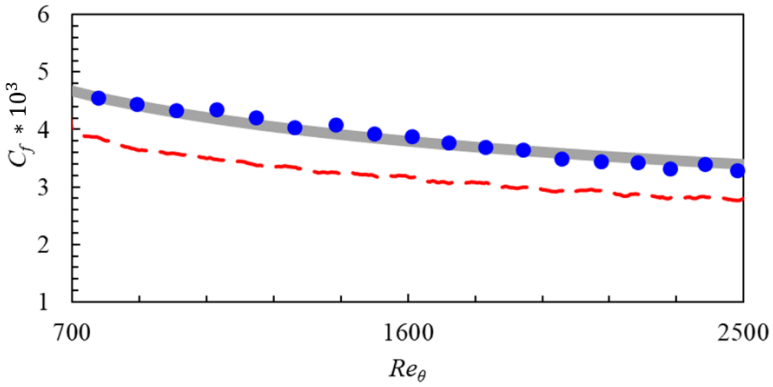


Figure 7.10. **The friction coefficient C_f as the function of Reynolds number Re_θ. The solid grey lines '—' indicate the correlated curve by Smits, et al. (1983). The blue symbols '●' are for the present two-scale BS solutions. The red dashed lines '– –' are for the one-scale solutions without the source-term coupling. Both results are taken from the global coarse-mesh region. Note that not all data points are shown for clarity.**

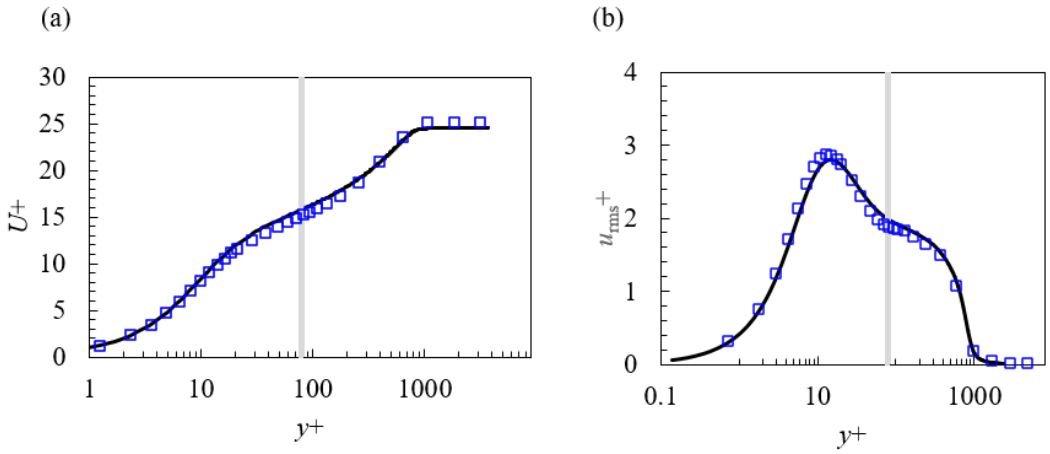


Figure 7.11. **Mean statistics. (a) the mean velocity profiles and (b) streamwise velocity fluctuations with respect to the wall-normal distance. The present two-scale BS solutions (open blue squares □) are compared with the DNS results (black solid lines '—') at Reynolds numbers $Re_\theta \approx 2540$. The grey lines '—' mark the inner-outer mesh interfaces. Note that not all data points are shown for clarity.**

7.3 Mesh Count – Reynolds Number Scaling

In this final section, we examine the mesh count - Reynolds number scaling for the spatially developing TBL to evaluate the potential benefit in terms of computational cost for the present two-scale method. As a laminar-to-turbulent transition (regardless of the way of initiation) should happen at a largely fixed Reynolds number, we shall only consider a fully turbulent part of the boundary layer starting from the upstream station x_0, to the downstream $x = L_x$ where the Reynolds

number based on either the total length or the maximum boundary layer thickness is calculated.

We assume that the whole TBL can be divided into N_s subdomains, as shown in Figure 7.12(a). Within each subdomain, we have one locally embedded near-wall fine-mesh block. As such, a subdomain can be approximately viewed as a channel flow with the local mean boundary layer thickness δ being taken as the half channel height (Figure 7.12b).

The total mesh count required for the whole TBL ($x_0 < x < L_x$) is

$$N_{total} = \sum_{i=1}^{N_s} N_i(Re_{\delta_i}) \tag{7.1}$$

where the total mesh-count N_{total} is a summation of local mesh-counts for N_s subdomains (Figure 7.12a). For sub-domain i, its mesh count N_i depends on the local Reynolds number Re_{δ_i} based on the freestream velocity U_∞, the kinematic viscosity ν and the local boundary layer thickness δ_i. For each subdomain, the boundary layer thickness can be approximately taken as a constant. Thus, a local TBL flow in a subdomain is equivalent to a channel flow (Figure 7.12b).

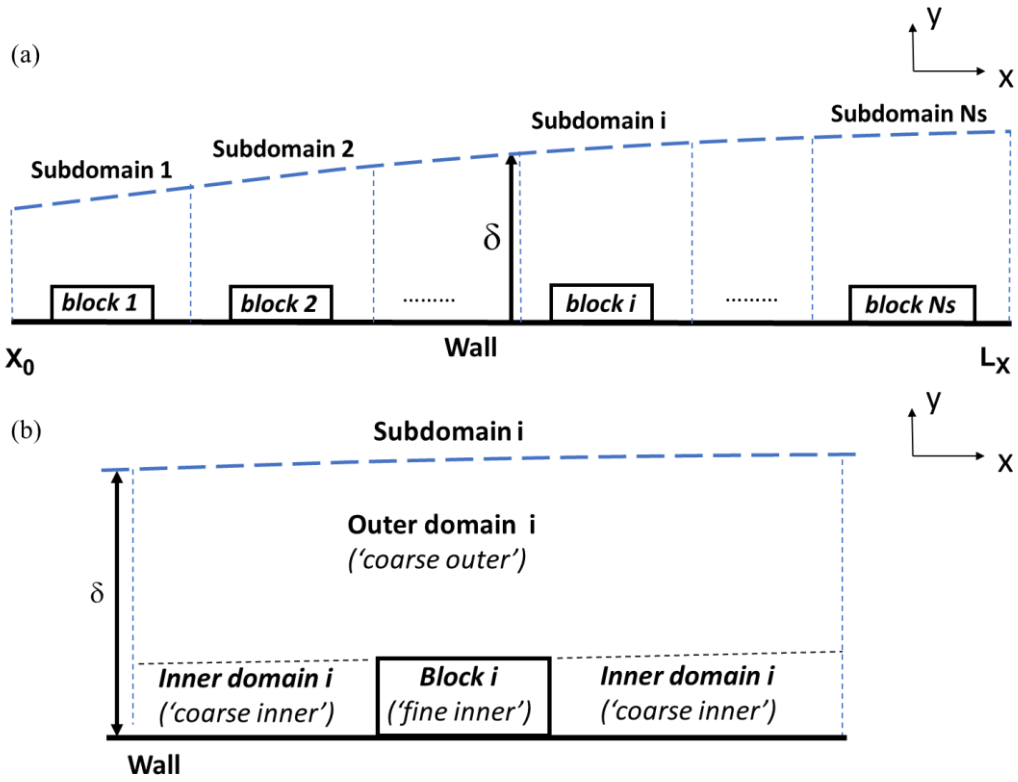


Figure 7.12. **Sectioned TBL domain: (a) Illustration of the TBL domain with N_s sub-domains. (b) A close-up view of the sub-domain i.**

Following Choi & Moin (2012), the local mesh count is estimated as $NLES_{local} \sim {Re_\delta}^{11/6}$ for wall-resolved LES and $NDNS_{local} \sim {Re_\delta}^{11/4}$ for DNS. For the present two-scale method, there should be one embedded fine-mesh DNS block in each subdomain. As indicated above, the mesh count $N_i(Re_\delta)$ for subdomain i can be estimated similarly to a channel flow. In Chen & He (2022), the mesh count for a channel flow with δ denoting the channel half-height is estimated as

$$NLES_{channel} = NLES_{fine\ inner} + NLES_{coarse\ outer} + NLES_{coarse\ inner} \sim \delta^+ \tag{7.2}$$

The three terms on the right-hand side corresponding the three domains (Figure 7.12b) are estimated as

$$\begin{cases} NLES_{fine\ inner} = NDNS_{embed\ block} \sim y_s^+ \sim {\delta^+}^{0.5} \\ NLES_{coarse\ outer} \sim \int_{y_s}^{\delta} \delta^2 \,/\, y^3 \, dy \sim \delta^+ \\ NLES_{coarse\ inner} \sim \delta^+ \end{cases} \tag{7.3}$$

where y_s marks the starting point of the log region, being proportional to ${\delta^+}^{0.5}$ (Marusic et al. 2013). In the present TBL case, we replace δ denoting the half-channel-height for channel flow by the local boundary layer thickness δ_i. From Choi & Moin (2012), scaling can be represented with different Reynolds number definitions through the conversion as $Re_\delta \sim (\delta^+)^{12/11}$. Thus, correspondingly equation (7.2) can be rewritten in terms of local TBL thickness for subdomain i as

$$NLES_i(Re_{\delta_i}) \sim {Re_{\delta_i}}^{11/12}. \tag{7.4}$$

Furthermore, we assume the local Reynolds number for subdomain i can be approximately correlated to the overall Reynolds number Re_δ based on the downstream boundary layer thickness by $Re_{\delta_i} = C_i Re_\delta$, where C_i is a multiplier coefficient for subdomain i ($0 < C_i < 1$). The multiplier coefficient should remain roughly constant when the TBL Reynolds number Re_δ varies. Equation (7.1) can then be expressed as:

$$NLES_{total} \sim Re_{\delta}^{11/12} \sum_{i=1}^{N_s} f_i(C_i).$$

(7.5)

As f_i for the subdomain i is only a function of the local multiplier C_i independent of Reynolds number, we will then have:

$$NLES_{total} \sim Re_{\delta}^{11/12}.$$

(7.6)

Therefore, the overall mesh count in TBL is reduced from $O(Re_{\delta}^{11/6})$ for the full wall-resolved LES (WRLES) to $O(Re_{\delta}^{11/12})$ for the two-scale solutions. Figure 7.13 shows the mesh count - Re scaling for the different solution approaches.

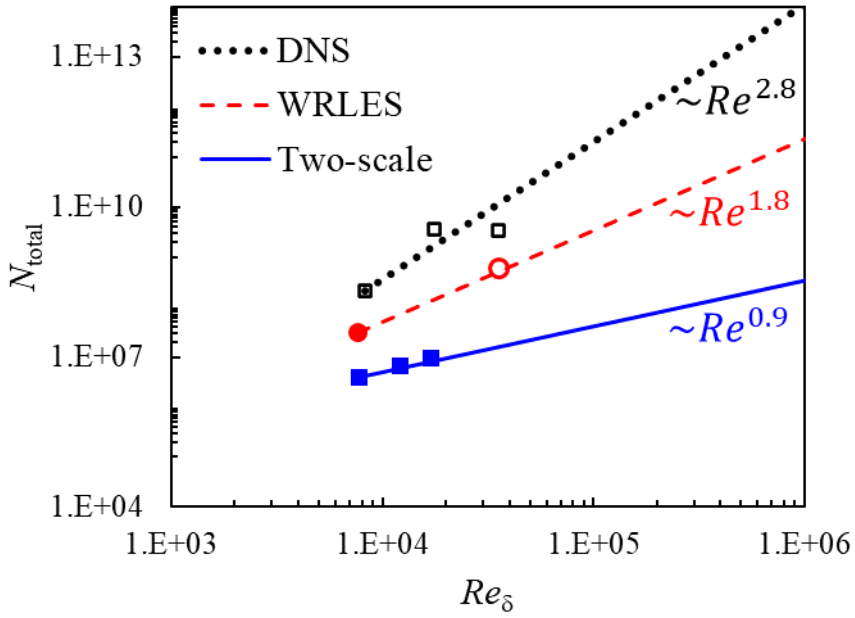


Figure 7.13. **Mesh count - Re scaling. DNS (black dots '▪'); wall-resolved LES (red dash line '— —'); the present two-scale method (blue solid line '—'). The open black square '□' and red circle '○' are for the actual N_{total} as reviewed in Deck, et al. (2014). Solid red circle '●': total mesh count in the present full WRLES (chapter 6); Solid squares '■': two-scale calculations (chapter 7).**

7.4 Summary

The principal objective of this thesis is to explore an efficient and accurate methodology for scale-resolving simulations. Previously, chapter 5 demonstrates a two-scale method for the canonical turbulent channel flow where the mesh-count scaling with Reynolds number is potentially reduced from $O(Re^2)$ of the full wall-resolved LES to $O(Re^1)$. This chapter extends the methodology to spatially evolving boundary layers.

When implementing the two-scale method in the boundary layer flow, the tripped transition is covered by a locally embedded frontal fine-mesh block. The tripping effects on the downstream turbulent regime are seemingly insensitive to the spanwise size of the frontal fine-mesh block. Characteristics of large-scale unsteadiness around the trip appear to be similar regardless of the spanwise size of the embedded block though detailed spectra over the trip show some differences. These differences manifested in the local spectra around the trip seem to vanish quickly further downstream with very limited history effects. Therefore, the frontal fine-mesh block with a short span comparable to those embedded blocks for the tripped TBL is deemed adequate.

For a non-homogeneous boundary layer, the block-spectral (BS) mapping of the time-invariant source terms with the Chebyshev spectral method is shown to be effective. The space-time-averaged fine-mesh solutions are taken as a target, leading to source terms for the upscaled equations for the corresponding coarse-mesh region. The source terms generated from the locally embedded near-wall fine-mesh blocks are propagated to the global coarse-mesh near-wall region by use of the Chebyshev method. The present two-scale BS method is validated by comparing the calculated mean statistics and energy spectra with full LES and DNS results. Finally, the scaling of computational mesh count with respect to the Reynolds number (based on the boundary layer thickness δ) is estimated. It is highlighted that the overall mesh count - Re scaling may be potentially reduced from $O({Re_\delta}^{1.8})$ for the full wall-resolved LES to $O({Re_\delta}^{0.9})$ for the present locally embedded two-scale method.

8 CONCLUSIONS AND RECOMMENDATIONS FOR FUTURE WORK

An efficient two-scale method for wall-bounded flows is developed based on the original framework in He (2018) and He (2021), implemented, and validated in the canonical channel flows and boundary layer flows. Locally refined DNS blocks are embedded in the near-wall region, coupled with the global region with a coarser mesh.

Recall the four research questions raised in chapter 1:

1) How can the local embedded region receive the influence of the large-scale coherent structures?

2) How can the under-resolved region be conditioned with minimised discretisation errors?
3) How can a turbulent boundary layer be properly initiated with clearly and consistently applied inflow conditions in scale-resolving numerical simulations?
4) How much computational saving could be achieved through the two-scale method?

The first research question is addressed by the distinctive and closely relevant capability of the scale-dependent interface treatment, compared to the previously commonly adopted minimum flow unit (MFU) based method. The coarse-mesh scale resolved disturbances are directly exchanged across a coarse-fine mesh domain interface, whilst only are the fine-mesh resolved fluctuations around the coarse-mesh variables subject to the periodic condition at the pairing boundaries of the fine-mesh block. The global influence of the outer coherent large scales as the 'foot-printing' and is received by the locally embedded region with the interactive 'modulation' sufficiently captured. On the other hand, the common limit of MFU approaches is their imposed periodicity on the flow unit boundaries from which the 'foot-printing' effect is not capable of being captured.

The second research question is addressed by the source-term-oriented approach. The coupling between the two domains is facilitated by a space-time averaging of the fine-mesh solution over the corresponding coarse-mesh cells. The source terms as the residual imbalance are mapped to the under-resolved global near-wall coarse-mesh region for driving the time-mean flow field converging to the target fine-mesh solutions. These source terms effectively balance out the under-

resolution associated errors for the time-averaged solution over the coarse mesh. In the fully developed turbulent channel flows, with homogeneity in both the streamwise and spanwise wall-parallel directions, source terms can be simply duplicated to be added to the near-wall global coarse-mesh region. For the spatially evolving boundary layer flows, we resort to the Chebyshev spectral method for the source term interpolation and propagation. The present two-scale block-spectral (BS) method is validated by comparing the calculated mean statistics and energy spectra with full LES and DNS results.

The two fundamental cases as the channel flows and TBL flows are studied in this thesis for concept proof and validation purposes, where further work could potentially be carried out investigating the present two-scale BS method implemented in more complex fluid flows, for example, 3-D flows with zero homogeneous direction, boundary layer flows with adverse pressure gradients, etc. These may lead to a wider application of the method, and the way of propagating the source terms could lead to a series of future work, relevant to machine-learning-based modelling, Gaussian process regression, etc.

When studying the turbulent boundary layer, a simple physical tripping method is adopted to initiate the TBL via locally numerically resolving a 2-D roughness element. The third research question is addressed by two main points. Firstly, it is demonstrated that directly resolving the trip is requesting only marginal extra computing resources compared with a typical mesh required for a scale resolving TBL solution at a similar Reynolds number. Secondly, the tripping-induced excessive large-scale disturbances residing in the lower log region do not have noticeable ‘foot-prints’ on the near wall. Also, they seem to have difficulty surviving

along the streamwise direction compared to those with shorter-length scales. This is in clear contrast to well-established wall-bounded turbulence at high Reynolds numbers where long coherent streaks appear persistently in the outer flow region with a marked 'foot-printing' on the near-wall part. Overall, the physical tripping resolving a simple roughness element provides an option to properly initiate a TBL with clearly and consistently applied inflow conditions.

In terms of a physically tripped laminar-to-turbulent transition, a tripping device that overly buffets the inflow (e.g., a wire as thick as the boundary layer) will inevitably trigger large-scale disturbances whose signatures could retain very further downstream, as shown in Marusic, et al. (2015). A relevant interesting aspect for further study may be how an overly triggered laminar-to-turbulent transition and an over-stimulated turbulent boundary layer would develop towards the equilibrium state in numerical simulations and how the large-scale disturbances would affect the downstream in this case as posed by Marusic, et al. (2015). This will involve full LES or DNS simulations at much higher Reynolds numbers compared to the ones carried out in the present study.

Finally, a substantive appeal for developing such a local-embedded fine-mesh method is the possibility for much more efficient scale-resolving simulations whilst avoiding taking the wall-modelled avenue. The relevant research question 4 as how much computational saving could be achieved is addressed by the mesh count – Reynolds number scaling. For a canonical turbulent channel flow, is potentially reduced from $O(Re^2)$ for wall-resolved LES to $O(Re^1)$ for the present two-scale method. For the spatially evolving boundary layer flow, it is estimated to reduce

from $O(Re^{1.8})$ for the full wall-resolved LES to $O(Re^{0.9})$ for the present two-scale BS solution.

The fundamental studies in this thesis regarding wall-embedded LES/DNS, for simplicity, set the wall-normal inner coarse mesh point distribution the same as the local embedded fine-mesh block. A relevant question is how coarse the under-resolved near-wall region could be, as the mean solutions there are supposed to be corrected through the source-term-oriented approach. Notice that this region is still the near-wall portion of the global region and should be in charge of resolving the large scales as the 'foot-prints' of outer coherent large-scale structures. For this attribute, the mesh resolution in the wall-normal direction has to be adequately fine to resolve the large sales and also does not necessarily have to be strictly the same as the local DNS block. Further studies are expected on dealing with the non-conformal mesh interface between the coarse and fine regarding node distribution in the wall-normal direction.

Note that even though the thesis focuses only on incompressible flows with the basic canonical channel flow and boundary layer flow studied, the present two-scale method has been and will continue to be explored. The implementation of the two-scale method to flows with compressibility has been demonstrated by He (2021). The lumped source terms should be including the scalar sum of all viscous stress terms from the energy equation as well in this case. The source terms as the lumped form of viscous terms underline that regardless of whether the terms are modelled by empirical correlation or directly calculated from fine-mesh solutions, what matters for each flow equation is simply the scalar sum. This fundamental feature will be further utilised in future work studying more complex flows.

9 REFERENCES

Adler, M., Gonzalez, D., Stack, C. & Gaitonde, D., 2018. Synthetic generation of equilibrium boundary layer turbulence from modeled statistics. *Computers and Fluids*, Volume 165, pp. 127-143.

Adrian, R., 2007. Hairpin vortex organization in wall turbulence. *Physics of Fluids*, Volume 19, p. 041301.

Adrian, R., Meinhart, C. & Tomkins, C., 2000. Vortex organization in the outer region of the turbulent boundary layer. *J. Fluid Mech*, Volume 422, pp. 1-54.

Agostini, L. & Leschziner, M. A., 2014. On the influence of outer large-scale structures on near-wall turbulence in channel flow. *Physics of Fluids*, 26(7), p. 075107.

Agostini, L. & Leschziner, M. A., 2016. On the validity of the quasi-steady-turbulence hypothesis in representing the effects of large scales on small scales in boundary layers. *Physics of Fluids*, 28(4), p. 045102.

Agostini, L. & Leschziner, M. A., 2016. Predicting the response of small-scale near-wall turbulence to large-scale outer motions. *Physics of Fluids*, 28(1), p. 015107.

Agostini, L. & Leschziner, M. A., 2019. On the departure of near-wall turbulence from the quasi-steady state. *Journal of Fluid Mechanics*, Volume 871, p. R1.

Baars, W. J., Hutchins, N. & Marusic, I., 2017. Reynolds number trend of hierarchies and scale interactions in turbulent boundary layers. *Philosophical Transactions of the Royal Society A*, 375(2089), p. 20160077.

Bernardini, M., Pirozzoli, S. & Orlandi, P., 2013. Velocity statistics in turbulent channel flow up to Reτ=4000. *Journal of Fluid Mechanics*, Volume 742, pp. 171-191.

Bhuiyan, S. M. A., Adhami, R. R. & Khan, J. F., 2008. Fast and Adaptive Bidimensional Empirical Mode Decomposition Using Order-Statistics Filter Based Envelope Estimation. *EURASIP J. Adv. Signal Process*, Volume 2008, p. 728356.

Bose, S. & Park, G., 2018. Wall-Modeled Large-Eddy Simulation for Complex Turbulent Flows. *Annual Review of Fluid Mechanics*, Volume 50, pp. 535-561.

Boudet, J., Monier, J. & Gao, F., 2015. Implementation of a Roughness Element to Trip Transition in Large-eddy Simulation. *Journal of Thermal Science*, 24(1), pp. 30-36.

Boussinesq, J., 1877. *Essai sur la theorie des eaux courantes*. s.l.:Memoires presentes par divers savants a l'Academie des Sciences de l'Institut National de France, Tome XXIII, No 1. Imprimerie Nationale, Paris..

Boyd, J., 2001. *Chebyshev and Fourier Spectral Methods.* 2nd ed. New York: Dover.

Brandt, L., Schlatter, P. & Henningson, D., 2004. Transition in boundary layers subject to free-stream turbulence. *J. Fluid Mech.*, Volume 517, pp. 167-198.

Brinkerhoff, J. & Yaras, M., 2011. Interaction of viscous and inviscid instability modes in separation–bubble transition. *Physics of Fluids*, Volume 23, p. 124102.

Cabot, W. & Moin, P., 2000. Approximate Wall Boundary Conditions in the Large-Eddy Simulation of High Reynolds Number Flow. *Flow, Turbulence and Combustion*, Volume 63, p. 269–291.

Carney, S., Engquist, B. & Moser, R., 2020. Near-wall patch representation of wall-bounded turbulence. *Journal of Fluid Mechanics*, Volume 903, p. A23.

Chapman, D., 1979. Computational Aerodynamics Development and Outlook. *AIAA Journal*, 17(12), pp. 1293-1313.

Chauhan, K., Monkewitz, P. & Nagib, H., 2009. Criteria for assessing experiments in zero pressure-gradient boundary layers. *Fluid Dyn. Res.*, Volume 41, p. 021404.

Chen, C. & He, L., 2021. On locally embedded two-scale solution for wall-bounded turbulent flows. *Journal of Fluid Mechanics*, Volume 933, p. A47.

Choi, H. & Moin, P., 2012. Grid-point requirements for large eddy simulation: Chapman's estimates revisited. *Physics of Fluids*, 24(1), p. 011702.

Coles, D., 1964. The turbulent boundary layer in a compressible fluid. *Phys. Fluids.*, Volume 7, pp. 1403-23.

de Villiers, E., 2006. *The potential of Large Eddy Simulation for the modeling of wall bounded flows*, PhD thesis. London: Imperial College of Science, Technology and Medicine.

Deck, S., Renard, N., Laraufie, R. & Sagaut, P., 2014. Zonal detached eddy simulation (ZDES) of a spatially developing flat plate turbulent boundary layer over the Reynolds number range $3150 \leqslant Re\theta \leqslant 14000$. Physics of Fluids, Volume 26, p. 025116.

del Alamo, J., Jimenez, J., Zandonade, P. & Moser, R., 2004. Scaling of the energy spectra of turbulent channels. Journal of Fluid Mechanics, Volume 500, pp. 135-144.

Denton, J. D., 1993. Loss Mechanisms in Turbomachines. *Journal of Turbomachinery*, 115(4), pp. 621-656.

Devenport, W. & Lowe, T., 2022. Equilibrium and non-equilibrium turbulent boundary layers. *Progress in Aerospace Sciences*, Volume 131, p. 100807.

Dryden, H. L., 1959. *Transition from laminar to turbulent*. In: Turbulent Flows and Heat Transfer. Princeton, New Jersey: Princeton University Press.

Eeckhout, L., 2017. Is Moore's Law Slowing Down? What's Next?. *IEEE Micro*, Volume 37, pp. 4-5.

Erm, L. & Joubert, P., 1991. Low-Reynolds-number turbulent boundary layers. *Journal of Fluid Mechanics*, Volume 230, pp. 1-44.

Farmer, C. L., 2002. Upscaling: a review. *International Journal for Numerical Methods in Fluids*, Volume 40, pp. 63-78.

Farrell, P. E. & Maddison, J. R., 2011. Conservative interpolation between volume meshes by local Galerkin projection. *Computer Methods in Applied Mechanics and Engineering*, 200(1-4), pp. 89-100.

Fernholz, H. & Finley, P., 1996. The incompressible zero-pressure-gradient turbulent boundary layer: an assessment of the data. *Prog. Aerospace Sci*, Volume 32, pp. 245-311.

Gao, F., Ma, W., Zambonini, G., Boudet, J., Ottavy, X., Lu, L., & Shao, L., 2015. Large-eddy simulation of 3-D corner separation in a linear compressor cascade. *Physics of Fluids*, Volume 27, p. 085105.

Georgiadis, N. J., Rizzetta, D. P. & Fureby, C., 2010. Large-Eddy Simulation: Current Capabilities, Recommended Practices, and Future Research. *AIAA Journal*, 48(8), p. 1772.

Ghanadi, F., Arjomandi, M., Cazzolato, B. & Zander, A., 2015. Analysis of the turbulent boundary layer in the vicinity of a self-excited cylindrical Helmholtz resonator. *Journal of Turbulence*, 16(8), pp. 705-728.

Hallback, M., Groth, J. & Johansson, A. V., 1989. *A Reynolds stress closure for the dissipation in anisotropic turbulent flows.* Stanford, CA, Symposium on Turbulent Shear Flows, 7th.

Hamilton, J., Kim, J. & Waleffe, F., 1995. Regeneration mechanisms of near-wall turbulence structures. *Journal of Fluid Mechanics*, Volume 287, pp. 317-348.

He, L., 2018. Multiscale block spectral solution for unsteady flows. *Int. J. Numer. Meth. Fluids*, Volume 86, pp. 655-677.

He, L., 2021. Averaging for High Fidelity Modeling - Toward Large Eddy Simulations in Multi-Passage Multi-Row Configurations. *Journal of Turbomachinery*, 143(2), p. 021002.

Hickling, T. & He, L., 2021. Some Observations on the Computational Sensitivity of Rotating Cavity Flows. *Journal of Engineering for Gas Turbines and Power*, 143(4), p. 041014.

Hoyas, S. & Jimenez, J., 2006. Scaling of the velocity fluctuations in turbulent channels up to Reτ=2003. *Physics of Fluids*, Volume 18, p. 011702.

Huang, N. E., Shen, Z., Long, S. R., Wu, M. C., Shih, H. H., Zheng, Q., Yen, N.-C., Tung, C. C. & Liu, H. H., 1998. The empirical mode decomposition and the Hilbert spectrum for nonlinear and non-stationary time series analysis. *Proc. R. Soc. London, A*, Volume 454, p. 903.

Hunt, J., Wary, A. & Moin, P., 1988. *Eddies, streams, and convergence zones in turbulent flows.* CTR-S88, s.n.

Hutchins, N., 2012. Caution: tripping hazards. *Journal of Fluid Mechanics*, Volume 710, pp. 1-4.

Hutchins, N. & Marusic, I., 2007. Evidence of very long meandering features in the logarithmic region of turbulent boundary layers. *Journal of Fluid Mechanics*, Volume 579, pp. 1-28.

Ishihara, T., Gotoh, T. & Kaneda, Y., 2009. Study of High–Reynolds Number Isotropic Turbulence by Direct Numerical Simulation. *Annual Review of Fluid Mechanics*, Volume 41, pp. 165-180.

Jacobs, R. & Durbin, P., 2001. Simulations of bypass transition. *Journal of Fluid Mechanics*, Volume 428, pp. 185-212.

Jarrin, N., Benhamadouche, S., Laurence, D. & Prosser, R., 2006. A synthetic-eddy-method for generating inflow conditions for large-eddy simulations. *International Journal of Heat and Fluid Flow*, Volume 27, p. 585–593.

Jeong, J. & Hussain, F., 1995. On the identification of a vortex. *Journal of Fluid Mechanics*, Volume 285, pp. 69-94.

Jeong, J., Hussain, F., Schoppa, W. & Kim, J., 1997. Coherent structures near the wall in a turbulent channel flow. *J. Fluid Mech.*, Volume 332, pp. 185-214.

Jimenez, J., 2003. Computing high-Reynolds-number turbulence: will simulations ever replace experiments?. *J. Turbulence*, Volume 4, pp. 1-14.

Jimenez, J., 2013. Near-wall turbulence. *Physics of Fluids*, 25(10), p. 101302.

Jimenez, J. & Moin, P., 1991. The minimal flow unit in near-wall turbulence. *Journal of Fluid Mechanics*, Volume 225, pp. 213-240.

Jimenez, J. & Moser, R., 2000. Large-Eddy Simulations: Where Are We and What Can We Expect?. *AIAA Journal*, 38(4), pp. 605-612.

Jimenez, J. & Pinelli, A., 1999. The autonomous cycle of near-wall turbulence. *Journal of Fluid Mechanics*, Volume 389, pp. 335-359.

Jovanovic, M., Schmid, P. & Nichols, J., 2014. Sparsity-promoting dynamic mode decomposition. *Physics of Fluids*, Volume 26, p. 024103.

Kadivar, M., Tormey, D. & McGranaghan, G., 2021. A review on turbulent flow over rough surfaces: Fundamentals and theories. *International Journal of Thermofluids*, Volume 10, pp. 1-34.

Kapsis, M., He, L., Li, Y., Valero, O., Wells, R., Krishnababu, S., Gupta, G., Kapat, J. & Schaenzer, M., 2020. Multiscale parallelized computational fluid dynamics modeling toward resolving manufacturable roughness. *Journal of Engineering for Gas Turbines and Power*, 142(2), p. 021001.

Khujadze, G. & Oberlack, M., 2004. DNS and scaling laws from new symmetry groups of ZPG. *Theor. Comput. Fluid Dyn.*, Volume 18, pp. 391-411.

Khujadze, G. & Oberlack, M., 2007. *New scaling laws in ZPG turbulent boundary layer flow*. Munchen, Germany, s.n.

Klebanoff, P. & Tidstrom, K., 1972. Mechanism by which a two-dimensional roughness element induces boundary-layer transition. *Physics of Fluids*, 15(7), p. 1173.

Klewicki, J., Fife, P. & Wei, T., 2009. On the logarithmic mean profile. *Journal of Fluid Mechanics*, Volume 638, pp. 73-93.

Kline, S. J., Reynolds, W. C., Schraub, F. A. & Runstadler, P. W., 1967. The structure of turbulent boundary layers. *Journal of Fluid Mechanics*, 30(4), pp. 741 - 773.

Kline, S., Reynolds, W., Schraub, F. & Runstadler, P., 2006. The structure of turbulent boundary layers. *Journal of Fluid Mechanics*, 30(4), pp. 741-773.

Kolmogorov, A., 1941. The Local Structure of Turbulence in Incompressible Viscous Fluid for Very Large Reynolds' Numbers. *Doklady Akademiia Nauk SSSR*, Volume 30, pp. 301-305.

Komen, E., Camilo, L., Shams, A., Geurts, B., & Koren, B., 2017. A quantification method for numerical dissipation in quasi-DNS and under-resolved DNS, and effects of numerical dissipation in quasi-DNS and under-resolved DNS of turbulent channel flows. *Journal of Computational Physics*, Volume 345, pp. 565-595.

Komen, E., Shams, A., Camilo, L. & Koren, B., 2014. Quasi-DNS capabilities of OpenFOAM for different mesh types. *Computers & Fluids*, Volume 96, pp. 87-104.

Komminaho, J. & Skote, M., 2002. Reynolds stress budgets in couette and boundary layer flows. *Flow Turbul. Combust.*, Volume 68, pp. 167-192.

Kraichnan, R., 1970. Diffusion by a Random Velocity Field. *Physics of Fluids*, Volume 13, p. 22.

Kravchenko, A., Moin, P. & Moser, R., 1996. Zonal embedded grids for numerical simulations of wall-bounded turbulent flows. *Journal of Computational Physics*, Volume 127, pp. 412-423.

Larsson, J., Kawai, S., Bodart, J. & Bermejo-Moreno, I., 2016. Large eddy simulation with modeled wall-stress: recent progress and future directions. *Mechanical Engineering Reviews*, 3(1), pp. 15-00418.

Launder, B. & Spalding, D., 1974. The numerical computation of turbulent flows. *Computer Methods in Applied Mechanics and Engineering*, 3(2), pp. 269-289.

Lee, M. & Moser, R., 2015. Direct numerical simulation of turbulent channel flow up to Reτ~5200. *Journal of Fluid Mechanics*, Volume 774, pp. 395-415.

Lee, M. & Moser, R., 2019. Spectral analysis of the budget equation in turbulent channel flows at high Reynolds number. *Journal of Fluid Mechanics*, Volume 860, pp. 886-938.

Lozano-Duran, A. & Bae, H., 2019. Error scaling of large-eddy simulation in the outer region of wall-bounded turbulence. *Journal of Computational Physics*, Volume 392, pp. 532-555.

Lozano-Duran, A. & Jimenez, J., 2014. Effect of the computational domain on direct simulations of turbulent channels up to Reτ = 4200. *Physics of Fluids*, Volume 26, p. 011702.

Lund, T., 2003. The use of explicit filters in large eddy simulation. *Computers and Mathematics with Applications*, 46(4), pp. 603-616.

Lund, T., Wu, X. & Squires, K., 1998. Generation of Turbulent Inflow Data for Spatially-Developing Boundary Layer Simulations. *Journal of Computational Physics*, 140(2), pp. 233-258.

Marusic, I., Baars, W. J. & Hutchins, N., 2017. Scaling of the streamwise turbulence intensity in the context of inner-outer. *Physical Review Fluids*, Volume 2, p. 100502.

Marusic, I., Chauhan, K., Kulandaivelu, V. & Hutchins, N., 2015. Evolution of zero-pressure-gradient boundary layers from different tripping conditions. *J. Fluid Mech.*, Volume 783, pp. 379-411.

Marusic, I., Mathis, R. & Hutchins, N., 2010. Predictive Model for Wall-Bounded Turbulent Flow. *Science*, 329(5988), pp. 193-196.

Marusic, I., McKeon, J., Monkewitz, A., Nagib, M., Smits, J., & Sreenivasan, R., 2010. Wall-bounded turbulent flows at high Reynolds numbers. *Phys. Fluids*, 22(6), p. 065103.

Marusic, I., Monty, J., Hultmark, M. & Smits, A., 2013. On the logarithmic region in wall turbulence. *Journal of Fluid Mechanics*, Volume 716, p. R3.

Mathis, R., Hutchins, N. & Marusic, I., 2009. Large-scale amplitude modulation of the small-scale structures in turbulent boundary layers. *Journal of Fluid Mechanics*, Volume 628, pp. 311-337.

Mizuno, Y. & Jiménez, J., 2013. Wall turbulence without walls. *Journal of Fluid Mechanics*, Volume 723, pp. 429-455.

Moin, P. & Jimenez, J., 1997. Large-Eddy Simulation of Turbulent Flows. *AIAA Paper*, 97(0749).

Monkewitz, P., 2007. Self-consistent high-Reynolds-number asymptotics for zero-pressure-gradient turbulent boundary layers. *Physics of Fluids*, Volume 19, p. 115101.

Moore, G., 1965. Cramming more components onto integrated circuits. *Electronics*, 38(8), p. 114.

Moser, R., Kim, J. & Mansour, N., 1999. Direct numerical simulation of turbulent channel flow up to Reτ=590. *Physics of Fluids*, 11(4), p. 943.

Ning, W. & He, L., 2001. Some modeling issues on trailing-edge vortex shedding. *AIAA Journal*, 39(5), pp. 787-793.

Orszag, S., 1970. Analytical theories of turbulence. *Journal of Fluid Mechanics*, 41(2), pp. 363-386.

Pascarelli, A., Piomelli, U. & Candler, G., 2000. Multi-Block large-eddy simulations of turbulent boundary layers. *Journal of Computational Physics*, 157(1), pp. 256-279.

Piomelli, U. & Balaras, E., 2002. Wall-Layer Models for Large-Eddy Simulations. *Annual Review of Fluid Mechanics*, Volume 34, pp. 349-374.

Prandtl, L., 1904. *On the Motion of Fluids in Very Little Friction.* Heidelberg, Germany, s.n.

Rao, N., Jefferson-Loveday, R., Tucker, P. & Lardeau, S., 2014. Large Eddy Simulations in Turbines: Influence of Roughness and Free-Stream Turbulence. *Flow Turbulence Combust.*, Volume 92, pp. 543-561.

Reshotko, E., 2001. Transient growth: A factor in bypass transition. *Physics of Fluids*, 13(5), pp. 1067-1075.

Reynolds, O., 1883. An Experimental Investigation of the Circumstances which determine whether the Motion of Water shall be Direct or Sinuous, and of the Law of Resistance in Parallel Channels. *Philosophical Transactions of the Royal Society of London*, Volume 174, p. 935–982.

Robinson, S., 1991. COHERENT MOTIONS IN THE TURBULENT BOUNDARY LAYER. *Annu. Rev. Fluid Mech.*, Volume 23, pp. 601-39.

Rodríguez-López, E., Bruce, P. & Buxton, O., 2016. Near field development of artificially generated high Reynolds number turbulent boundary layers. *Phys. Rev. Fluids*, 1(7), p. 074401.

Rumsey, C., 2014. *SA Expected Results - 2D Zero Pressure Gradient Flat Plate*, s.l.: Langley Research Center, Turbulence Modeling Resource.

Sagaut, P. & Deck, S., 2009. Large eddy simulation for aerodynamics: status and perspectives. *Philos Trans A Math Phys Eng Sci.*, 367(1899), pp. 2849-60.

Sandham, N., Johnstone, R. & Jacobs, C., 2017. Surface-sampled simulations of turbulent flow at high Reynolds number. *International Journal for Numerical Methods in Fluids*, 85(9), pp. 525-537.

Sanmiguel Vila, C., Vinuesa, R., Discetti, S., Ianiro, A., Schlatter, P., & Orlu, R., 2017. On the identification of well-behaved turbulent boundary layers. *J. Fluid Mech.*, Volume 822, pp. 109-138.

Sayadi, T., Hamman, W. & Moin, P., 2013. Direct numerical simulation of complete H-type and K-type transitions with implications for the dynamics of turbulent boundary layers. *J. Fluid Mech.*, Volume 724, pp. 480-509.

Schlatter, P. & Orlu, R., 2010. Assessment of direct numerical simulation data of turbulent boundary layers. *J. Fluid Mech.*, Volume 659, pp. 116-126.

Schlatter, P. & Orlu, R., 2012. Turbulent boundary layers at moderate Reynolds numbers: inflow length and tripping effects. *J. Fluid Mech.*, Volume 710, pp. 5-34.

Schlichting, H., 1968. *Boundary-layer theory*. New York: McGraw-Hill.

Schmid, P., 2010. Dynamic mode decomposition of numerical and experimental data. *Journal of Fluid Mechanics*, Volume 656, pp. 5-28.

Shur, M. L., Spalart, P. R., Strelets, M. K. & Travin, A. K., 2008. A hybrid RANS-LES approach with delayed-DES and wall-modelled LES capabilities. *International Journal of Heat and Fluid Flow*, 29(6), pp. 1638-1649.

Sillero, J., Jimenez, J. & Moser, R., 2013. One-point statistics for turbulent wall-bounded flows at Reynolds numbers up to $\delta+ \approx 2000$. *Physics of Fluids*, Volume 25, p. 105102.

Silvestri, A., Ghanadi, F., Arjomandi, M., Cazzolato, B., & Zander, A., 2018. The Application of Different Tripping Techniques to Determine the Characteristics of the Turbulent Boundary Layer Over a Flat Plate. *Journal of Fluids Engineering*, Volume 140, p. 011204.

Simens, M., Jimenez, J. & Mizuno, Y., 2009. A high-resolution code for turbulent boundary layers. *J. Comput. Phys.*, Volume 228, pp. 4218-4231.

Skote, M., Haritonidis, J. & Henningson, D., 2002. Varicose instabilities in turbulent boundary layers. *Phys. Fluids*, Volume 14, pp. 2309-2323.

Slotnick, J. P., Khodadoust, A., Alonso, J. J., Darmofal, D. L., Gropp, W., Lurie, E. A., & Mavriplis, D. J., 2014. *CFD Vision 2030 Study: A Path to Revolutionary Computational*, s.l.: NASA Technical Reports Server.

Smagorinsky, J., 1963. General Circulation Experiments with the Primitive Equations. *Monthly Weather Review*, 91(3), p. 99.

Smith, C. R. & Metzler, S. P., 1983. The characteristics of low-speed streaks in the near-wall region of a turbulent boundary layer. *Journal of Fluid Mechanics*, Volume 129, pp. 27-54.

Smits, A. J. & Marusic, I., 2013. Wall-bounded turbulence. *Phys. Today.*, 66(9), pp. 25-30.

Smits, J., Matheson, N. & Joubert, N., 1983. Low-Reynolds-number turbulent boundary layers in zero and favourable pressure-gradients. *J. Ship Res.*, Volume 27, pp. 147-157.

Spalart, P., 1988. Direct simulation of a turbulent boundary layer up to Reθ = 1410. *Journal of Fluid Mechanics*, Volume 187, pp. 61-98.

Spalart, P. & Allmaras, S., 1994. A One-Equation Turbulence Model for Aerodynamic Flows. *Recherche Aerospatiale*, Volume 1, pp. 5-21.

Spalart, P. R., 2009. Detached-Eddy Simulation. *Annual Review of Fluid Mechanics*, Volume 41, pp. 181-202.

Spalart, P. R., Deck, S., Shur, M. L., Squires, K. D., Strelets, M. K., & Travin, A., 2006. A New Version of Detached-eddy Simulation, Resistant to Ambiguous Grid Densities. *Theoretical and Computational Fluid Dynamics*, Volume 20, pp. 181-195.

Spalart, P. R., Jou, W., Strelets, M. & Allmaras, S., 1997. *Comments on the Feasibility of LES for Wings, and on a Hybrid RANS/LES Approach.* Ruston, Louisiana, USA, Proceedings of the First AFOSR International Conference on DNS/LES.

Spalart, P. & Watmuff, J., 1993. Experimental and numerical study of a turbulent boundary. *J. Fluid Mech.*, Volume 249, pp. 337-371.

Sreenivasan, K. R. & Antonia, R. A., 1997. THE PHENOMENOLOGY OF SMALL-SCALE TURBULENCE. *Annual Review of Fluid Mechanics*, Volume 29, pp. 435-472.

Taira, K., Brunton, S., Dawson, S., Rowley, C., Colonius, T., McKeon, B., Schmidt, O., Gordeyev, S., Theofilis, V. & Ukeiley, L., 2017. Modal Analysis of Fluid Flows: An Overview. *AIAA Journal*, 55(12), pp. 4013-4041.

Talluru, K. M., Baidya, R., Hutchins, N. & Marusic, I., 2014. Amplitude modulation of all three velocity components in turbulent boundary layers. *Journal of Fluid Mechanics*, Volume 746, p. R1.

Tang, Y. & Akhavan, R., 2016. Computations of equilibrium and non-equilibrium turbulent channel flows using a nested-LES approach. *Journal of Fluid Mechanics*, Volume 793, pp. 709-748.

Tani, I., 1969. Boundary-Layer Transition. *Annual Review of Fluid Mechanics*, Volume 1, pp. 169-196.

Tennekes, H. & Lumley, J. L., 1972. In: *A First Course in Turbulence.* s.l.:The MIT Press, p. 159.

Tissot, G., Cordier, L., Benard, N. & Noack, B., 2014. Model reduction using Dynamic Mode Decomposition. *Comptes Rendus Mecanique*, Volume 342, pp. 410-416.

Townsend, A. A., 1976. *The Structure of Turbulent Shear Flow.* s.l.:Cambridge University Press.

Trefethen, L. N., 2000. *Spectral Methods in Matlab*. Philadelphia: SIAM.

von Karman, T., 1930. *Mechanische Ahnlichkeit und Turbulenz.* s.l., s.n.

Wang, H., Huang, W. & Xu, C., 2021. Off-wall boundary conditions for large-eddy simulation based on near-wall turbulence prediction. *Physics of Fluids*, Volume 33, p. 045125.

Welch, P. D., 1967. The use of Fast Fourier Transform for the estimation of power spectra: A method based on time averaging over short, modified periodograms. *IEEE Transactions on Audio and Electroacoustics*, 15(2), pp. 70-73.

Wheeler, A., Dickens, A. & Miller, R., 2018. The Effect of Nonequilibrium Boundary Layers on Compressor Performance. *J. Turbomach.*, 140(10), p. 101003.

Wilcox, D. C., 2008. Formulation of the k-omega Turbulence Model Revisited. *AIAA Journal*, 46(11), pp. 2823-2838.

Wu, J., Xiao, H., Sun, R. & Wang, Q., 2019. Reynolds-averaged Navier-Stokes equations with explicit data-driven Reynolds stress closure can be ill-conditioned. *Journal of Fluid Mechanics*, Volume 869, pp. 553-586.

Wu, S., Christensen, K. & Pantano, C., 2019. Modelling smooth- and transitionally rough-wall turbulent channel flow by leveraging inner-outer interactions and principal component analysis. *J. Fluid Mech.*, Volume 863, p. 407–453.

Wu, X., 2017. Inflow Turbulence Generation Methods. *Annu. Rev. Fluid Mech.*, Volume 49, pp. 23-49.

Wu, X. & Moin, P., 2009. Direct numerical simulation of turbulence in a nominally zero-pressure-gradient flat-plate boundary layer. *Journal of Fluid Mechanics*, Volume 630, pp. 5-41.

Zhang, C. & Chernyshenko, S. I., 2016. Quasisteady quasihomogeneous description of the scale interactions in near-wall turbulence. *Physical Review Fluids*, Volume 1, p. 014401.

Zhou, W., Rao, Y. & Hu, H., 2016. An Experimental Investigation on the Characteristics of Turbulent Boundary Layer Flows Over a Dimpled Surface. *J. Fluids Eng.*, 138(2), p. 021204.

10 APPENDICES

APPENDIX 1 BUFFER REGION AND 'MODULATION' 221

APPENDIX 1 BUFFER REGION AND 'MODULATION'

For the baseline implementation of the two-scale method, it is assumed that the 'modulation' can be mostly regarded as a one-way influence of the large scales in the outer flow region on the small scales and some intermediate scales in the near-wall region, as indicated in Figure 5.14. On the other hand, the modulated near-wall turbulent flow should in principle be able to provide feedback to affect the outer large scales, which is neglected in the baseline implementation. Although the authors have so far not seen any noticeable feedback effects, the issue should be dealt with for completeness of the framework and implementation method. In this Appendix, we consider a very simple option without extra mesh cost to include this feedback, should it become significant.

As illustrated in Figure 10.1, we take a local region of the coarse-mesh domain directly adjacent to the embedded fine-mesh block as a target buffer region (labelled as 'Buffer 1'). Correspondingly, we take a global buffer region to be corrected which is adjacent to the global inner coarse-mesh region, labelled as 'Buffer 2'. A phenomenological argument within the two-scale framework follows that if the 'modulation' resolved in the near-wall fine mesh block does have non-negligible feedback on the outer flow region, the buffer region adjacent to the local fine-mesh block will have to be different from that of the global outer coarse-mesh region directly adjacent to the coarse-mesh inner region. Thus, the time-averaged flow of Buffer 1 will have to be different from that of Buffer 2. As such we can use the time-averaged flow of Buffer 1 as the target to correct Buffer 2.

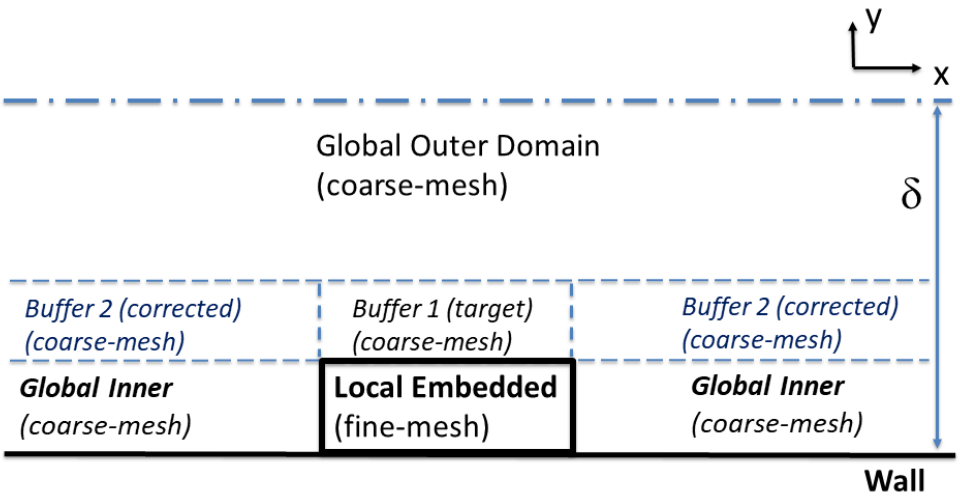


Figure 10.1. **Domain with coarse-mesh buffer regions as an extended version of Figure 3.1.**

For the buffer regions, the general upscaled coarse-mesh flow equations (3.12) can be written as:

$$\frac{\partial \boldsymbol{u}_B}{\partial t} + R(\boldsymbol{u}_B) = (\boldsymbol{ST}_{st})_{B1} + (\boldsymbol{ST}_t)_{B2} \tag{10.1}$$

For the target region Buffer 1, the space-time averaging is now reduced to time-averaging only. Thus, the driving source is simply generated by taking the inverse mode of the time-averaging:

$$(\boldsymbol{ST}_{st})_{B1} = R(\overline{\boldsymbol{u}}_{B1}) \tag{10.2}$$

For Buffer 2, making use of equation (3.15), we have the upscaled equation:

$$\frac{\partial \boldsymbol{u}_{B2}}{\partial t} + R(\boldsymbol{u}_{B2}) = R(\overline{\boldsymbol{u}}_{B1}) + \overline{R(\boldsymbol{u}_{B2})} - R(\overline{\boldsymbol{u}}_{B2})$$

(10.3)

Time-averaging equation (10.3), we then get the resultant equation driving the converged time-averaged flow in Buffer 2 to the target in Buffer 1, as intended:

$$R(\overline{\boldsymbol{u}}_{B2}) = R(\overline{\boldsymbol{u}}_{B2})$$

(10.4)

It is emphasised that the implementation of this option does not involve any extra mesh, as all the buffer regions are of the coarse mesh which is meant to be sufficiently fine to resolve all relevant scales locally. The only extra cost will be that for local time-averaging, and for evaluating and actuating the time-averaging source terms in the inverse or the direct mode for the two buffer regions respectively, which tend to be minimally small.

The two-scale method with the added extra buffer regions is tested for the case with $Re_\tau \approx 5200$. The buffer thickness is taken to be 0.05δ. The differences between the results with and without the extra buffer regions are negligible as shown in Figure 10.2. All the results agree well with the DNS data. This further test seems to suggest that for the present cases at the given Reynolds numbers, the 'modulation' can still be regarded as predominantly only influential on small and intermediate scales in the near-wall region without noticeable feedback to the large scales themselves in the outer flow region.

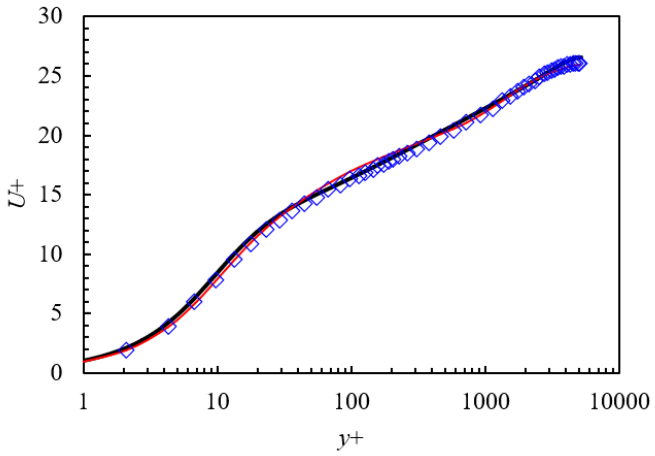


Figure 10.2. **Mean velocity profiles at $Re_\tau \approx 5200$. The blue symbols '◊' indicate the global coarse-mesh result with the buffer, while the red solid line '—' indicates the coarse-mesh results without buffer. The black solid line '—' indicates the DNS results from Lee & Moser (2015). Note that not all data points are included to increase readability.**